Mon. Not. R. Astron. Soc. **000**, 000–000 (0000) Printed 8 August 2013 (MN LaTeX style file v2.2)

The GALEX Arecibo SDSS Survey. VIII. Final Data Release – The Effect of Group Environment on the Gas Content of Massive Galaxies

Barbara Catinella[1,2*], David Schiminovich[3], Luca Cortese[2,4], Silvia Fabello[5], Cameron B. Hummels[6], Sean M. Moran[7], Jenna J. Lemonias[3], Andrew P. Cooper[8], Ronin Wu[9], Timothy M. Heckman[10], and Jing Wang[1]

[1] *Max-Planck Institut für Astrophysik, D-85741 Garching, Germany*
[2] *Centre for Astrophysics and Supercomputing, Swinburne University of Technology, Hawthorn, VIC 3122, Australia*
[3] *Department of Astronomy, Columbia University, New York, NY 10027, USA*
[4] *European Southern Observatory, D-85748 Garching, Germany*
[5] *Autoliv Electronics Germany, Theodor-Heuss-Str. 2, 85221 Dachau, Germany*
[6] *Department of Astronomy and Steward Observatory, University of Arizona, Tucson, AZ 85721, USA*
[7] *Smithsonian Astrophysical Observatory, 60 Garden Street, Cambridge, MA 02138, USA*
[8] *National Astronomical Observatories, Chinese Academy of Sciences, 20A Datun Rd., Chaoyang, Beijing 100012, P.R. China*
[9] *Commissariat à l'Energie Atomique (CEA), 91191 Gif-sur-Yvette, France*
[10] *Department of Physics and Astronomy, Johns Hopkins University, Baltimore, MD 21218, USA*

ABSTRACT

We present the final data release from the GALEX Arecibo SDSS Survey (GASS), a large Arecibo program that measured the HI properties for an unbiased sample of ∼800 galaxies with stellar masses greater than 10^{10} $M_\odot$ and redshifts $0.025 < z < 0.05$. This release includes new Arecibo observations for 250 galaxies. We use the full GASS sample to investigate environmental effects on the cold gas content of massive galaxies at fixed stellar mass. The environment is characterized in terms of dark matter halo mass, obtained by cross-matching our sample with the SDSS group catalog of Yang et al. Our analysis provides, for the first time, clear statistical evidence that massive galaxies located in halos with masses of $10^{13}-10^{14}$ $M_\odot$ have at least 0.4 dex less HI than objects in lower density environments. The process responsible for the suppression of gas in group galaxies most likely drives the observed quenching of the star formation in these systems. Our findings strongly support the importance of the group environment for galaxy evolution, and have profound implications for semi-analytic models of galaxy formation, which currently do not allow for stripping of the cold interstellar medium in galaxy groups.

Key words: galaxies:evolution–galaxies: fundamental parameters–ultraviolet: galaxies– radio lines:galaxies

1 INTRODUCTION

As the source of the material that will eventually form stars, atomic hydrogen (HI) is clearly a key ingredient to understand how galaxies form and evolve. For instance, physical processes that transform galaxies from blue, star-forming to "red and dead" objects must deplete their gas reservoirs first, so that their star formation is quenched as a result. Systematic studies of the cold gas content of galaxies as a function of their star formation, mass and structural properties, and across all environmental densities (*e.g.* Catinella et al. 2010; Huang et al. 2012), are necessary to explain the variety of systems observed today in the local Universe, and to provide important constraints to theoretical models and simulations of galaxy formation (*e.g.* Fu et al. 2010; Lagos et al. 2011; Davé, Finlator & Oppenheimer 2011; Kauffmann et al. 2012).

Environmental mechanisms are known to be effective in removing gas from galaxies in high-density regions, and indeed HI is one of the most sensitive tracers of environmen-

* bcatinella@swin.edu.au

tal effects. This is because HI gas typically extends further away from the center of galaxies compared to other baryonic components, thus it is more easily affected by environment. A classic example of the value of HI observations in this context is represented by spatially-resolved radio observations of the M81 group, which have revealed a spectacular, complex network of gas filaments connecting three galaxies that appear completely undisturbed in optical images (Yun, Ho & Lo 1994).

Despite its importance as environmental probe, we are far from having a comprehensive picture of how the HI content of galaxies varies as a function of the local density. This is in stark contrast with optical studies, where the availability of large photometric and spectroscopic databases such as those assembled by the Sloan Digital Sky Survey (SDSS; York et al. 2000) and the Two-degree Field Galaxy Redshift Survey (2dFGRS; Colless et al. 2001) has allowed us to quantify how the star formation properties of galaxies vary across all environments, from voids to clusters, and for different cosmic epochs (*e.g.* Balogh et al. 2004; Kauffmann et al. 2004; Cooper et al. 2006). The evidence based on such datasets suggests that the transformation from star-forming to quiescent galaxies is a smooth function of density, and happens in great part outside clusters (*e.g.* Dressler 1980; Lewis et al. 2002; Gómez et al. 2003; Blanton & Moustakas 2009). Surprisingly enough, we have not pinned down the mechanisms that drive this decrease in star formation rate, and whether this is accompanied/triggered by gas removal. This is due to a lack of HI observations covering a large enough range of environments to sufficient depth.

Environmental HI studies to date concentrated on the difference between cluster and field populations, and demonstrated that galaxies in high-density regions are HI deficient compared to isolated objects with similar size and stellar morphology (Giovanelli & Haynes 1985; Solanes et al. 2001). Resolved HI maps of galaxies in the Virgo and Coma clusters clearly show that HI is removed from the star-forming disk (Gavazzi 1989; Cayatte et al. 1990; Bravo-Alfaro et al. 2000; Kenney, van Gorkom & Vollmer 2004; Chung et al. 2009), mainly due to ram pressure stripping by the dense intracluster medium through which galaxies move (Gunn & Gott 1972; Vollmer 2009; Boselli & Gavazzi 2006). What happens to the gas content in the lower density group environment, where ram pressure is thought to be inefficient, is still unclear. Several studies have mapped the HI content of galaxies in groups, and found examples of HI-deficient galaxies (*e.g.* Huchtmeier 1997; Verdes-Montenegro et al. 2001; Kilborn et al. 2009). Tidal interactions in groups might funnel gas in the central regions of galaxies and increase their star formation (Iono, Yun & Mihos 2004; Kewley, Geller & Barton 2006), eventually reducing their HI content, but the net effect on statistical basis is unknown.

Because of limitations in the current HI samples, which target a limited range of environmental densities, with largely different selection criteria, HI sensitivities and multi-wavelength coverage, we still do not know at which density scale the environment starts affecting the gas content of galaxies. In order to quantify the effect of environment on the HI reservoir of galaxies, we need wide-area surveys over large enough volumes to sample a variety of environments, and deep enough to probe the HI-poor regime. Accompanying multi-wavelength information is essential not only to determine the environmental density, but also to provide measurements of the structural and star formation properties of the galaxies, that are necessary to connect the fate of the gas to that of the stars. In particular, because star formation and galaxy properties are known to scale primarily with mass (*e.g.* Kauffmann et al. 2003; Shen et al. 2003; Baldry et al. 2004), environmental comparisons must be done at fixed stellar mass.

HI-blind surveys such as the ongoing Arecibo Legacy Fast ALFA (ALFALFA; Giovanelli et al. 2005) survey map large volumes, but are not sensitive enough to detect HI-poor systems beyond the very local Universe (Gavazzi et al. 2013). However, the availability of high-quality HI spectra for galaxies that are individually not detected can offer important constraints on the average gas content of galaxies, when these are binned according to a given property and co-added or "stacked" (*e.g.* Fabello et al. 2011a,b). Indeed, statistical analyses based on stacking of optically-selected galaxies in the ALFALFA data cubes have already provided interesting insights into the average HI content of nearby massive galaxies in groups. Fabello et al. (2012) found that the average HI gas mass fraction declines with environmental density, and that such decline is stronger than what is observed for the mean global and central specific star formation rates. By comparing the observed trends with the results of semi-analytic models, they concluded that ram pressure stripping is likely to become effective in groups.

In this work, we use deep HI observations of optically-selected galaxies from the recently completed GALEX Arecibo SDSS Survey (GASS; Catinella et al. 2010, hereafter DR1) to investigate the effects of the environment on a galaxy-by-galaxy basis. GASS includes HI measurements for ~800 galaxies with stellar masses greater than 10^{10} $M_\odot$ and redshifts $0.025 < z < 0.05$. For these galaxies, we have homogeneous measurements of structural parameters from SDSS and ultraviolet (UV) photometry from GALEX (Martin et al. 2005) imaging. In addition to its clean selection criteria, GASS is unique for being gas fraction limited: we designed the survey to reach small limits of gas content at fixed stellar mass ($M_{\rm HI}/M_\star$~2-5%), therefore probing the HI-rich to HI-poor regime. Because there is no morphological or environmental selection, and our redshift cut spans a large volume (approximately corresponding to distances between 100 and 200 Mpc), GASS probes a variety of local densities to significant depth, and thus is ideally suited to investigate environmental effects on the gas content of massive galaxies.

This paper is organized as follows. We summarize our survey design and Arecibo observations in Section 2, and introduce our third and final data release, which includes new Arecibo observations for 250 galaxies, in Section 3 (the catalogs are in Appendix A). Sections 4 and 5 illustrate the HI properties of the full GASS sample and revisit the gas fraction scaling relations introduced in our earlier work. Section 6 briefly describes the group catalog (based on SDSS) used to characterize the environment of GASS galaxies, and presents our results on the environmental analysis. Discussion and conclusions follow in Section 7. All the distance-dependent quantities in this work are computed assuming $\Omega = 0.3$, $\Lambda = 0.7$ and $H_0 = 70$ km s^{-1} Mpc^{-1}. AB magnitudes are used throughout the paper.

2 SAMPLE SELECTION, ARECIBO OBSERVATIONS AND DATA REDUCTION

Survey design, sample selection, Arecibo observations and data reduction are described in detail in our first two data release papers (DR1 and Catinella et al. 2012b, hereafter DR2), thus we only provide a summary here, including relevant updates.

GASS was designed to measure the global HI properties of ∼1000 galaxies, selected uniquely by their stellar mass ($10 < \mathrm{Log}(M_\star/M_\odot) < 11.5$) and redshift ($0.025 < z < 0.05$). The galaxies are located within the intersection of the footprints of the SDSS primary spectroscopic survey, the GALEX Medium Imaging Survey and ALFALFA. We defined a GASS *parent sample*, based on SDSS DR6 (Adelman-McCarthy et al. 2008) and the final ALFALFA footprint, which includes 12006 galaxies that meet our survey criteria. The targets for 21cm observations were chosen by randomly selecting a subset of the parent sample which balanced the distribution across stellar mass and which maximized existing GALEX exposure time.

We observed the galaxies with the Arecibo radio telescope until we detected them or until we reached a limit of a few percent in gas mass fraction (defined as $M_{\mathrm{HI}}/M_\star$ in this work). Practically, we set a limit of $M_{\mathrm{HI}}/M_\star > 0.015$ for galaxies with $\mathrm{Log}(M_\star/M_\odot) > 10.5$, and a constant gas mass limit $\mathrm{Log}(M_{\mathrm{HI}}/M_\odot) = 8.7$ for galaxies with smaller stellar masses. This corresponds to a gas fraction limit $0.015 - 0.05$ for the whole sample. Given the HI mass limit assigned to each galaxy (set by its gas fraction limit and stellar mass), we computed the observing time, T_{max}, required to reach that value with our observing mode and instrumental setup. We excluded from our sample any galaxies requiring more than 3 hours of total integration time[1] (this effectively behaves like a redshift cut at the lowest stellar masses). Galaxies with good HI detections already available from ALFALFA and/or the Cornell HI digital archive (Springob et al. 2005, hereafter S05) were not re-observed. These HI-rich galaxies are added back to the GASS observations to make the *representative* sample (see Section 4).

GASS observations started in March 2008 and ended in July 2012. The total telescope time allocation was 1005 hours, of which ∼11% unusable due to radio frequency interference (RFI) or other technical problems. This third and final data release includes the observations carried out after March 1st 2011 (420 hours divided into 117 runs).

The Arecibo observations were carried out remotely in standard position-switching mode, using the L-band wide receiver and the interim correlator as a backend. Two correlator boards with 12.5 MHz bandwidth, one polarization, and 2048 channels per spectrum (yielding a velocity resolution of 1.4 km s^{-1} at 1370 MHz before smoothing) were centered at or near the frequency corresponding to the SDSS redshift of the target. We recorded the spectra every second with 9-level sampling.

The data reduction, performed in the IDL environment, includes Hanning smoothing, bandpass subtraction, RFI excision, and flux calibration. The spectra obtained from each on/off pair are weighted by $1/rms^2$, where rms is the root mean square noise measured in the signal-free portion of the spectrum, and co-added. The two orthogonal linear polarizations (kept separated up to this point) are averaged to produce the final spectrum, which is boxcar smoothed, baseline subtracted and measured as explained in the DR1 paper. The instrumental broadening correction for the velocity widths is described in the DR2 paper (we revised it after DR1, as discussed in Catinella et al. 2012a).

[1] There are a few exceptions (5% of the sample), represented by galaxies added for our initial pilot observations or already observed by one of our follow-up programs with the Hubble Space Telescope or other facilities (Moran et al. 2012; Saintonge et al. 2011).

3 DATA RELEASE

This data release is incremental over DR1 and DR2, and includes new Arecibo observations of 250 galaxies. The catalogs of optical, UV and 21 cm parameters for these objects are presented in Appendix A.

All the optical parameters were obtained from the SDSS DR7 database server[2]. Stellar masses are from the Max Planck Institute for Astrophysics (MPA)/Johns Hopkins University (JHU) value-added catalogs based on SDSS DR6, and assume a Chabrier (2003) initial mass function.

The GALEX UV photometry for our sample was reprocessed by us, as explained in Wang et al. (2010) and summarized in the DR1 paper. Briefly, we produced NUV$-r$ images by registering GALEX and SDSS frames, and convolving the latter to the UV point spread function. The measured NUV$-r$ colors are corrected for Galactic extinction only; we do not apply internal dust attenuation corrections.

The catalogs presented in our three releases are available both individually and combined on the GASS website[3], along with all the HI spectra in digital format.

4 GASS SAMPLE PROPERTIES

The three GASS data releases combined include 666 galaxies, of which 379 are HI detections and 287 are non-detections. We refer to this as the GASS *observed* sample. Because we did not reobserve galaxies with good HI detections already available from either ALFALFA or the S05 archive, this sample lacks the most gas-rich objects, which need to be added back in the correct proportions. By following the procedure described in the DR1 paper, we obtained a sample that includes 760 galaxies (of which 473 are detections) and that is representative in terms of HI properties. We refer to this as the GASS *representative* sample. Notice that, because of the improved statistics compared to DR1, here we use only one such representative sample (as opposed to a suite of 100 realizations with different sets of randomly-selected gas-rich galaxies added to the GASS observations).

The HI properties of the detected galaxies are illustrated in Figure 1 for both observed (**solid** histograms) and representative (dotted) samples. The blue histogram in the top left panel shows the redshift distribution for the full GASS observed sample, using the SDSS redshifts for the non-detections (hatched green histogram). We note that HI

[2] *http://cas.sdss.org/dr7/en/tools/search/sql.asp*
[3] *http://www.mpa-garching.mpg.de/GASS/data.php*

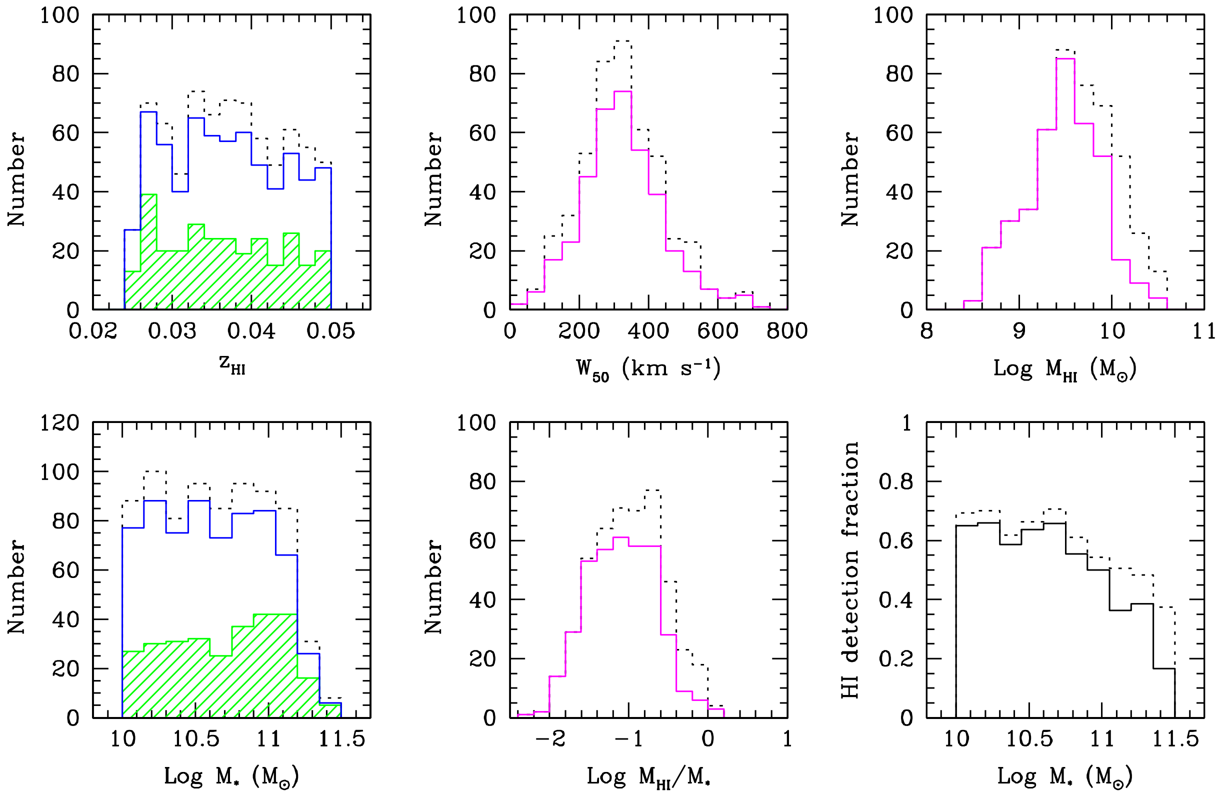

Figure 1. GASS sample properties. *Top row:* Distributions of HI redshifts, velocity widths (not corrected for inclination) and HI masses for the Arecibo detections (magenta histograms). The green hatched histogram in the left panel shows the distribution of SDSS redshifts for the non-detections (the blue histogram includes both detections and non-detections). *Bottom row:* Distributions of stellar mass (same color scheme as top left panel), gas fraction, and detection fraction (*i.e.*, the ratio of detections to total) as a function of stellar mass. The dotted histograms in all panels correspond to the representative sample, which includes gas-rich objects from ALFALFA and/or S05 archive (see text).

detections and non-detections present a similar redshift distribution. As for our previous data releases, the distribution of corrected velocity widths (which have not been deprojected to edge-on view) peaks near 300 km s^{-1}, which is the value that we assume to compute upper limits for the HI masses of the non-detections, and to estimate $T_{\rm max}$ in Table 2. The bottom left panel shows the stellar mass distribution for the observed and representative samples. The corresponding distribution for the non-detections is shown as a hatched green histogram (as for the redshift distribution, the detections are plotted on top of the non-detections). The stellar mass histogram is almost flat by survey design, as we wish to obtain similar statistics in each bin in order to perform comparisons at fixed stellar mass. As already noted in the DR1 and DR2 papers, non-detections span the entire range of stellar masses, but they are concentrated in the red portion of the NUV$-r$ space (not shown). The detection fraction, *i.e.* the ratio of detected galaxies to total, is plotted as a function of stellar mass in the bottom right panel. The detection fraction is close to 70% for $M_\star < 10^{10.7}$ M$_\odot$, and drops to ∼40% in the highest stellar mass bin.

5 GAS FRACTION SCALING RELATIONS

In this section we present the final version of the scaling relations introduced in the DR1 paper, now based on the full GASS sample. Here and in the rest of this work we use the representative sample for our analysis (unless explicitly noted).

Clockwise from the top left, Figure 2 shows how the gas mass fraction $M_{\rm HI}/M_\star$ depends on stellar mass, stellar mass surface density (defined as $\mu_\star = M_\star/(2\pi R^2_{50,z})$, where $R_{50,z}$ is the radius containing 50% of the Petrosian flux in z-band, expressed in kpc units), observed NUV$-r$ color and R_{90}/R_{50} concentration index (a proxy for bulge-to-total ratio). Small gray circles and green upside-down triangles indicate HI detections and non-detections (plotted at their upper limits), respectively. The average values of the gas fraction are overplotted as filled circles; these are computed including the non-detections, whose HI masses were set either to their upper limits (green) or to zero (red). The averages are weighted in order to compensate for the flat stellar mass distribution of the GASS sample, using the volume-limited parent sample as a reference. Briefly, we binned both parent and representative samples by stellar mass (with a 0.2 dex step), and used the ratio between the two histograms as a weight. Error bars indicate the standard deviation of the weighted averages. These results are entirely consistent with our previous findings (see also Fabello et al. 2011a and Cortese et al. 2011). In summary:
– The gas fraction of massive galaxies anticorrelates with all the quantities shown in Figure 2. The tightest corre-

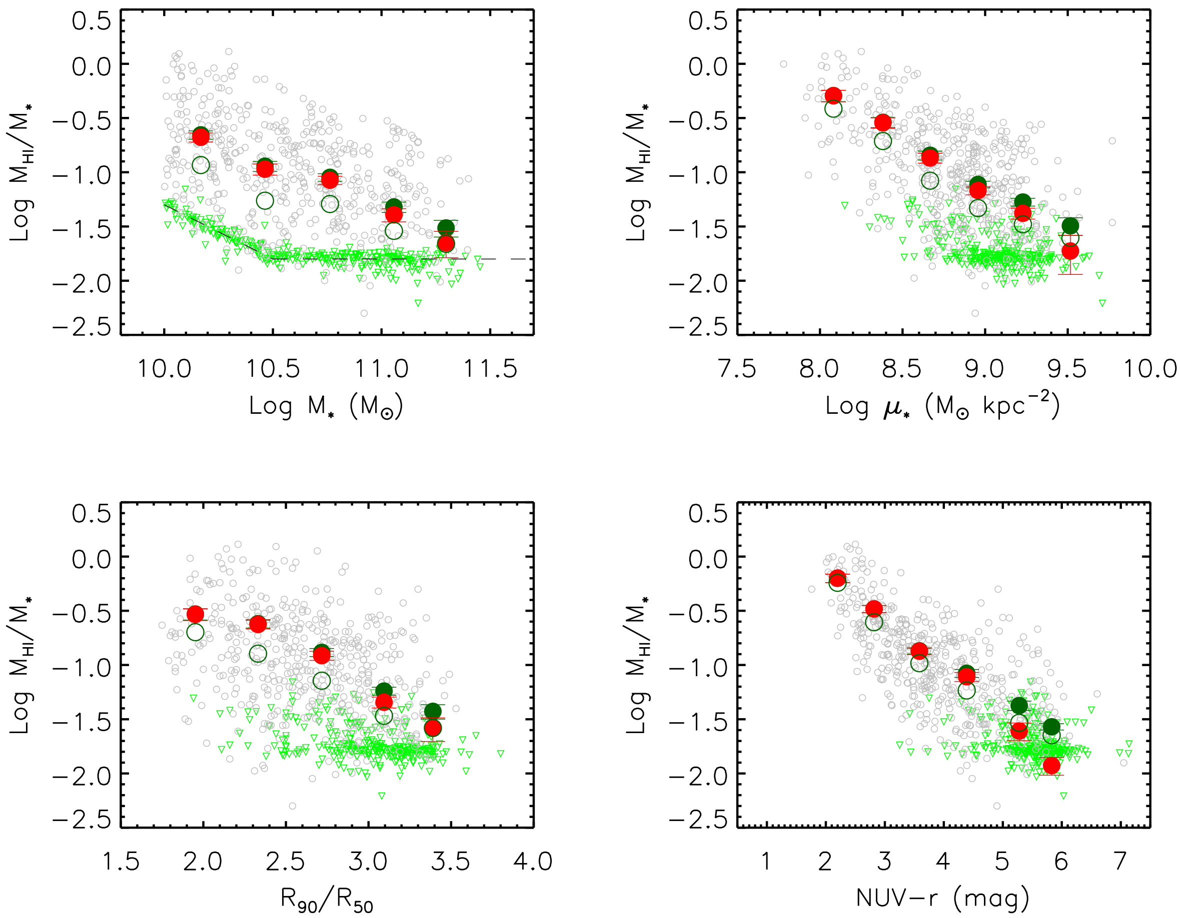

Figure 2. Average trends of HI mass fraction as a function of stellar mass, stellar mass surface density, concentration index and observed NUV−r color for the representative sample. In each panel, large filled circles indicate weighted average gas fractions (see text). These were computed including the non-detections, whose HI mass was set to either its upper limit (green) or to zero (red). Large empty circles indicate weighted averages of the logarithms of the gas fractions. Only bins including at least 10 galaxies are shown. These results are listed in Table 1. Small gray circles and green upside-down triangles indicate individual HI detections and non-detections (plotted at their upper limits), respectively. The dashed line in the top left panel shows the HI gas fraction limit of GASS.

lations are with observed NUV−r color (Pearson correlation coefficient $r = -0.69$) and stellar mass surface density ($r = -0.56$), and the weakest ones are with stellar mass ($r = -0.44$) and concentration index ($r = -0.38$).
– The non-detections are almost exclusively found at stellar mass surface densities $\mu_\star > 10^{8.5}$ M$_\odot$ kpc^{-2} and NUV−r > 4.5 magnitudes. The average gas fractions are insensitive to the way we treat the non-detections, except for the very most massive, dense and red galaxies.

We chose to compute averages of the linear gas fractions and plot their logarithms because this allows us to bracket the possible HI masses of the non-detections (between zero and their upper limits). However, as noted by Cortese et al. (2011), the distribution of HI gas fraction is closer to lognormal than Gaussian, hence averaging the logarithms seems more appropriate. In this case we can only set the non-detections to their upper limits, and the resulting weighted averages of the logarithmic gas fractions are plotted in Figure 2 as empty green circles. These are systematically smaller than the averages of the linear gas fractions (filled green circles), and the difference is larger for the stellar mass and concentration index relations, which are also the most scattered. The values of the weighted average gas fractions shown in this figure are listed in Table 1 for reference.

In our past work we introduced the *gas fraction plane*, a relation between gas mass fraction and a linear combination of NUV−r color (which is a proxy for star formation rate per unit stellar mass) and stellar mass surface density, which can be used to define what is "HI normalcy" for local massive, star-forming galaxies. The plane is obtained by fitting only the HI detections and minimizing the scatter on the y coordinate (thus, it is equivalent to a direct fit). As demonstrated by Cortese et al. (2011), the distance from the plane along the y axis strongly correlates with the HI deficiency parameter (Haynes & Giovanelli 1984) and has a similar scatter (naturally, the sample used to define the plane should be representative of unperturbed systems). This makes the gas fraction plane a very useful tool to investigate environmental effects and to identify unusually HI-rich galaxies, especially when an accurate morphological classification is not available.

We plot the gas fraction plane in Figure 3a. We refined our sample by excluding galaxies for which confusion within the Arecibo beam is certain (because their measured HI flux belongs entirely or for the most part to a companion galaxy;

Table 1. Weighted Average Gas Fractions

x	$\langle x\rangle$	$\langle M_{\rm HI}/M_\star\rangle^a$	$\langle M_{\rm HI}/M_\star\rangle^b$	$\langle log(M_{\rm HI}/M_\star)\rangle^c$	N^d
Log $M_\star$	10.17	0.221±0.020	0.210±0.020	−0.934	188
	10.46	0.114±0.012	0.107±0.013	−1.262	176
	10.76	0.090±0.007	0.084±0.008	−1.293	180
	11.06	0.048±0.005	0.041±0.006	−1.540	177
	11.30	0.031±0.005	0.022±0.006	−1.660	39
Log $\mu_\star$	8.08	0.509±0.061	0.508±0.062	−0.414	32
	8.38	0.289±0.031	0.286±0.031	−0.712	69
	8.67	0.143±0.014	0.135±0.014	−1.078	145
	8.96	0.077±0.005	0.068±0.006	−1.330	268
	9.23	0.053±0.004	0.042±0.005	−1.480	218
	9.52	0.032±0.006	0.019±0.007	−1.605	24
R_{90}/R_{50}	1.95	0.295±0.035	0.293±0.036	−0.697	50
	2.33	0.240±0.021	0.237±0.022	−0.896	160
	2.72	0.131±0.011	0.122±0.012	−1.145	217
	3.09	0.057±0.005	0.045±0.005	−1.469	272
	3.39	0.037±0.006	0.026±0.006	−1.580	60
NUV−r	2.20	0.632±0.057	0.632±0.057	−0.242	24
	2.82	0.329±0.025	0.329±0.025	−0.605	108
	3.59	0.135±0.009	0.134±0.009	−0.983	139
	4.39	0.084±0.007	0.078±0.007	−1.235	131
	5.28	0.042±0.004	0.025±0.005	−1.533	194
	5.83	0.027±0.002	0.012±0.002	−1.648	145

Notes. — [a]Gas fraction weighted average; HI mass of non-detections set to upper limit. [b]Gas fraction weighted average; HI mass of non-detections set to zero. [c]Weighted average of logarithm of gas fraction; HI mass of non-detections set to upper limit. [d]Number of galaxies in the bin.

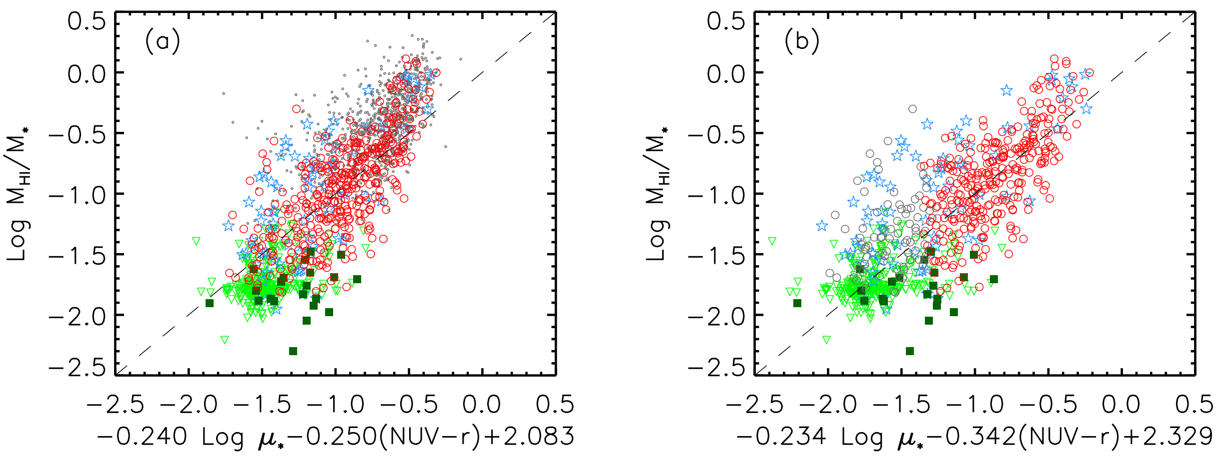

Figure 3. Gas fraction plane, a relation between HI mass fraction and a linear combination of stellar mass surface density and observed NUV−r color. (*a*) Relation obtained using all the HI detections in the GASS representative sample (red circles) that are not confused (blue stars) or below the nominal gas fraction limit of GASS (dark green squares). Green upside-down triangles are non-detections, and galaxies meeting GASS selection criteria that have been cataloged by ALFALFA to date are shown as gray dots. (*b*) Relation obtained using only the subset of detected galaxies with NUV−$r\leq$ 4.5 mag (red circles). Gray circles indicate the remaining HI detections; green and blue symbols are as in (a).

these objects are marked as blue stars) and galaxies with measured gas fractions below our survey limit[4] (squares).

[4] Figure 2 (top left panel) shows a few HI detections below the nominal gas fraction limit of GASS (dashed line). As explained in the DR1 paper (footnote 6), the main reasons for this are that (i) the expected gas fraction limit assumes a 5σ signal with velocity width of 300 km s^{-1} (hence galaxies with smaller widths and/or face-on might be detected with higher signal to noise), and (ii) we never integrate less than 4 minutes (but, at large stellar masses, the gas fraction limit can be reached in as little as 1 minute).

For comparison, we also show the full set of ALFALFA galaxies meeting GASS selection criteria that have been cataloged to date (Haynes et al. 2011, gray dots), and that comprise the most HI-rich systems in the GASS volume. The coefficients of the gas fraction plane are noted on the x axis of the figure. These have slightly changed with respect to the DR2 version (Log $M_{\rm HI}/M_\star = -0.338$ Log $\mu_\star$ -0.235 NUV$-r$ $+2.908$), but the two solutions are entirely consistent: the mean difference between the two gas fraction predictions is -0.023 dex, with a standard deviation of 0.027 dex. The rms scatter of the plane in Log $M_{\rm HI}/M_\star$ is now 0.292 dex (it was 0.319 dex for DR2).

As discussed in the DR2 paper, the validity of the gas fraction plane breaks down in the region where the contribution of the HI non-detections (which are excluded from the sample used to define it) becomes significant. Therefore we computed another gas fraction plane relation using only galaxies with NUV$-r \leq 4.5$ mag, which is presented in Figure 3b. Over its interval of validity, this relation has slightly smaller scatter (0.281 dex) than our original plane in (a). The relation in (b) should be preferred to predict gas fractions of massive galaxies on the star-forming sequence. In any other case we recommend to use the relation in (a) because it is based on the full sample of detections, rather than on a subset, and spans the entire range of NUV$-r$ colors and stellar mass surface densities covered by massive galaxies.

In summary, the average scaling relations have not significantly changed with respect to our previous data releases, except for the fact that the errorbars are of course smaller. However, we can now take advantage of our increased statistics to investigate second order effects, such as the dependence of the gas content on the environment *at fixed stellar mass*, which would not be feasible without the full survey sample.

6 EFFECT OF ENVIRONMENT ON THE GAS CONTENT OF MASSIVE GALAXIES

6.1 Group catalog and halo masses

Here we describe briefly the group catalog that we used to characterize the environment of GASS galaxies.

Yang et al. (2007) compiled a catalog of galaxy groups based on SDSS DR4, using what they refer to as a halo-based group finder. Their algorithm is iterative and includes the following steps: (a) identify potential group centers using two methods; (b) compute the characteristic luminosity of each tentative group (*i.e.* the combined luminosity of all group members brighter than a threshold); (c) estimate the mass, size and velocity dispersion of the dark matter halo associated with it (initially using a constant mass-to-light ratio for all groups); (d) reassign galaxies to each tentative group based on its halo properties; (e) recompute group centers and iterate until there is no further change in the group memberships.

Once the group catalog was finalized, Yang et al. (2007) assigned halo masses via abundance matching, assuming the halo mass function of Warren et al. (2006). In practice, they associated the characteristic luminosity or stellar mass of a group to a halo mass by matching their rank orders.

They applied the same algorithm to SDSS DR7 (Yang et al. 2012), and generated two sets of group catalogs[5], one based on Petrosian magnitudes and one based on model magnitudes. We use the latter for our environmental analysis, and adopt halo masses $M_{\rm h}$ obtained by rank ordering the groups by stellar mass, following *e.g.* Woo et al. (2013). The catalog also classifies galaxies as centrals or satellites.

We note that 10 out of 760 galaxies in our GASS representative sample are not included in the group catalog, and are thus excluded from our environmental analysis. Lastly, very small groups are not assigned halo masses in the group catalog, and this affects 110 of the remaining galaxies. However, this is not an issue for our analysis, as we will divide our sample into three intervals of halo mass, and include those 110 galaxies in the lowest $M_{\rm h}$ bin (Log $M_{\rm h}/{\rm M}_\odot < 12$).

6.2 The environment of GASS galaxies

We begin our analysis by asking what are the typical environments probed by the GASS galaxies. In order to establish this, we crossed-matched both our parent and representative samples with the galaxies in the group catalog described above. We remind the reader that the parent sample is the super-set of all the 12,006 galaxies in SDSS DR6 that meet the GASS selection criteria (stellar mass, redshift cuts and located within the final ALFALFA footprint), out of which we extracted those that we observed with Arecibo. As such, the parent sample is volume-limited and reasonably complete in stellar mass above 10^{10} M$_\odot$ (aside from SDSS fiber collision issues).

We plot the normalized distribution of $N_{\rm gal}$, the number galaxies in each group, in Figure 4a, for both parent (black) and GASS (red) samples. Galaxies with $N_{\rm gal} = 1$ are isolated, and we generically call "group" any structure with two or more members. According to this definition, about half of the GASS parent sample galaxies are isolated (48%; the percentage is 43% for the representative sample), and about half are in groups. The richest structure in our survey volume is represented by the far outskirts of the Coma cluster (with $N_{\rm gal} = 623$; with a median redshift of 0.0229, the center of Coma is just below our redshift cutoff). Compared with the parent sample, the GASS sample probes the same environments in terms of group richness. The distribution of halo masses for the GASS sample is shown in panel (b); the 110 galaxies in small groups mentioned above, which do not have halo masses assigned in the group catalog, are not plotted. As a result of our survey strategy (specifically, the fact that we selected a set of galaxies that balanced the distribution across stellar mass), this histogram is less peaked at low $M_{\rm h}$ than the corresponding one for the parent sample (not shown), but most importantly the two samples span the same interval of halo mass.

Lastly, Figure 5 shows the relation between stellar and halo masses for the galaxies in our sample with assigned halo mass; we color-coded the points to indicate central galaxies in isolation (red) or in groups (orange) and satellites (blue). Our sample does not include central galaxies in the most massive halos, because such systems are rare.

Having established that the GASS sample is representative of the parent sample also in terms of environment,

[5] Available at *http://gax.shao.ac.cn/data/Group.html*

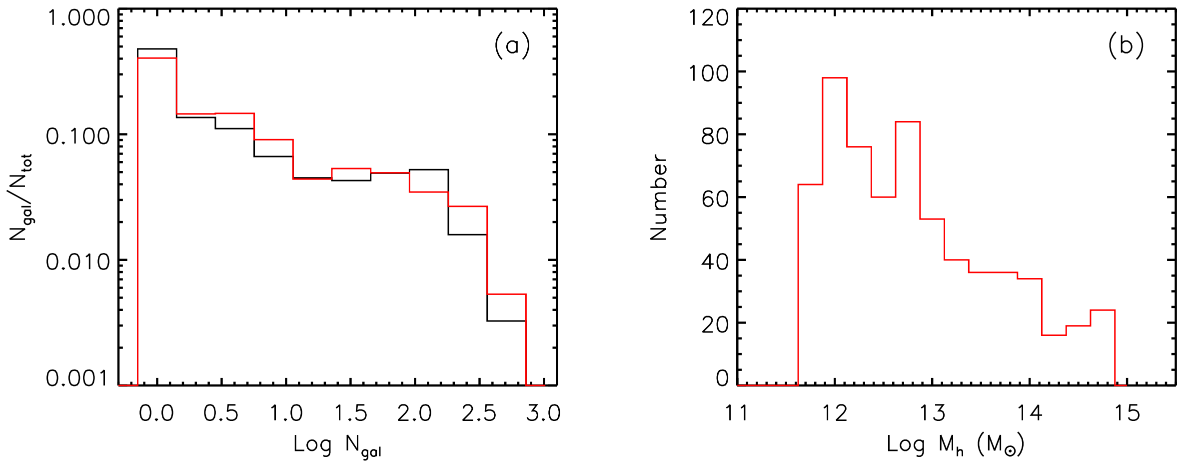

Figure 4. (*a*) Normalized distribution of $N_{\rm gal}$, the number of galaxies in each group, for the GASS parent and representative samples (black and red respectively; see text). (*b*) Distribution of halo masses for the representative sample. This histogram does not include 110 galaxies in very small groups that do not have halo masses assigned in the group catalog.

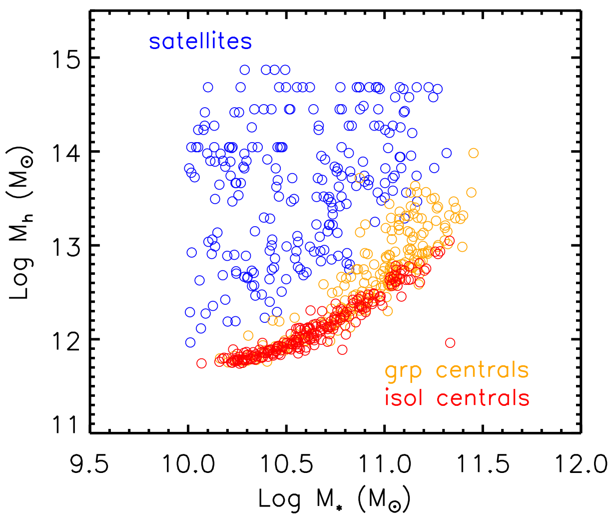

Figure 5. Relation between halo and stellar masses for central galaxies in isolation (red circles) or in groups (orange) and for satellite galaxies (blue) in the GASS sample.

it is important to note that our survey only probes low to intermediate density environments (as we discuss later, our most massive halo bin is dominated in number by groups with an average of 20 members). There are no rich clusters, such as Virgo or Coma, in our survey volume. Both the limited dynamic range in galaxy density and our relatively high gas fraction limit (see below) do not allow us to investigate the most dramatic cases of HI stripping, which are well known to occur in the central regions of clusters and rich groups (Cayatte et al. 1990; Bravo-Alfaro et al. 2000; Boselli & Gavazzi 2006). The reader should bear this in mind when interpreting our results in the following sections. Instead, GASS is optimally suited to look for evidence of quenching mechanisms acting on the HI and stellar content of massive galaxies *in the group environment* and from a statistical point of view.

6.3 Quantifying the suppression of HI gas

If environmental mechanisms play an important role in removing cold gas from galaxies, it is reasonable to expect that the HI content of the affected galaxies will be lower than that of similar (in terms of structural and star formation properties), but unperturbed, systems. This idea is behind the definition of the classic "HI deficiency" parameter (Haynes & Giovanelli 1984), which has been successfully used to demonstrate that galaxies in the densest environments have their HI gas content largely reduced, most likely by ram pressure stripping by the dense intracluster medium (Giovanelli & Haynes 1985; Solanes et al. 2001; Chung et al. 2007; Vollmer 2009; Cortese et al. 2011).

As mentioned in Section 5, the gas fraction plane is an excellent tool to investigate environmental effects, and the distance from the best fit relation has been shown to be equivalent to the HI deficiency for galaxies in the Virgo cluster (Cortese et al. 2011). Indeed, the plane is a reformulation of the HI deficiency relation in terms of quantities (stellar mass surface density and NUV$-r$ color, which is a proxy for specific star formation rate) that have a more immediate physical interpretation (compared to morphological classification and optical diameter) and are more easily applicable to large, modern data sets. However, we show below that GASS does not probe the HI-deficient regime, hence the gas fraction plane is of limited use to find evidence for gas suppression *within our own sample.*

We measured the "HI richness" parameter for our galaxies, defined as the difference between the logarithms of the measured gas fraction and that predicted by the relation in Figure 3a. HI-poor galaxies have smaller gas fractions than predicted, *i.e.* a negative HI richness. Figure 6a shows the distribution of the HI richness parameter for HI-detected galaxies in three bins of halo mass, as indicated on the top left; panel (b) shows the same histograms for the non-detections. These distributions clearly illustrate that the non-detections pile up at HI richness between -0.5 and -0.2, but they start to be important already in the "HI-normal" regime, *i.e.* near HI richness of zero. Keeping in mind that the scatter of the plane is 0.3 dex, only galaxies with gas

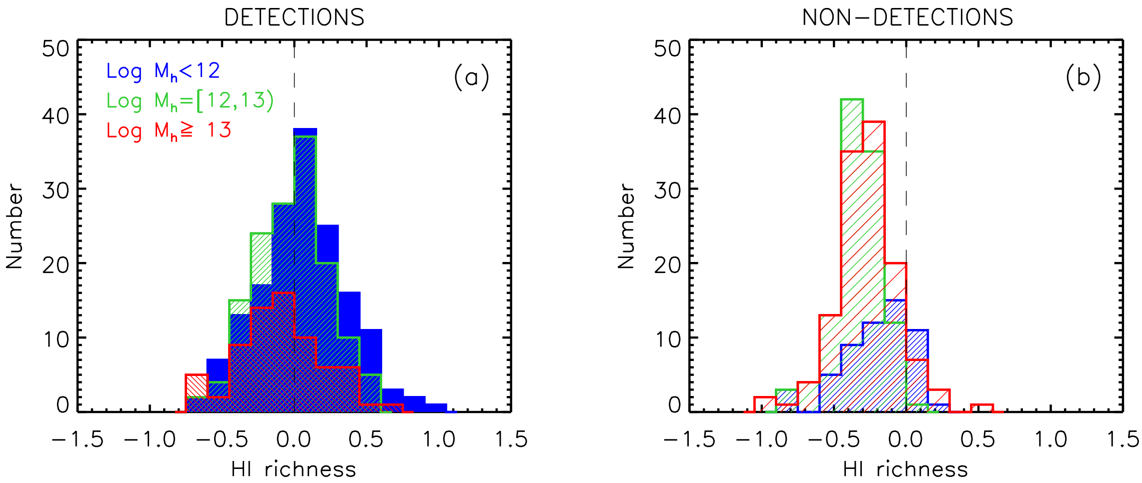

Figure 6. (*a*) Distribution of HI richness, *i.e.* the difference between measured and expected gas fractions, for HI-detected galaxies. The sample is divided into three bins of halo mass, as indicated in the top left corner. (*b*) Same distributions for galaxies that were not detected in HI (plotted at their upper limits), together with detections below the gas fraction limit of GASS. The colors correspond to the same halo mass bins indicated on the top left corner of panel (a).

fractions that deviate from the predicted values by at least that amount (or more conservatively 0.5 dex, as usually assumed for the HI deficiency parameter) should be called HI-deficient (or HI-excess) systems. Thus, because our survey gas fraction limit is so close to the start of the HI-deficient regime, it turns out that the plane is much better suited to characterize the HI-excess systems in the GASS redshift interval than the HI-poor ones (since for the latter we only have upper limits).

The sample used to define the gas fraction plane is indeed representative of unperturbed systems, because it does not include the HI non-detections, which are the galaxies affected by the environment. We checked this by computing the gas fraction plane using only HI detections in the $M_{\rm h} < 10^{12}$ M$_\odot$ bin, which gives a solution that is indistinguishable from that in Figure 3a. The highest halo mass bin, $M_{\rm h} \geq 10^{13}$ M$_\odot$, includes only 70 detections, and although the corresponding gas fraction plane is slightly offset towards lower $M_{\rm HI}/M_\star$ with respect to the "undisturbed" one, the difference is statistically not significant (the mean difference between the two solutions is 0.17 dex, with a standard deviation of 0.08 dex, and the scatters of the planes are both 0.3 dex; see Fig. 6a).

Because we cannot quantify the degree of HI removal in individual HI-deficient systems at the distances probed by GASS, and also our statistics become limited when we start binning galaxies by stellar mass and environment, we do not attempt to compute the average gas fraction scaling relations presented in Figure 2 in bins of environmental density (see however Section 7). This approach was adopted by Cortese et al. (2011) to compare Virgo cluster and HI-normal galaxies, and was successful because the more nearby Herschel Reference Survey (HRS; Boselli et al. 2010) sample includes HI detections and more stringent upper limits in the HI-deficient regime.

Instead, as already done by Kauffmann et al. (2012) for our sample, we adopt the gas fraction threshold of GASS as the nominal division between HI-normal and HI-deficient systems, and look for trends in the HI detection fractions as a function of galaxy properties and environment. As discussed above, this is entirely justified by the fact that the detection limit of GASS roughly corresponds to the gas fraction separating HI-normal from HI-deficient massive galaxies. In order to compute meaningful detection fractions we excluded from our sample the objects for which confusion within the Arecibo beam is certain (15% of the HI detections, indicated by blue stars in Fig. 3; these galaxies were not included in Fig. 6). Also, as already noted, the few HI detections with gas fraction below the GASS limit (dark green squares in Fig. 3) are effectively HI-poor systems, and thus are counted as non-detections.

6.4 Suppression of HI gas in the group environment

In this section we investigate the relation between gas content and other galaxy properties in different environments, looking for possible evidence of gas removal at the highest densities. We use dark matter halo masses as our environmental estimator and, for the reasons explained above, we resort to using detection fractions to characterize the average gas content in a given bin of, *e.g.*, stellar and halo mass.

Figure 7 shows how the average HI detection fraction, *i.e.* the ratio of detections to total in each bin, $N_{\rm det}/N_{\rm tot}$, changes as a function of stellar mass, stellar mass surface density and concentration index in the first column, and NUV$-r$, $g-i$ colors in the second one. Blue and red circles indicate galaxies that inhabit dark matter halos with masses below and above 10^{13} M$_\odot$, respectively. We initially divided our sample into the same three bins of halo mass used for Figure 6, which contain similar numbers of galaxies (see also Fig. 4). We indicate the average detection fractions in the two lowest halo mass intervals, Log $M_{\rm h}$/M$_\odot < 12$ and $12 \leq$ Log $M_{\rm h}$/M$_\odot < 13$, with dashed purple and dot-dashed green lines, respectively. As can be seen, there is no significant difference between these two halo mass bins in any of these plots (the only apparent exception would be the first stellar mass bin in the top left panel, but notice that the green data

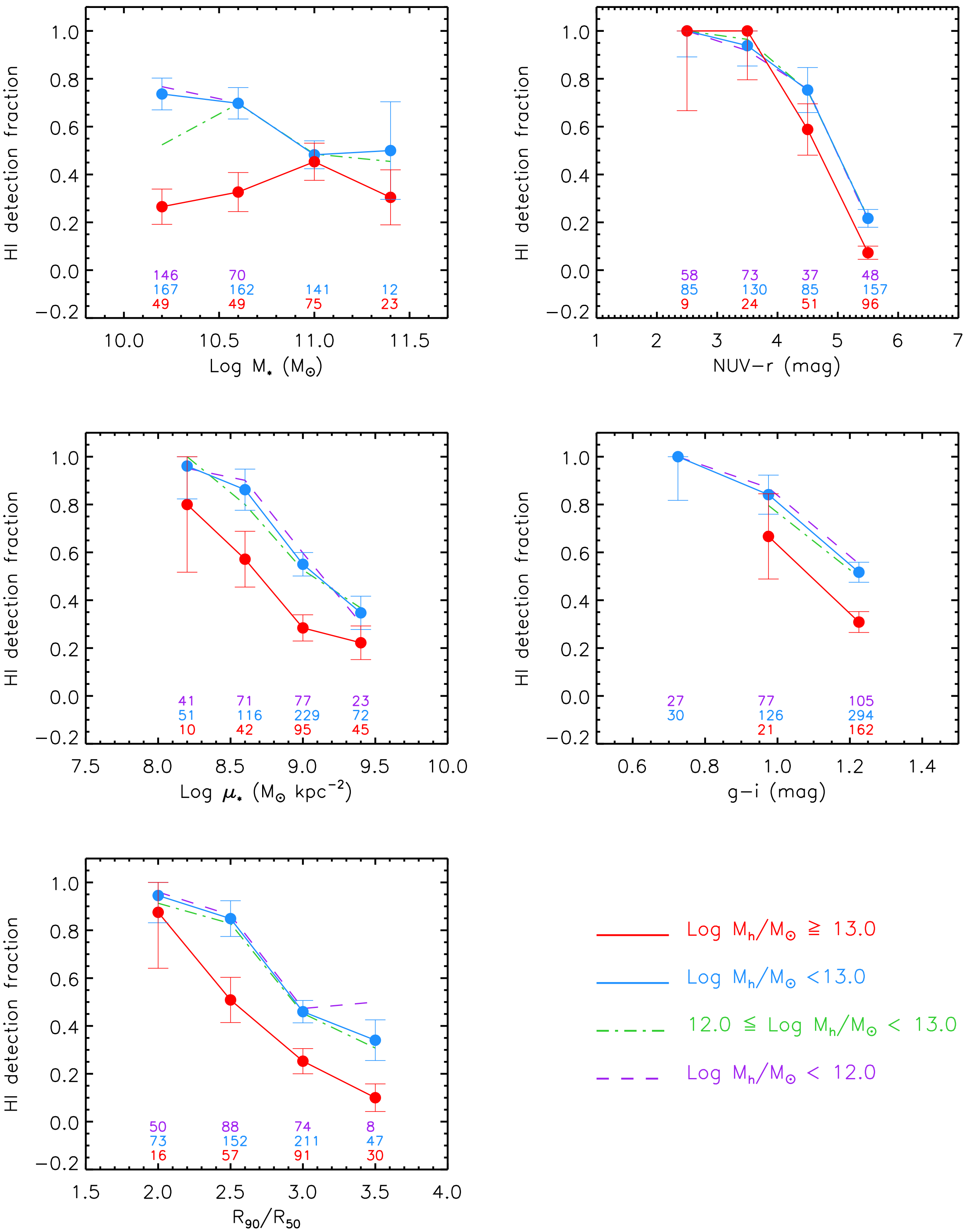

Figure 7. HI detection fraction of GASS galaxies plotted as a function of stellar mass, stellar mass surface density and concentration index in the first column, and NUV$-r$, $g-i$ colors in the second one. The data in each panel are divided into two bins of halo mass, below and above 10^{13} $M_\odot$ (blue and red, respectively), as indicated in the bottom right corner of the figure. Large circles are average detection fractions, and the numbers in each panel indicate the total number of galaxies in each bin (only bins with $N_{\rm tot} \geq 5$ are shown); errorbars are Poissonian (truncated at detection fraction of 1 if necessary). We also show the results for a finer division of the lowest halo mass interval, *i.e.* Log $M_{\rm h}/M_\odot < 12$ (dashed purple line) and $12 \leq$ Log $M_{\rm h}/M_\odot < 13$ (dot-dashed green line). Notice that halos with $M_{\rm h} < 10^{12}$ $M_\odot$ are populated only by galaxies in the lowest two stellar mass bins.

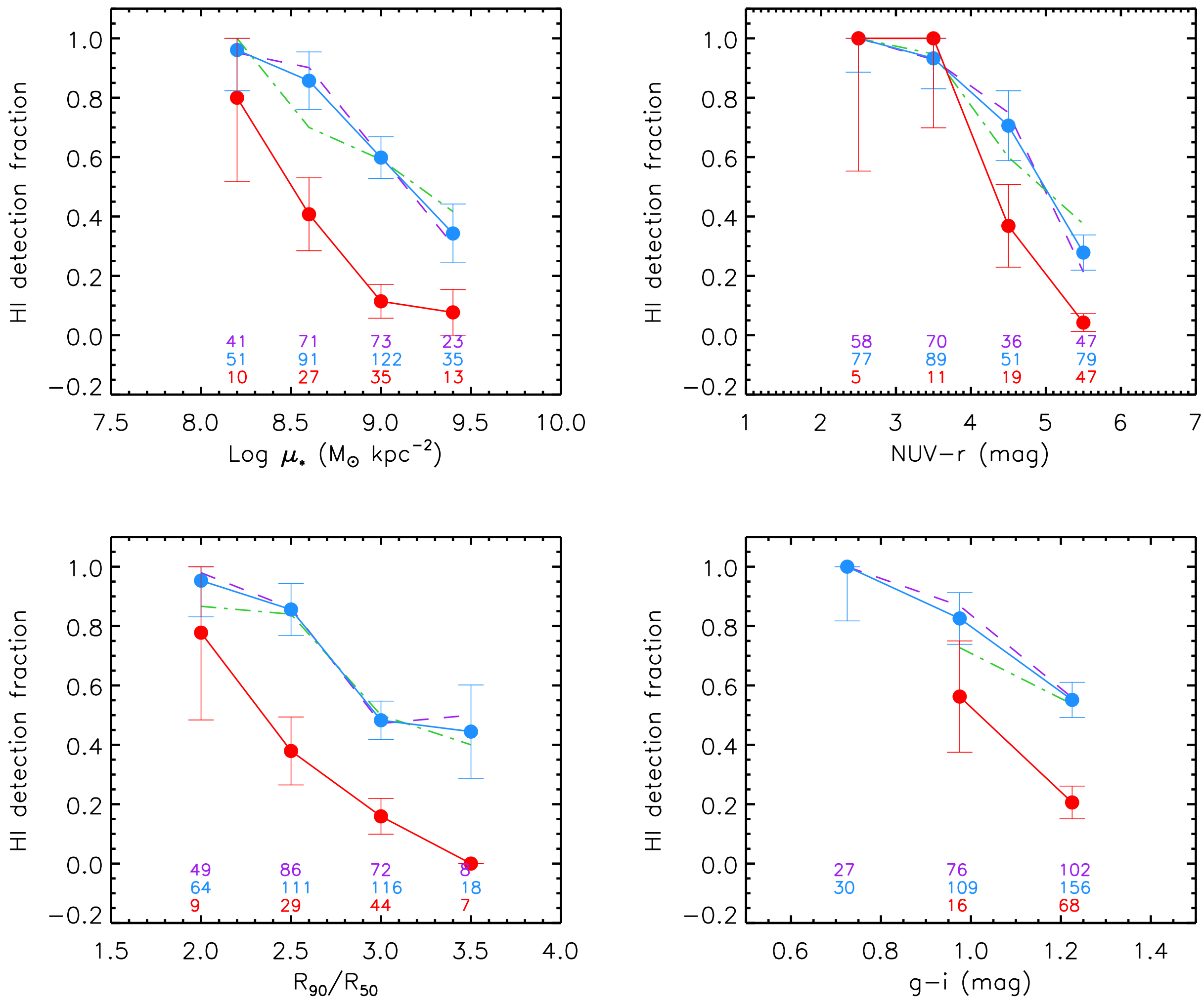

Figure 8. HI detection fraction plotted as a function of stellar mass surface density, concentration index, NUV$-r$, and $g-i$ colors for the subset of galaxies with stellar mass Log $M_\star/M_\odot < 10.75$. Symbols and colors are the same as in Figure 7.

point is based on 20 objects only), so we combined them to increase statistics.

The top left panel of Figure 7 is the main result of this work, and clearly shows that the HI content of massive galaxies that live in dark matter halos with $M_h \gtrsim 10^{13}$ $M_\odot$ is significantly reduced compared to that of galaxies *with the same stellar mass*, at least below $M_\star \sim 10^{11}$ $M_\odot$. We do not see a difference at larger stellar mass, which seems to suggest that the environment has no detectable effect on the most massive galaxies in our sample. We will come back to this point later. Because GASS does not contain any very rich group or clusters (and indeed 2/3 of the halos in our highest density bin have masses between 10^{13} and 10^{14} $M_\odot$; see also Fig. 4b), our result implies that *the suppression of* HI *is modulated by the environment even at the intermediate densities probed by our sample.*

The other two panels in the first column of Figure 7 show that the suppression of HI gas in the most massive halos in our sample can be seen also at fixed stellar mass surface density and concentration index, both proxies of stellar morphology (higher values of $\mu_\star$ and R_{90}/R_{50} correspond to bulge-dominated systems).

The plots on the right column of Figure 7 compare the detection fractions in different environments at fixed galaxy color. Interestingly, we find that galaxies in more massive halos have lower gas content only for NUV$-r$ colors redder than $\sim$4 mag. In the stellar mass range probed by GASS, this color corresponds to the red edge of the blue cloud and the start of the green valley (Wyder et al. 2007), suggesting that a fraction of our gas-poor systems have not yet completely stopped forming stars. The presence of gas-poor, but still star-forming, galaxies may indicate that the timescale of the gas removal is significantly shorter than the timescale necessary for the NUV$-r$ color to reach values typical of the red sequence galaxies, *i.e.* NUV$-r\sim$5.5 mag ($\sim$1 Gyr, see also Fig. 4 in Cortese et al. 2011).

Less enlightening is the variation of HI detection fraction with $g-i$ color. Although we find that, at fixed $g-i$ color, galaxies in high mass halos have significantly lower detection fractions, this result does not provide any additional insights into the physical process at play. Indeed, massive galaxies generally lie on the optical red sequence regardless of their current star formation activity (Wyder et al. 2007; Cortese 2012), thus their optical colors are saturated — they cannot significantly redden following further quenching of the star formation.

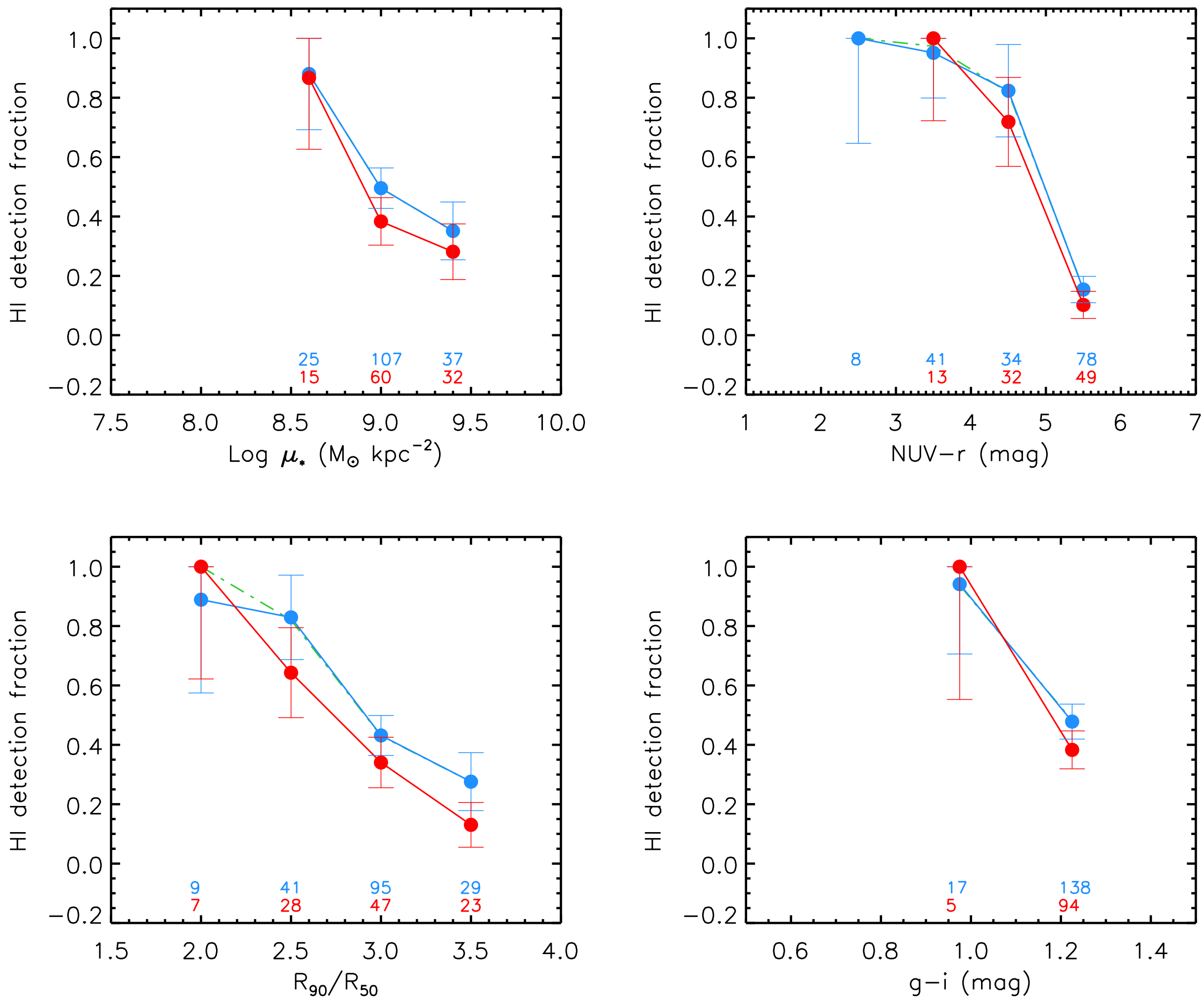

Figure 9. Same as Figure 8 for galaxies with larger stellar mass (Log $M_\star/M_\odot \geq 10.75$).

We look in more detail at the properties of the lower stellar mass galaxies, for which we see a clear difference of gas content above and below $M_h \sim 10^{13}$ $M_\odot$, in Figure 8. Here the detection fraction is shown as a function of stellar mass surface density, concentration index, NUV$-r$, and $g-i$ colors for the subset of galaxies with $M_\star < 10^{10.75}$ $M_\odot$. For comparison, the same plots are presented in Figure 9 for the galaxies with stellar mass above that limit. As expected, the offsets seen in Figure 7 become larger when we restrict the sample to the lower stellar mass bin. This is particularly interesting in the case of the NUV$-r$, since it slightly reinforces our timescale argument. Overall, the larger differences shown in Figure 8 are simply due to the exclusion of the most massive galaxies, which have lower gas fractions (see Fig. 2). With regard to the galaxies with stellar mass $M_\star \geq 10^{10.75}$ $M_\odot$, we caution the reader that the median galaxy is a non-detection, hence we cannot conclude that the environment is not acting on the gas reservoir of those systems – our survey might simply not be sensitive enough to detect environmental effects on these already gas-poor galaxies.

The trends in detection fraction observed when we divide the sample according to halo mass are present also when we describe the environment in terms of central and satellite galaxies. Figure 10 repeats the panels of Figure 7, but now blue and red circles represent central and satellite galaxies, respectively. Purple dashed and green dot-dashed lines indicate central galaxies in isolation and in groups, respectively. There is no significant difference between the two classes of central galaxies and, at fixed stellar mass (at least below $\sim 10^{11}$ $M_\odot$), satellite galaxies have lower gas content on average than centrals. This is completely consistent with the result shown in the corresponding panel of Figure 7, as expected from the fact that central galaxies in this stellar mass interval are mostly isolated (see Fig. 5). Overall, the offsets in detection fraction are slightly smaller when we divide the sample into central and satellites rather than by halo mass (mostly because satellite galaxies are found at all halo masses, not only in halos with $M_h > 10^{13}$ $M_\odot$), but they are still significant.

It would be very interesting to know whether the observed decrease of HI content is primarily dependent on the dark matter halo mass or on the nature of the galaxy as central vs. satellite. This is because there could be physically distinct processes that link HI content separately to these two different environmental descriptors (*e.g.* Weinmann et al. 2006). Unfortunately, our data do not allow us to disentangle between the two scenarios. As can be seen

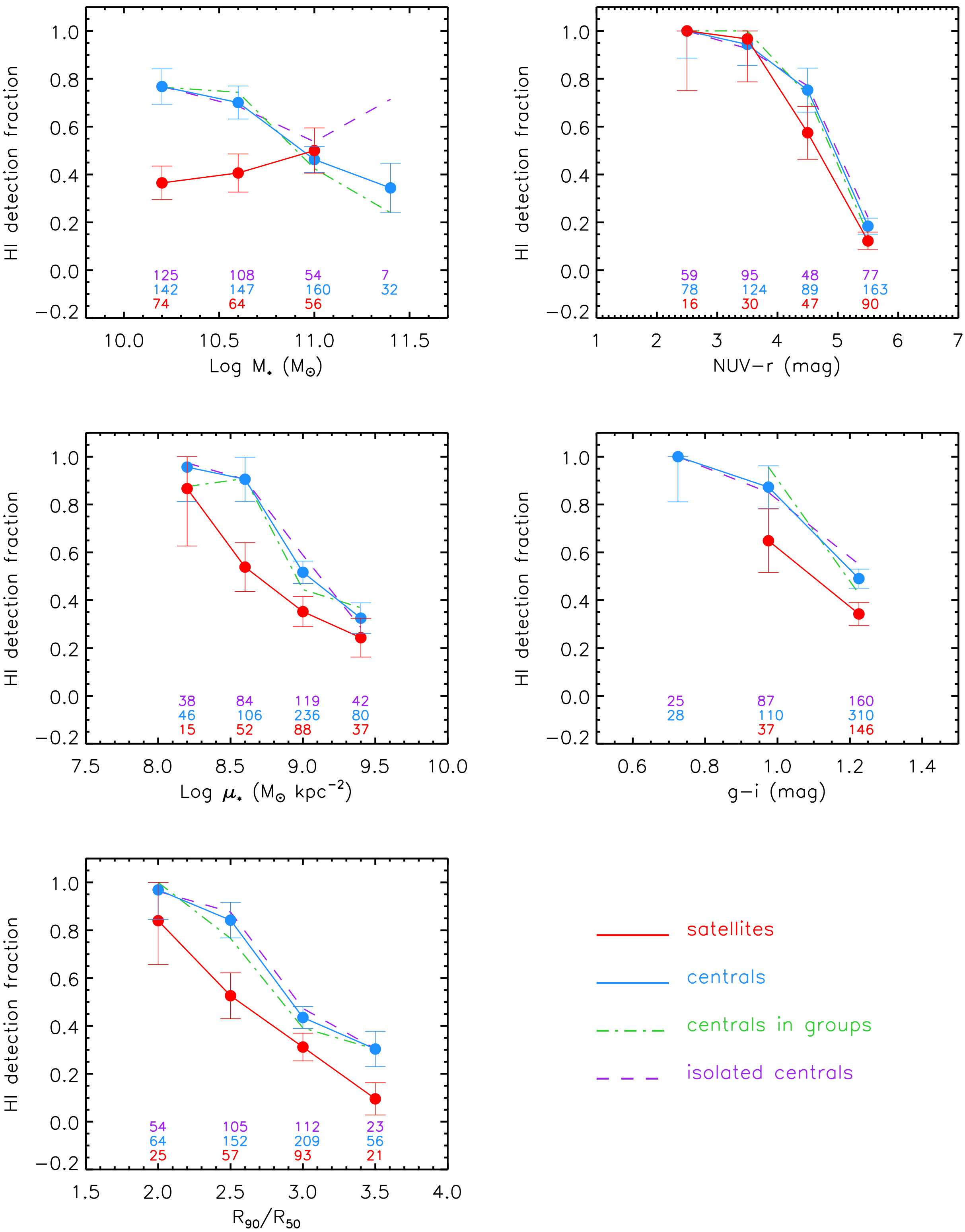

Figure 10. The HI detection fraction of GASS galaxies is plotted here as a function of the same quantities seen in Figure 7, but now the data are divided into centrals (blue) and satellites (red). The purple dashed and green dot-dashed lines indicate central galaxies in isolation and in groups, respectively.

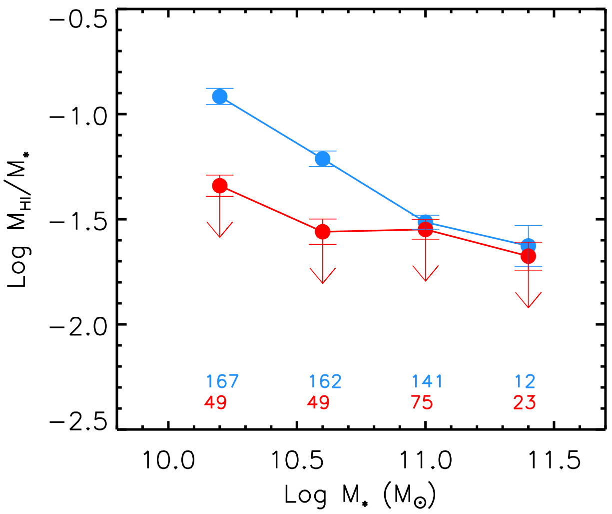

Figure 11. Averages of HI gas fraction logarithms versus stellar mass. The data are divided into two bins of halo mass, above and below 10^{13} M$_\odot$ (red and blue, respectively). Downward arrows indicate upper limits (because the corresponding bins are dominated by HI non-detections). The numbers at the bottom indicate the total number of galaxies in each bin (only bins with $N_{\rm tot}\geq 5$ are shown); errorbars are errors on the mean.

by simply drawing a horizontal line at Log $M_{\rm h}/{\rm M}_\odot = 13$ in Figure 5, there are almost no central galaxies above that threshold and there are only very few satellites below. Therefore, although splitting the sample by halo mass is not the same as splitting by centrals vs. satellites, once we bin the galaxies to reach sufficient statistics the two classifications become almost the same, and the issue ends up being just a semantic one.

7 DISCUSSION AND CONCLUSIONS

In this work we have used the full GASS data set, which includes HI measurements for ∼800 galaxies with stellar masses $10 < {\rm Log}(M_\star/M_\odot) < 11.5$ and redshift $0.025 < z < 0.05$, to study how the gas content of massive systems depends on environment *at fixed stellar mass*. We characterized the environment of GASS galaxies by their dark matter halo mass, obtained from the SDSS group catalog of Yang et al. (2007, updated to SDSS DR7) using the abundance matching technique.

The key new result of our analysis is that we obtained clear evidence for suppression of HI gas at fixed stellar mass (at least below $M_\star{\sim}10^{11}$ M$_\odot$) for galaxies that are located in groups with halo masses $M_{\rm h}\gtrsim 10^{13}$ M$_\odot$. The effect is seen also at fixed stellar morphology (*i.e.*, $\mu_\star$ and R_{90}/R_{50}), and when we divide our sample according to central/satellite classification. As shown in Figure 4, our most massive halo bin is dominated by systems with $M_{\rm h}$ between 10^{13} and 10^{14} M$_\odot$. In the SDSS group catalog, such halos include up to ∼60 members (20 on average), whereas smaller halos include up to 10 members (2 on average). Thus, the environment where we detect a decrease of HI gas content in massive galaxies is that of moderately rich groups, and we are certainly not probing the cluster regime.

We attempt to quantify the amount of gas depletion for our sample in Figure 11. We computed average gas fractions in bins of stellar and halo mass, including the non-detections at their upper limits. As in Figures 7-9, blue and red lines indicate dark matter halos with masses below and above 10^{13} M$_\odot$, respectively. The result is qualitatively consistent with what shown in the top left panel of Figure 7 for the average detection fractions: at fixed stellar mass (at least below $\sim 10^{11}$ M$_\odot$), the HI content of galaxies in more massive halos is systematically lower. In the first two stellar mass bins, the difference of HI gas fractions between galaxies in halos with masses below and above 10^{13} M$_\odot$ is ∼0.4 dex (linear gas fractions drop from 12% to 5% in the first $M_\star$ bin, and from 6% to 3% in the second one). As indicated by the red arrows, the average gas fractions for the $M_{\rm h}\geq 10^{13}$ M$_\odot$ bins (and those for $M_\star\geq 10^{11}$ M$_\odot$ regardless of halo mass) are dominated by non-detections, and thus must be considered upper limits. This gives us a lower limit on the typical amount of HI suppression in groups, which is at least a factor of two compared to galaxies in smaller halos, but prevents us from a more precise quantification. This is the reason why we decided to carry out our analysis in terms of detection fractions instead of gas fractions.

As expected, the decrease of HI content measured in the group environment for our sample, 0.4 dex, is smaller than what observed in higher density regions, such as rich galaxy clusters. For instance, HI-deficient Virgo members with stellar masses $\sim 10^{10} - 10^{10.7}$ M$_\odot$ have gas fractions that are 0.8 dex smaller than HI-normal galaxies in the HRS (see table 1 in Cortese et al. 2011). Galaxies in more massive clusters such as Coma have more extreme levels of HI deficiency (Solanes et al. 2001).

It is interesting to determine whether the star formation properties of the galaxies for which HI has been reduced are affected as well. Figure 12 shows the running averages of the specific star formation rates versus stellar mass for our sample, binned by halo mass as in Figure 11. The star formation rates were computed from our NUV photometry as in Schiminovich et al. (2010). As for the gas, we see a quenching of the star formation in the group environment (at least for galaxies with stellar mass less than $\sim 10^{11}$ M$_\odot$). This is in qualitative agreement with optical studies, which established that the star formation properties of galaxies are affected by the environment well before reaching the high-density regimes that are typical of clusters (*e.g.* Lewis et al. 2002; Gómez et al. 2003). A detailed comparison with such studies is difficult, as sample selections and environmental descriptors vary widely, and we specifically targeted only massive galaxies.

We can think of two main scenarios to explain the observed suppression of HI content in group galaxies: direct removal of HI from the disk and starvation (Larson, Tinsley & Caldwell 1980). In the first case, the HI is directly affected and removed from the galaxy disk by one or more environmental mechanisms (*e.g.*, ram pressure or gravitational interactions). In the second case, the lower HI mass fraction in the more massive halos (and in satellites vs. centrals) is due to the group environment disrupting the accretion of the infalling, pristine gas, which, if allowed to reach the galaxy disk, would subsequently replenish its HI reservoir. However, it seems unlikely that starvation alone could explain both the HI suppression and the difference of gas content at fixed specific star formation rate seen in our

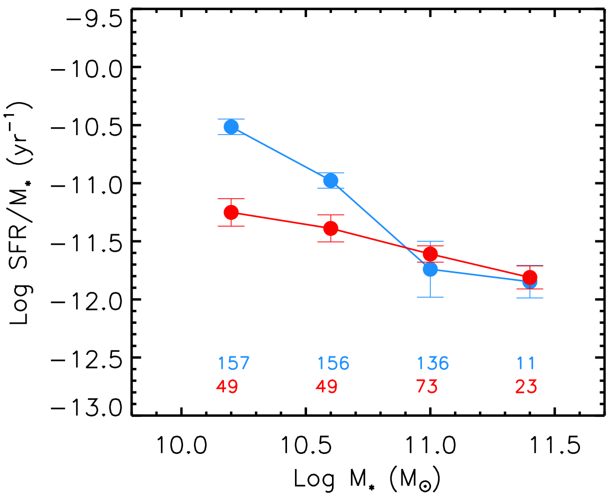

Figure 12. Average specific star formation rates are plotted as a function of stellar mass for two bins of halo mass (symbols and colors as in Fig. 11).

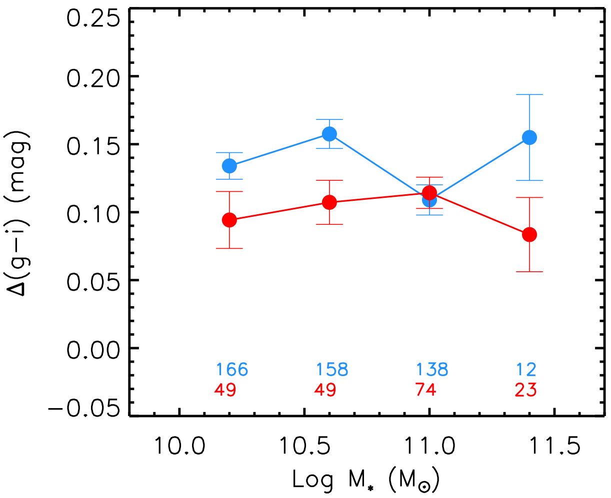

Figure 13. Average $g-i$ color gradients, defined as the difference between inner and outer $g-i$ colors, versus stellar mass for two bins of halo mass (symbols and colors as in Figures 11 and 12).

data. If the supply of infalling gas is stopped and no other external mechanisms are at play, then the HI in the galaxy will be consumed by star formation, and the two quantities should track each other and decrease on the same timescale (Boselli et al. 2006; Cortese et al. 2011). Instead, Figure 8 shows that, at fixed NUV$-r$ color (*i.e.*, at fixed specific star formation rate), the HI content of galaxies in more massive halos is systematically lower, at least in objects with stellar masses less than 10^{11} M$_\odot$. This supports a scenario in which an environmental mechanism acting directly on the cold gas reservoir is needed to explain our findings. We will assume that this is the case in the remainder of this section.

Without detailed information on the distribution and kinematics of the HI gas we cannot determine which environmental process is responsible for the HI removal, but we can try to establish if it acts outside-in by looking at the color gradients of our galaxies. Indeed, Cortese et al. (2012) have recently shown that the extent of the star-forming disk and the shape of the color gradients are tightly related to the amount of HI gas. Using $g-i$ color gradients of massive galaxies extracted from the GASS parent sample, Wang et al. (2011) showed that more HI-rich systems are bluer on the outside relative to the inside compared to control samples matched in stellar mass and redshift. We use the same quantity adopted by Wang et al. (2011), but with opposite sign, and define $\Delta(g-i)$ as the difference between inner and outer $g-i$ colors (inner and outer regions are enclosed by R_{50} and 2.5 times the Kron radius, both determined from r-band photometry, respectively). Therefore $\Delta(g-i)$ is typically positive for disk galaxies (especially the bulge-dominated ones), because their outer regions are bluer than their inner regions. We plot the average $g-i$ color gradients versus stellar mass and in our two usual halo bins in Figure 13. There is tentative evidence that galaxies in the stellar mass interval of interest ($\lesssim 10^{11}$ M$_\odot$) have smaller values of $\Delta(g-i)$ when they are located in more massive halos — in other words their color gradients are *flatter*. Because their specific star formation rates are smaller (*i.e.*, their global $g-i$ colors are redder), this implies that their outer regions have become redder (as opposed to their central parts bluer), compared to those of galaxies with the same stellar mass but found in smaller halos. This is expected from the fact that most of the HI gas in a galaxy is typically found beyond R_{50}, and supports an outside-in suppression (without any strong enhancement in the center) of both gas and star formation in groups.

From the evidence presented by our data, we conclude that HI gas is removed from massive galaxies in the group environment, and that the process responsible for this quenches their star formation as well, most likely in the outer regions of the galaxy. Although we clearly observe the HI suppression only in galaxies with stellar masses less than $\sim 10^{11}$ M$_\odot$, we cannot exclude that environmental effects are at work also in more massive systems, which are already gas poor. This is because at high stellar mass the average GASS galaxy is a non-detection, hence we are not able to detect a possible HI decrease with respect to similar objects in smaller dark matter halos.

As discussed in the previous section, the difference of detection fractions at fixed NUV$-r$ color between high and low mass halos might indicate that the suppression of the gas takes place on timescales of $\sim$1 Gyr or shorter. This would be in qualitative agreement with the cosmological hydrodynamical simulations of Davé et al. (2013), which suggest that the process that removes HI from satellite galaxies acts quickly compared to the infall timescale into the halo (several Gyrs). All this points to a pre-processing of the gas (and star formation) in the group environment. Both ram pressure stripping and tidal interactions might be responsible for this quenching, but the fact that the mechanism seems to truncate the star formation outside-in might favor ram pressure. It is currently unclear if ram pressure stripping can significantly affect the interstellar medium of galaxies outside the rich cluster environment, where hot X-ray-emitting gas is not present, but there is some evidence that this might be the case (*e.g.* Scott et al. 2012; Freeland & Wilcots 2011).

Very interestingly, Fabello et al. (2012) came to a similar conclusion with a completely different approach. These authors determined the average gas content of massive galaxies by cross-correlating the GASS parent sample with ALFALFA, and stacking the HI spectra (mostly non-detections). They binned the galaxies by stellar mass and local density, estimated from the number of neighbors with $M_\star \geq 10^{9.5}$ M$_\odot$ within 1 Mpc and $\pm$500 km s^{-1}, and compared their results with predictions of semi-analytic models (Guo et al. 2011). For galaxies with $M_\star \leq 10^{10.5}$ M$_\odot$ (where they are not limited by small number statistics), the decline in average gas fraction with local density is stronger than the decline in mean global and central specific star formation rates. This ordering is not reproduced by the semi-analytic models, which do not include stripping of the cold interstellar medium, and suggests that ram pressure is able to remove atomic gas from the outer disks of galaxies *in the group environment* probed by GASS. Furthermore, Fabello et al. (2012) used mock catalogs generated from the semi-analytic models to show that galaxies with $10 < \log M_\star/\mathrm{M}_\odot < 10.5$ and local density parameter $N > 7$, for which the strong decline in HI content is seen, are found in dark matter halos with masses in the range of $10^{13} - 10^{14}$ M$_\odot$, in agreement with what we determined more directly in this work.

Although it is well known that the star formation of galaxies is affected by the environment well before reaching the highest densities typical of clusters, to our knowledge this is the first time that environmental effects have been proved to remove HI gas in groups in a statistical sense and from an observational point of view. Our data indicate that, at fixed stellar mass, the gas fraction of galaxies with stellar mass between 10^{10} and 10^{11} M$_\odot$ drops by at least 50% in dark matter halos with $M_\mathrm{h} \sim 10^{13} - 10^{14}$ M$_\odot$. The removal of gas in groups most likely drives the observed quenching of the star formation in these systems, and although not conclusive, we offered some evidence in support of a hydrodynamical process like ram pressure stripping behind this effect. This is extremely important for our understanding of the physical processes that transform galaxies from blue, star-forming to red and passively evolving, and suggests a key role for the pre-processing in groups. Indeed, hydrodynamical processes are usually considered not to be important in groups, and simulations do not include them (for instance, in the Guo et al. 2011 models, tidal and ram-pressure forces only remove hot gas from the halos of infalling satellites, and do not act on the cold gas).

Progress in this field requires not only better statistics and spatial resolution, but also sensitivity to low levels of gas content, which can be achieved only with large apertures and/or long integrations. GASS has the unique advantage of combining a stellar mass selection over a large volume (100-200 Mpc) with a low gas fraction limit, which allowed us to detect galaxies with $M_\mathrm{HI}/M_\star$ down to a few per cent. In order to reach these gas fractions, we observed our targets up to 90 minutes on-source with the largest collecting area currently available. Restricting the survey to lower redshifts would decrease the telescope time, but at the price of increasing cosmic variance. All-sky HI-blind surveys planned with the Australian Square Kilometer Array (SKA) Pathfinder (ASKAP; Johnston et al. 2007) and the upgraded Westerbork Synthesis Radio Telescope (APERTIF; Verheijen et al. 2008), will provide larger samples and much better spatial resolution. The large volumes surveyed will compensate for the modest sensitivity, which will be comparable to that of ALFALFA, definitely allowing a step further in this field. Furthermore, stacking is a promising, complementary technique to extend the results presented in this work. However, a sensitive HI survey able to detect galaxies with small gas fractions over a comparable volume to GASS and across a wide range of environments might have to wait for the full SKA.

ACKNOWLEDGMENTS

We thank the anonymous referee for useful suggestions.

BC is the recipient of an Australian Research Council Future Fellowship (FT120100660). APC acknowledges a National Natural Science Foundation of China international cooperation and exchange grant, no. 11250110509. The research leading to these results has received funding from the European Community's Seventh Framework Programme (/FP7/2007-2013/) under grant agreement No 229517.

This research has made use of the NASA/IPAC Extragalactic Database (NED) which is operated by the Jet Propulsion Laboratory, California Institute of Technology, under contract with the National Aeronautics and Space Administration.

The Arecibo Observatory is operated by SRI International under a cooperative agreement with the National Science Foundation (AST-1100968), and in alliance with Ana G. Méndez-Universidad Metropolitana, and the Universities Space Research Association.

GALEX (Galaxy Evolution Explorer) is a NASA Small Explorer, launched in April 2003. We gratefully acknowledge NASA's support for construction, operation, and science analysis for the GALEX mission, developed in cooperation with the Centre National d'Etudes Spatiales (CNES) of France and the Korean Ministry of Science and Technology.

Funding for the SDSS and SDSS-II has been provided by the Alfred P. Sloan Foundation, the Participating Institutions, the National Science Foundation, the U.S. Department of Energy, the National Aeronautics and Space Administration, the Japanese Monbukagakusho, the Max Planck Society, and the Higher Education Funding Council for England. The SDSS Web Site is http://www.sdss.org/.

The SDSS is managed by the Astrophysical Research Consortium for the Participating Institutions. The Participating Institutions are the American Museum of Natural History, Astrophysical Institute Potsdam, University of Basel, University of Cambridge, Case Western Reserve University, University of Chicago, Drexel University, Fermilab, the Institute for Advanced Study, the Japan Participation Group, Johns Hopkins University, the Joint Institute for Nuclear Astrophysics, the Kavli Institute for Particle Astrophysics and Cosmology, the Korean Scientist Group, the Chinese Academy of Sciences (LAMOST), Los Alamos National Laboratory, the Max-Planck-Institute for Astronomy (MPIA), the Max-Planck-Institute for Astrophysics (MPA), New Mexico State University, Ohio State University, University of Pittsburgh, University of Portsmouth, Princeton University, the United States Naval Observatory, and the University of Washington.

REFERENCES

Adelman-McCarthy J. K. et al., 2008, ApJS, 175, 297

Baldry I. K., Glazebrook K., Brinkmann J., Ivezić Ž., Lupton R. H., Nichol R. C., Szalay A. S., 2004, ApJ, 600, 681
Balogh M. et al., 2004, MNRAS, 348, 1355
Binggeli B., Sandage A., Tammann G. A., 1985, AJ, 90, 1681
Blanton M. R., Moustakas J., 2009, ARA&A, 47, 159
Boselli A., Boissier S., Cortese L., Gil de Paz A., Seibert M., Madore B. F., Buat V., Martin D. C., 2006, ApJ, 651, 811
Boselli A. et al., 2010, PASP, 122, 261
Boselli A., Gavazzi G., 2006, PASP, 118, 517
Bravo-Alfaro H., Cayatte V., van Gorkom J. H., Balkowski C., 2000, AJ, 119, 580
Catinella B. et al., 2012a, MNRAS, 420, 1959
Catinella B. et al., 2012b, A&A, 544, A65 (DR2)
Catinella B. et al., 2010, MNRAS, 403, 683 (DR1)
Cayatte V., van Gorkom J. H., Balkowski C., Kotanyi C., 1990, AJ, 100, 604
Chabrier G., 2003, PASP, 115, 763
Chung A., van Gorkom J. H., Kenney J. D. P., Crowl H., Vollmer B., 2009, AJ, 138, 1741
Chung A., van Gorkom J. H., Kenney J. D. P., Vollmer B., 2007, ApJL, 659, L115
Colless M. et al., 2001, MNRAS, 328, 1039
Cooper M. C. et al., 2006, MNRAS, 370, 198
Cortese L., 2012, A&A, 543, A132
Cortese L. et al., 2012, A&A, 544, A101
Cortese L., Catinella B., Boissier S., Boselli A., Heinis S., 2011, MNRAS, 415, 1797
Davé R., Finlator K., Oppenheimer B. D., 2011, MNRAS, 416, 1354
Davé R., Katz N., Oppenheimer B. D., Kollmeier J. A., Weinberg D. H., 2013, ArXiv e-prints
Dressler A., 1980, ApJ, 236, 351
Dreyer J. L. E., 1888, MmRAS, 49, 1
Dreyer J. L. E., 1895, MmRAS, 51, 185
Dreyer J. L. E., 1908, MmRAS, 59, 105
Fabello S., Catinella B., Giovanelli R., Kauffmann G., Haynes M. P., Heckman T. M., Schiminovich D., 2011a, MNRAS, 411, 993
Fabello S., Kauffmann G., Catinella B., Giovanelli R., Haynes M. P., Heckman T. M., Schiminovich D., 2011b, MNRAS, 416, 1739
Fabello S., Kauffmann G., Catinella B., Li C., Giovanelli R., Haynes M. P., 2012, MNRAS, 427, 2841
Freeland E., Wilcots E., 2011, ApJ, 738, 145
Fu J., Guo Q., Kauffmann G., Krumholz M. R., 2010, MNRAS, 409, 515
Gavazzi G., 1989, ApJ, 346, 59
Gavazzi G. et al., 2013, ArXiv e-prints
Giovanelli R., Haynes M. P., 1985, ApJ, 292, 404
Giovanelli R. et al., 2005, AJ, 130, 2598
Gómez P. L. et al., 2003, ApJ, 584, 210
Gunn J. E., Gott, III J. R., 1972, ApJ, 176, 1
Guo Q. et al., 2011, MNRAS, 413, 101
Haynes M. P., Giovanelli R., 1984, AJ, 89, 758
Haynes M. P. et al., 2011, AJ, 142, 170
Huang S., Haynes M. P., Giovanelli R., Brinchmann J., 2012, ApJ, 756, 113
Huchtmeier W. K., 1997, A&A, 325, 473
Iono D., Yun M. S., Mihos J. C., 2004, ApJ, 616, 199
Johnston S. et al., 2007, PASA, 24, 174
Kauffmann G. et al., 2003, MNRAS, 341, 54
Kauffmann G. et al., 2012, MNRAS, 422, 997
Kauffmann G., White S. D. M., Heckman T. M., Ménard B., Brinchmann J., Charlot S., Tremonti C., Brinkmann J., 2004, MNRAS, 353, 713
Kenney J. D. P., van Gorkom J. H., Vollmer B., 2004, AJ, 127, 3361
Kewley L. J., Geller M. J., Barton E. J., 2006, AJ, 131, 2004
Kilborn V. A., Forbes D. A., Barnes D. G., Koribalski B. S., Brough S., Kern K., 2009, MNRAS, 400, 1962
Lagos C. D. P., Baugh C. M., Lacey C. G., Benson A. J., Kim H.-S., Power C., 2011, MNRAS, 418, 1649
Larson R. B., Tinsley B. M., Caldwell C. N., 1980, ApJ, 237, 692
Lewis I. et al., 2002, MNRAS, 334, 673
Martin D. C. et al., 2005, ApJL, 619, L1
Moran S. M. et al., 2012, ApJ, 745, 66
Nilson P., 1973, Uppsala general catalogue of galaxies
Saintonge A., 2007, AJ, 133, 2087
Saintonge A. et al., 2011, MNRAS, 415, 32
Salim S. et al., 2007, ApJS, 173, 267
Schiminovich D. et al., 2010, MNRAS, 408, 919
Scott T. C., Cortese L., Brinks E., Bravo-Alfaro H., Auld R., Minchin R., 2012, MNRAS, 419, L19
Shen S., Mo H. J., White S. D. M., Blanton M. R., Kauffmann G., Voges W., Brinkmann J., Csabai I., 2003, MNRAS, 343, 978
Solanes J. M., Manrique A., García-Gómez C., González-Casado G., Giovanelli R., Haynes M. P., 2001, ApJ, 548, 97
Springob C. M., Haynes M. P., Giovanelli R., Kent B. R., 2005, ApJS, 160, 149 (S05)
Verdes-Montenegro L., Yun M. S., Williams B. A., Huchtmeier W. K., Del Olmo A., Perea J., 2001, A&A, 377, 812
Verheijen M. A. W., Oosterloo T. A., van Cappellen W. A., Bakker L., Ivashina M. V., van der Hulst J. M., 2008, in American Institute of Physics Conference Series, Vol. 1035, The Evolution of Galaxies Through the Neutral Hydrogen Window, Minchin R., Momjian E., eds., pp. 265–271
Vollmer B., 2009, A&A, 502, 427
Wang J. et al., 2011, MNRAS, 412, 1081
Wang J., Overzier R., Kauffmann G., von der Linden A., Kong X., 2010, MNRAS, 401, 433
Warren M. S., Abazajian K., Holz D. E., Teodoro L., 2006, ApJ, 646, 881
Weinmann S. M., van den Bosch F. C., Yang X., Mo H. J., 2006, MNRAS, 366, 2
Woo J. et al., 2013, MNRAS, 428, 3306
Wyder T. K. et al., 2007, ApJS, 173, 293
Yang X., Mo H. J., van den Bosch F. C., Pasquali A., Li C., Barden M., 2007, ApJ, 671, 153
Yang X., Mo H. J., van den Bosch F. C., Zhang Y., Han J., 2012, ApJ, 752, 41
York D. G. et al., 2000, AJ, 120, 1579
Yun M. S., Ho P. T. P., Lo K. Y., 1994, Nature, 372, 530
Zwicky F., Herzog E., Wild P., Karpowicz M., Kowal C. T., 1961, Catalogue of galaxies and of clusters of galaxies, Vol. I

APPENDIX A: DATA RELEASE

We present here SDSS postage stamp images, Arecibo HI-line spectra, and catalogs of optical, UV and HI parameters for the 250 galaxies included in this third and final data release. The content and format of the tables are identical to the DR2 ones, and we refer the reader to that paper for details. We only briefly summarize their content below. Notes on individual objects (marked with an asterisk in the last column of Tables 3 and 4) are reported in Appendix B.

SDSS and GALEX data.
Table 2 lists optical and UV quantities for the 250 GASS galaxies, ordered by increasing right ascension:
Cols. (1) and (2): GASS and SDSS identifiers.
Col. (3): UGC (Nilson 1973), NGC (Dreyer 1888) or IC (Dreyer 1895, 1908) designation, or other name, typically from the Catalog of Galaxies and Clusters of Galaxies (CGCG; Zwicky et al. 1961), or the Virgo Cluster Catalog (VCC; Binggeli, Sandage & Tammann 1985).
Col. (4): SDSS redshift, $z_{\rm SDSS}$. The typical uncertainty of SDSS redshifts for this sample is 0.0002.
Col. (5): base-10 logarithm of the stellar mass, $M_\star$, in solar units. Stellar masses are derived from SDSS photometry using the methodology described in Salim et al. (2007) (a Chabrier 2003 initial mass function is assumed). Over our required stellar mass range, these values are believed to be accurate to better than 30%.
Col. (6): radius containing 50% of the Petrosian flux in z-band, $R_{50,z}$, in arcsec.
Cols. (7) and (8): radii containing 50% and 90% of the Petrosian flux in r-band, R_{50} and R_{90} respectively, in arcsec.
Col. (9): base-10 logarithm of the stellar mass surface density, $\mu_\star$, in M$_\odot$ kpc^{-2}. This quantity is defined as $\mu_\star = M_\star/(2\pi R_{50,z}^2)$, with $R_{50,z}$ in kpc units.
Col. (10): Galactic extinction in r-band, ext$_r$, in magnitudes, from SDSS.
Col. (11): r-band model magnitude from SDSS, r, corrected for Galactic extinction.
Col. (12): minor-to-major axial ratio from the exponential fit in r-band, $(b/a)_r$, from SDSS.
Col. (13): inclination to the line-of-sight, in degrees (see Catinella et al. 2012b for details).
Col. (14): NUV$-r$ observed color from our reprocessed photometry, corrected for Galactic extinction.
Col. (15): exposure time of GALEX NUV image, T$_{NUV}$, in seconds.
Col. (16): maximum on-source integration time, $T_{\rm max}$, required to reach the limiting HI mass fraction, in minutes (see § 2). Given the HI mass limit and redshift of each galaxy, $T_{\rm max}$ is computed assuming a 5σ signal with 300 km s^{-1} velocity width and the instrumental parameters typical of our observations (*i.e.*, gain ∼10 K Jy^{-1} and system temperature ∼28 K at 1370 MHz).

HI source catalogs.
This data release includes 147 detections and 103 non-detections, for which we provide upper limits below.

The measured HI parameters for the detected galaxies are listed in Table 3, ordered by increasing right ascension:
Cols. (1) and (2): GASS and SDSS identifiers.
Col. (3): SDSS redshift, $z_{\rm SDSS}$.
Col. (4): on-source integration time of the Arecibo observation, $T_{\rm on}$, in minutes. This number refers to *on scans* that were actually combined, and does not account for possible losses due to RFI excision (usually negligible).
Col. (5): velocity resolution of the final, smoothed spectrum in km s^{-1}.
Col. (6): redshift, z, measured from the HI spectrum. The error on the corresponding heliocentric velocity, cz, is half the error on the width, tabulated in the following column.
Col. (7): observed velocity width of the source line profile in km s^{-1}, W_{50}, measured at the 50% level of each peak. The error on the width is the sum in quadrature of the statistical and systematic uncertainties in km s^{-1}. Statistical errors depend primarily on the signal-to-noise of the HI spectrum, and are obtained from the rms noise of the linear fits to the edges of the HI profile. Systematic errors depend on the subjective choice of the HI signal boundaries (see DR1 paper), and are negligible for most of the galaxies in our sample (see also Appendix B).
Col. (8): velocity width corrected for instrumental broadening and cosmological redshift only, ${W_{50}}^c$, in km s^{-1} (see Catinella et al. 2012b for details). No inclination or turbulent motion corrections are applied.
Col. (9): observed, integrated HI-line flux density in Jy km s^{-1}, $F \equiv \int S\ dv$, measured on the smoothed and baseline-subtracted spectrum. The reported uncertainty is the sum in quadrature of the statistical and systematic errors (see col. 7). The statistical errors are calculated according to equation 2 of S05 (which includes the contribution from uncertainties in the baseline fit).
Col. (10): rms noise of the observation in mJy, measured on the signal- and RFI-free portion of the smoothed spectrum.
Col. (11): signal-to-noise ratio of the HI spectrum, S/N, estimated following Saintonge (2007) and adapted to the velocity resolution of the spectrum. This is the definition of S/N adopted by ALFALFA, which accounts for the fact that for the same peak flux a broader spectrum has more signal.
Col. (12): base-10 logarithm of the HI mass, $M_{\rm HI}$, in solar units (see Catinella et al. 2012b for details).
Col. (13): base-10 logarithm of the HI mass fraction, $M_{\rm HI}/M_\star$.
Col. (14): quality flag, Q (1=good, 2=marginal, 3=marginal and confused, 5=confused). An asterisk indicates the presence of a note for the source in Appendix 7. Code 1 indicates reliable detections, with a S/N ratio of order of 6.5 or higher. Marginal detections have lower S/N, thus more uncertain HI parameters, but are still secure detections, with HI redshift consistent with the SDSS one. We flag galaxies as "confused" when most of the HI emission is believed to originate from another source within the Arecibo beam. For some of the galaxies, the presence of small companions within the beam might contaminate (but is unlikely to dominate) the HI signal – this is just noted in Appendix B.

Table 4 gives the derived HI upper limits for the non-detections. Columns (1-4) and (5) are the same as columns (1-4) and (10) in Table 3, respectively. Column (6) lists the upper limit on the HI mass in solar units, Log $M_{{\rm HI},lim}$, computed assuming a 5 σ signal with 300 km s^{-1} velocity width, if the spectrum was smoothed to 150 km s^{-1}. Column (7) gives the corresponding upper limit on the gas fraction, Log $M_{{\rm HI},lim}/M_\star$. An asterisk in

Column (8) indicates the presence of a note for the galaxy in Appendix B.

SDSS postage stamps and HI spectra.
SDSS images and HI spectra of the galaxies are presented here, organized as follows: HI detections with quality flag 1 in Table 3 (Figure 14), marginal and/or confused detections with quality flag 2-5 (Figure 15) and non-detections (Figure 16). The objects in each of these figures are ordered by increasing GASS number (indicated on the top right corner of each spectrum). The SDSS images show a 1 arcmin square field, *i.e.* only the central part of the region sampled by the Arecibo beam (the half power full width of the beam is $\sim 3.5'$ at the frequencies of our observations). Therefore, companions that might be detected in our spectra typically are not visible in the postage stamps, but they are noted in Appendix B. The HI spectra are always displayed over a 3000 km s^{-1} velocity interval, which includes the full 12.5 MHz bandwidth adopted for our observations. The HI-line profiles are calibrated, smoothed (to a velocity resolution between 5 and 21 km s^{-1} for the detections, as listed in Table 3, or to $\sim$15 km s^{-1} for the non-detections), and baseline-subtracted. A red, dotted line indicates the heliocentric velocity corresponding to the optical redshift from SDSS. In Figures 14-15, the shaded area and two vertical dashes show the part of the profile that was integrated to measure the HI flux and the peaks used for width measurement, respectively.

APPENDIX B: NOTES ON INDIVIDUAL OBJECTS

We list here notes for galaxies marked with an asterisk in the last column of Tables 3 and 4. The galaxies are ordered by increasing GASS number. In what follows, AA2 is the abbreviation for ALFALFA detection code 2.

Detections (Table 3)

3666 – small blue companion $\sim$1 arcmin SW, SDSS J011759.89+153148.0 ($z = 0.038248$), some contamination certain. There is also a blue galaxy $\sim$3 arcmin N, no SDSS redshift.
3851 – offset from SDSS redshift, confused. This is a galaxy group, including a blue disk $\sim$2 arcmin W (SDSS J013844.52+150331.1, $z = 0.028769$, 8625 km s^{-1}) and two early-type galaxies $\sim$1.5 arcmin SW (SDSS J013848.58+150141.2, $z = 0.028044$) and $\sim$2 arcmin SE (SDSS J013854.76+150117.7, $z = 0.027916$).
3917 – marginal detection. Notice companion spiral galaxy $\sim$4 arcmin NW, SDSS J015742.52+132318.8 ($z = 0.044431$).
3936 – small blue disk $\sim$2 arcmin N has no SDSS redshift.
3960 – spectacular pair of interacting galaxies in the foreground ($z = 0.012$). AA2.
3966 – blend/confused with blue companion $\sim$2 arcmin W, SDSS J020447.70+140147.8 ($z = 0.030942$).
3987 – detected blue companion $\sim$2 arcmin W, SDSS J021327.81+132806.1 ($z = 0.041604$, 12473 km s^{-1}), confusion certain.
4056 – high frequency edge uncertain, systematic error. Small blue cloud at the N edge of the galaxy, perhaps responsible for the peak at 11750 km s^{-1}?
4111 – AA2.
4136 – low frequency edge uncertain, systematic error. Blue companion $\sim$40 arcsec SE, SDSS J015706.42+130926.9 ($z = 0.032673$, 9795 km s^{-1}), confused. The blue galaxy $\sim$40 arcsec NE, SDSS J015706.42+131039.4, has $z = 0.044781$.
4165 – confused: blue companions $\sim$1.5 arcmin W (SDSS J015040.40+134106.1, $z = 0.044814$, 13435 km s^{-1}) and 3 arcmin S (SDSS J015047.04+133824.1, $z = 0.04437$, 13302 km s^{-1}); two other blue galaxies within 3 arcmin NE are in the background (SDSS J015057.74+134249.2, $z = 0.050$ and SDSS J015052.62+134318.6, $z = 0.057$).
5701 – two blue galaxies within 2.5 arcmin are in the background ($z = 0.08$); small early-type galaxy 40 arcsec N has no SDSS redshift, but is unlikely to contaminate the signal.
6015 – RFI spike at 1375 MHz ($\sim$9900 km s^{-1}).
6679 – RFI feature at 1360 MHz (13300 km s^{-1}). Three blue galaxies $\sim$3 arcmin W: the large edge-on disk (SDSS J130158.47+030602.6, $z = 0.023386$ from NED) and its small companion to the N are in the foreground, and SDSS J130200.53+030550.1 is in the background ($z = 0.079602$).
7121 – near bright star.
7405 – asymmetric profile, uncertain width; several small galaxies within 2 arcmin, the only two with redshifts are in the background ($z = 0.056$ and $z = 0.13$).
7813 – blue companion $\sim$1.5 arcmin E, SDSS J151249.84+012827.7 ($z = 0.0304$, 9114 km s^{-1}), is separated enough in velocity not to cause any confusion (there is a small peak at the right velocity, but it is present in one polarization only). Also, blue companion 3.6 arcmin NW, SDSS J151233.08+013017.3 ($z = 0.029178$).
8096 – low frequency edge uncertain, systematic error. Small blue companion $\sim$1.5 arcmin SW, SDSS J085249.56+030823.9 ($z = 0.034776$), some contamination certain.
8634 – possibly confused with blue galaxy $\sim$2 arcmin N, SDSS J101322.37+050312.7, no optical redshift (photometric redshift $z = 0.042$).
8945 – blue companion $\sim$3 arcmin W, SDSS J105303.39+042036.5 ($z = 0.041924$, 12568 km s^{-1}), some contamination likely; the blue galaxy $\sim$1 arcmin NW has $z = 0.066$.
9615 – RFI spike at 1375 MHz ($\sim$9900 km s^{-1}), 2 channels replaced by interpolation. No companions within 3 arcmin, galaxy $\sim$2.5 arcmin SW is in the background (SDSS J142955.29+032157.1, $z = 0.168$).
9942 – stronger in polarization A. Blend/confused with edge-on disk 0.4 arcmin NE, SDSS J144326.39+042308.2, $cz = 7879$ km s^{-1}from NED. Blue galaxy $\sim$2.5 arcmin NE, SDSS J144332.81+042423.1, has $z = 0.071$.
10005 – blue disk $\sim$3 arcmin SW, SDSS J145259.66+033013.2, is in the background ($z = 0.045$).
10032 – three galaxies $\sim$1 arcmin N, 2 arcmin E and 2.5 arcmin SE are in the background ($z = 0.094$, 0.209 and 0.094, respectively).
11086 – 2.7 Jy continuum source at 5 arcmin, standing waves.
11092 – galaxy pair, the companion is a blue spiral $\sim$15 arcsec SE, SDSS J231340.49+140115.5 ($z = 0.040436$, 12122 km s^{-1}). Notice another two disk galaxies at the same redshift, $\sim$2.5 arcmin SW (SDSS J231334.71+135912.4, $z = 0.039767$) and $\sim$3 arcmin

NW (SDSS J231330.39+140349.7, $z = 0.039527$).
11193 – uncertain profile; early-type companion ∼1.5 arcmin E, SDSS J231328.01+141611.3 ($z = 0.038994$, 11690 km s^{-1}); another companion ∼4 arcmin NE, SDSS J231331.44+141938.7 ($z = 0.039231$, 11761 km s^{-1}), significant contamination unlikely. Small galaxy 40 arcsec W has $z = 0.150$. Better in polarization B.
11291 – companion of GASS 11292, ∼2.5 arcmin SW; strong contamination is unlikely, see note for GASS 11292.
11292 – most of the signal comes from GASS 11291 ∼2.5 arcmin NE, as can be seen by comparing the two profiles.
11312 – galaxy triplet, HI signal is most likely a blend. The two companions are disk galaxies 1.9 arcmin NE (SDSS J231229.22+135632.1, $z = 0.034137$) and 2.3 arcmin N (SDSS J231224.51+135704.5, $z = 0.034135$).
11347 – most likely confused/blend with large spiral ∼2 arcmin W, SDSS J231639.26+153516.2 ($z = 0.038807$ from NED).
11434 – small companion ∼2.5 arcmin S, SDSS J232328.01+140530.2 ($z = 0.041497$), some contamination possible.
11435 – small companions ∼2 arcmin NW (SDSS J232314.91+141817.8, $z = 0.043379$) and ∼2.5 arcmin S (SDSS J232318.65+141446.6, $z = 0.044175$), some contamination possible. Large spiral galaxy ∼3 arcmin NE is in the foreground ($z = 0.026$).
11509 – high frequency edge uncertain, systematic error. Detected (part of) blue companion ∼1.7 arcmin NW, SDSS J232403.09+145137.7 ($z = 0.042698$, 12801 km s^{-1}).
11573 – stronger in polarization B. Early-type companion 2 arcmin E, SDSS J233019.67+132657.3 ($z = 0.039838$); the early-type galaxy ∼1 arcmin N, SDSS J233013.51+132801.6, has $z = 0.041588$ (12468 km s^{-1}).
11669 – edge-on galaxy ∼1 arcmin SE, SDSS J232715.24+152752.4 ($z = 0.046110$ from NED), some contamination possible (although the profile is consistent with the fact that the target is almost face-on). AA2.
12062 – reddish companion ∼2 arcmin NE, same redshift ($z = 0.036556$), and two small galaxies ∼30 arcsec S, no redshifts; small contamination possible.
13159 – no obvious companion within the beam, however notice two small, blue smudges ∼1 and 1.5 arcmin E, without optical redshifts.
13618 – blend with companion 1 arcmin S, SDSS J135621.74+043606.0 ($z = 0.03382$, 10139 km s^{-1}).
13674 – AA2.
14247 – small companion ∼2 arcmin SW, SDSS J080523.82+355454.5 ($z = 0.033211$), some contamination possible.
15257 – uncertain profile; most likely confused/blend with blue galaxy ∼45 arcsec W, SDSS J104802.72+060103.7, without optical redshift.
17622 – disk galaxy ∼1.5 arcmin SW is in the background ($z = 0.061$). AA2.
17673 – confused/blend with blue companion ∼3 arcmin E, SDSS J110009.92+102214.1 ($z = 0.036759$, 11020 km s^{-1}); small galaxy ∼1 arcmin SE has $z = 0.092$.
18084 – detected blue companion ∼2 arcmin W, SDSS J115104.26+085225.0 ($z = 0.036558$, 10960 km s^{-1}).
18131 – two blue galaxies in the background, one ∼1 arcmin N (SDSS J120446.89+092617.6, $z = 0.069$) and one 3 arcmin S (SDSS J120446.35+092222.2, $z = 0.041$). Notice however blue, low surface brightness (LSB) galaxy 1 arcmin S, SDSS J120445.64+092426.7, without optical redshift. Confused?
18138 – early-type companion ∼3 arcmin W, SDSS J120227.14+085548.2 ($z = 0.034643$), significant contamination unlikely. Stronger in polarization B.
18225 – blue disk ∼1 arcmin W, SDSS J120507.73+103352.6, without optical redshift. Small blue galaxy ∼2 arcmin E, SDSS J120517.65+103320.5, has $z = 0.023$. Notice large early-type companion ∼3.5 arcmin N, SDSS J120514.04+103647.6 ($z = 0.033449$). Three other galaxies ∼3 arcmin away in the W quadrant are in the background ($z = 0.09$).
19672 – galaxy pair.
19989 – several small galaxies around without optical redshifts; galaxy ∼2.5 arcmin SW, SDSS J085419.08+081057.2, has $z = 0.096$.
20041 – large, blue companion 3.3 arcmin NE, SDSS J091437.31+080702.0 ($z = 0.031015$ from NED). The companion is detected by ALFALFA (AGC 191126) with W_{50}= 402 km s^{-1}and flux of 3.09 Jy km s^{-1}. Confused?
20376 – polarization mismatch (clear, overlapping signal in both polarizations, but offset by 1 MHz). The signal is most likely confused/blend with that of a blue spiral ∼2.5 arcmin NW, SDSS J095407.95+103625.6 (also AGC 193987, detected by ALFALFA; $z = 0.040392$, 12109 km s^{-1}). Notice also GASS 20445 ∼3 arcmin E ($z = 0.039708$, 11904 km s^{-1}; non-detection in this release).
23070 – spiral galaxy 3 arcmin W has $z = 0.109$.
23496 – RFI spikes near 1352.5 MHz (∼15,000 km s^{-1}). Small companion ∼1 arcmin E, SDSS J105725.50+120638.9 ($z = 0.047348$), and galaxy ∼30 arcsec NW without SDSS redshift; some contamination possible. AA2.
23703 – small blue galaxy ∼2 arcmin S, no optical redshift.
23739 – blue companion ∼3 arcmin SW, SDSS J113655.36+115053.9 ($z = 0.034412$, 10316 km s^{-1}), separated enough in velocity from the target.
23781 – confused/blend with large blue spiral ∼2 arcmin NW, SDSS J114206.64+113216.0 ($z = 0.042924$, 12868 km s^{-1}).
23789 – most likely confused/blend with blue companion ∼2.7 arcmin E, SDSS J114154.89+123030.7 ($z = 0.034531$, 10352 km s^{-1}).
23815 – small galaxy ∼20 arcsec SW has no redshift; blue galaxy ∼2 arcmin E is in the background ($z = 0.052$).
24496 – small blue companion ∼2 arcmin N, SDSS J111809.86+074845.7 ($z = 0.041832$), some contamination certain.
25215 – several galaxies to the S, all in the background.
25721 – small blue galaxy ∼1.7 arcmin S, SDSS J155507.68+092848.6, no optical redshift.
26406 – small galaxy ∼2.5 arcmin W has $z = 0.044$; smudge ∼1 arcmin E has no SDSS redshift.
26407 – RFI spike at 1352.6 MHz (15,000 km s^{-1}). Edge-on galaxy ∼2 arcmin NE is in the background ($z = 0.086$).
26586 – notice two blue, edge-on disks ∼4 arcmin from the target and with similar redshifts: SDSS J103624.87+130827.0 (4 arcmin SE, $z = 0.034084$) and SDSS J103619.24+131317.5 (3.5 arcmin NE, $z = 0.033366$).
28062 – most likely blend with small companion ∼1.5 arcmin E, SDSS J122807.37+081057.3 ($z = 0.037407$, 11214 km s^{-1}), which is exactly centered on the highest peak.

Also notice companion galaxy ∼3.5 arcmin NE.
28317 – companion ∼2 arcmin NW, SDSS J154403.74+274152.5 (z = 0.031411), but there is no hint of detection on the side away from GASS 28317, so contamination is unlikely. Notice however disk galaxy next to it, without optical redshift.
28703 – AA2.
31095 – AA2.
32308 – AA2.
33214 – high frequency edge uncertain, systematic error. The disk galaxy ∼2.5 arcmin S has $z = 0.050$.
33737 – disturbed, no companions within the beam, large offset from SDSS redshift ($z = 0.026869$, 8055 km s^{-1}).
38198 – several galaxies within 3 arcmin in the background ($z = 0.097$).
38458 – uncertain profile; blend: connected to large companion ∼40 arcsec E, SDSS J140606.72+123013.6 (also GASS 25575, not detected in DR1; z = 0.037966, 11382 km s^{-1}); notice also small companion ∼1.5 arcmin W, SDSS J140557.71+123016.6 ($z = 0.039257$, 11769 km s^{-1}).
39082 – blue LSB galaxy ∼1 arcmin SE, no optical redshift (photo-$z = 0.037$), possible contamination. AA2.
40495 – low frequency edge uncertain, systematic error; stronger in polarization A.
40502 – 163 mJy continuum source at 1 arcmin, standing waves.
41718 – detected blue companion in board 3, ∼1365 MHz (∼12150 km s^{-1}), most likely the very blue galaxy ∼1 arcmin NW, SDSS J144334.78+083432.3 (no optical redshift); galaxy ∼2.5 arcmin W, SDSS J144328.85+083248.9, has $z = 0.033037$ (9904 km s^{-1}).
41863 – interacting pair of blue galaxies: the companion is ∼40 arcsec E, SDSS J151031.62+072500.2 (cz = 9597 km s^{-1}from NED).
41869 – detected blue companion, SDSS J150921.31+070631.4, ∼2 arcmin N (z = 0.037367, 1369.24 MHz, 11200 km s^{-1}); galaxy ∼1 arcmin NE is in the background ($z = 0.078$).
42191 – profile edges uncertain, systematic error.
42233 – several galaxies within 3 arcmin in the background ($z > 0.08$).
44856 – tiny blue galaxy ∼1.5 arcmin S, SDSS J135409.08+243200.3, unknown redshift.
48356 – high frequency edge uncertain, systematic error. Interacting with SDSS J111113.00+284242.7, ∼1 arcmin N (z = 0.029366, 8804 km s^{-1}); several other galaxies with similar redshift within 3 arcmin.
48518 – low frequency edge uncertain, systematic error; uncertain profile. Blend with large spiral 2 arcmin S, SDSS J111750.61+263732.8 (z = 0.027048, 8109 km s^{-1}); there is also a small companion ∼1 arcmin N, SDSS J111751.46+264035.3 ($z = 0.026349$, 7899 km s^{-1}).
48521 – small blue galaxy ∼30 arcsec E, SDSS J111740.84+263502.1, unknown redshift, possible confusion. AA2.
48604 – small blue companion ∼1.5' N, SDSS J112746.74+265909.7 (z = 0.033782, 10129 km s^{-1}), some contamination certain. Several smaller galaxies within ∼2 arcmin, either in the background or without SDSS redshift. AA2.
48994 – two small blue companions ∼2.5 arcmin NE, SDSS J114225.77+301549.5 and SDSS J114227.14+301552.6 (both have $z = 0.033$), likely adding very little to the signal (given their size and distance to the target).
49386 – small spiral ∼2 arcmin SW is in the background ($z = 0.080$).
49727 – low frequency edge uncertain, systematic error. Galaxy pair, separation 4 arcsec (from NED); HI signal also blended with that of UGC 7064 (∼1 arcmin S, z = 0.024916, 1385.88 MHz, face-on blue galaxy, which is responsible for the low velocity peak) and likely with that of SDSS J120445.26+310927.8 (blue galaxy 2 arcmin S, z = 0.026637, 1383.55 MHz).
50404 – small companion ∼2 arcmin SW, SDSS J123400.02+280641.8 (z = 0.040307), some contamination possible. Spiral ∼3 arcmin NE is in the background ($z = 0.084$).
50406 – low frequency edge uncertain, systematic error.
51150 – small companion ∼1 arcmin S, SDSS J132301.23+270558.8 (z = 0.034507); notice also blue companion 3.7 arcmin SE, SDSS J132309.49+270359.2 ($z = 0.034215$); significant contamination unlikely.
51161 – AA2.
51334 – small companion ∼1.5 arcmin N, SDSS J075331.69+140237.3 (z = 0.029093), some contamination possible. AA2.
51580 – red companion ∼2 arcmin SW, SDSS J080359.21+150343.1 (z = 0.039), significant contamination unlikely. Several small galaxies nearby without SDSS redshift.
51899 – blend with two companions, a blue edge-on disk 2 arcmin S (SDSS J083131.00+192042.6, z = 0.039271) and a large galaxy ∼2.5 arcmin E (SDSS J083140.72+192307.8, z = 0.038759); there is also a small bluish galaxy ∼15 arcsec NE without optical redshift.
52045 – disturbed (tidal tail or companion to the S).
52297 – companion ∼2 arcmin NE, SDSS J085724.03+204237.8 ($z = 0.032874$), plus several galaxies nearby without SDSS redshifts; some contamination likely.
55541 – small blue galaxy ∼1 arcmin SW has z = 0.048, no comtamination problems.
55745 – stronger in polarization B.
56509 – 111 mJy continuum source at 2 arcmin, standing waves. Small blue companion ∼2 arcmin N, SDSS J085047.04+115102.8 (z = 0.029322), some contamination likely.
56662 – a few small galaxies within 3 arcmin, all in the background.

Non-detections (Table 4)

3157 – small face-on, spiral companion ∼2 arcmin E, SDSS J003042.29+145610.4 ($z = 0.038491$, 11539 km s^{-1}).
3258 – perhaps hint of galaxy signal; blue galaxy ∼2.5 arcmin SW has $z = 0.076$.
3972 – edge-on companion ∼3 arcmin SW, SDSS J020530.66+143652.7 (z = 0.042305, 12683 km s^{-1}); hint of signal centered at 12800 km s^{-1} is in polarization B only.
3980 – detected LSB companion ∼1.5 arcmin S, SDSS J021424.66+121836.7 (z = 0.040399, 12111 km s^{-1}, in much better agreement with SDSS redshift). Stronger in polarization A.
4014 – small companion ∼3.5 arcmin NE, SDSS

J020732.08+130338.3 ($z = 0.048163$, 14439 km s^{-1}).
4130 – blue companion ∼3.5 arcmin W, SDSS J015706.42+131039.4 ($z = 0.044781$); several other galaxies within 3 arcmin, with redshifts significantly different from GASS 4130 or unknown.
5204 – blue companion ∼3 arcmin SE, SDSS J102800.60+023414.1 ($z = 0.028467$, 8534 km s^{-1}) also not detected.
7310 – the two disk galaxies 3 arcmin S and ∼3.5 arcmin NE have $z > 0.05$.
8953 – blue companion ∼3 arcmin NE, SDSS J105251.60+041109.3 ($z = 0.043311$, 12984 km s^{-1}), marginally detected?
8971 – two companions: edge-on disk ∼1.5 arcmin NW, SDSS J104832.28+044838.1 ($z = 0.033723$, 10110 km s^{-1}) and face-on, blue spiral ∼3 arcmin NW, SDSS J104827.34+044931.7 ($z = 0.034128$, 10231 km s^{-1}), also not detected. The small galaxy ∼3 arcmin SE, SDSS J104847.35+044605.5, has $z = 0.026$.
9702 – small galaxy ∼1 arcmin W, SDSS J144039.22+032250.3 ($z = 0.030114$, 9028 km s^{-1}); several other galaxies within ∼3 arcmin with redshifts $z < 0.028$ or $z > 0.089$.
10211 – blue galaxy ∼1.5 arcmin S has $z = 0.093$.
11080 – double nucleus; detected blue companion ∼2 arcmin N in board 3, SDSS J225609.41+130551.4 ($z = 0.037436$, 1369.15 MHz).
11249 – companion of GASS 11257, ∼2 arcmin E (SDSS J230806.95+152520.2, $z = 0.036716$, see next note); large early-type galaxy ∼0.5 arcmin N without optical redshift.
11257 – companion of GASS 11249, ∼2 arcmin W (SDSS J230757.92+152455.2, $z = 0.03623$, see previous note); large early-type galaxy ∼2.5 arcmin W without optical redshift.
11284 – perhaps hint of galaxy signal.
11395 – small companion ∼2 arcmin S, SDSS J232336.22+133706.0 ($z = 0.042373$, 12703 km s^{-1}).
11410 – detected companion without redshift? perhaps the small LSB galaxy ∼0.5 arcmin NW, SDSS J232220.71+135957.4; the signal is significantly stronger in polarization A, although no RFI is visible at that frequency.
11544 – AA2. Marginally detected disk galaxy ∼2 arcmin NW, SDSS J232531.72+152211.6 ($z = 0.040311$, 12085 km s^{-1}).
11567 – two companions, a large spiral 2 arcmin W, SDSS J233011.60+132656.2 ($z = 0.038729$, 11611 km s^{-1}) and a small one ∼2 arcmin SE, SDSS J233024.64+132531.6 ($z = 0.039084$, 11717 km s^{-1}); notice also the early-type galaxy ∼2 arcmin NW, SDSS J233013.51+132801.6 ($z = 0.041588$, 12468 km s^{-1}).
11568 – large early-type galaxy ∼2 arcmin SE, SDSS J233019.67+132657.3 ($z = 0.039838$) and a spiral ∼1.5 arcmin S, SDSS J233011.60+132656.2 ($z = 0.038729$).
11585 – marginally detected blue companion ∼3 arcmin N, SDSS J232519.80+142419.5 ($z = 0.042036$, 12602 km s^{-1}).
11636 – two blue companions: SDSS J232336.90+151532.2 ∼2 arcmin NE ($z = 0.043298$, 12980 km s^{-1}) and GASS 11494 ∼2.5 arcmin S (SDSS J232335.34+151148.7, $z = 0.042709$, 12804 km s^{-1}, DR2 detection). The HI signal is most likely a blend of the two.
11791 – marginally detected blue companion ∼1.5 arcmin SE, SDSS J235205.28+144403.6 ($z = 0.0450$, 13491 km s^{-1}); another two galaxies with similar redshifts ∼2 arcmin N (SDSS J235158.07+144711.1, $z = 0.046598$, 13970 km s^{-1}) and ∼3.5 arcmin SW (SDSS J235148.64+144241.3, $z = 0.046466$, 13930 km s^{-1}).
11892 – three galaxies within 3 arcmin with $z > 0.09$, and two edge-on disks ∼3 arcmin S without optical redshifts.
11903 – two small galaxies within 0.5 arcmin without optical redshift.
12452 – companion ∼2 arcmin S, SDSS J112003.92+040830.2 ($z = 0.049371$, 14801 km s^{-1}); three other galaxies within 2.5 arcmin with $z = 0.15$.
12967 – companion of GASS 12970, ∼2 arcmin S (SDSS J123553.79+054539.8, $z = 0.041788$, DR2 non-detection). Small galaxy ∼2.5 arcmin S, SDSS J123556.38+054459.2 ($z = 0.041189$, 12348 km s^{-1}) also not detected. $T_{\rm max}$ not reached; perhaps hint of galaxy signal, but stronger in polarization A.
14017 – small blue cloud to the NW edge of the galaxy; galaxy pair ∼4 arcmin SW in the foreground ($z = 0.016$).
14260 – small blue galaxy ∼2 arcmin S has $z = 0.145$.
16756 – edge-on disk ∼40 arcsec SE and small blue galaxy ∼1 arcmin SW, both without optical redshift.
18004 – barred spiral galaxy ∼40 arcsec SE and small galaxy ∼40 arcsec W, both without optical redshifts; small early-type companion ∼2.5 arcmin E, SDSS J115145.97+084531.2 ($z = 0.035926$) also not detected.
18220 – perhaps hint of galaxy signal. Early-type companion ∼2.5 arcmin W, SDSS J120527.47+104204.4 ($z = 0.035443$, 10626 km s^{-1}); the blue galaxy ∼2.5 arcmin NW, SDSS J120530.37+104313.8, has $z = 0.063$.
19274 – AA2. Small companion ∼3 arcmin N, SDSS J081622.22+260241.1 ($z = 0.045113$) also not detected.
20149 – hint of galaxy signal.
20165 – detected companion (GASS 20133, DR1 detection) ∼1 arcmin E (SDSS J093236.58+095025.9, $z = 0.048884$, 14655 km s^{-1}).
20445 – companion of GASS 20376, ∼3 arcmin W (SDSS J095416.83+103457.5, $z = 0.039938$, see detections in this release).
23029 – three companions: SDSS J102714.26+110340.0, ∼2 arcmin W ($z = 0.032969$), SDSS J102710.59+110116.2, ∼2.5 arcmin S ($z = 0.032657$) and SDSS J102707.78+110038.5, ∼3 arcmin S ($z = 0.032367$).
23102 – perhaps hint of galaxy signal.
23203 – detected companion, probably the LSB galaxy ∼3 arcmin E, SDSS J103602.58+121118.3 ($z = 0.038124$, 11429 km s^{-1}), but notice also blue smudge ∼1.5 arcmin NE without optical redshift.
23457 – early-type galaxy ∼1 arcmin NE without optical redshift.
23531 – RFI at 1370 MHz (∼11000 km s^{-1}) visible in final spectrum.
25057 – companion of GASS 25115 (SDSS J152112.78+303928.5, ∼1.8 arcmin SE, see next note), also not detected; several other galaxies within 3 arcmin in the background ($z > 0.07$).
25115 – companion of GASS 25057 (SDSS J152106.26+304036.9, see previous note), also not detected; several other galaxies within 3 arcmin in the background ($z > 0.07$).
25213 – detected companion, most likely SDSS J131221.39+114022.8, 3 arcmin S ($z = 0.030132$, 9033

km s^{-1}). Two other galaxies within the beam with sligthly higher redshift: SDSS J131229.71+114432.7, $\sim$2 arcmin NE ($z = 0.030916$, 9268 km s^{-1}) and GASS 25214 (SDSS J131232.81+114344.2, $z = 0.031105$, 9325 km s^{-1}), 2.5 arcmin E, which was not detected in DR1.
25682 – three galaxies within $\sim$3.5 arcmin at slightly higher redshift ($z = 0.042$), plus others without optical redshifts.
26017 – large early-type companion $\sim$2.5 arcmin SW, SDSS J095634.77+110947.4 ($z = 0.041272$, 12373 km s^{-1}), and small disk galaxy $\sim$2 arcmin W, SDSS J095633.88+111058.2 ($z = 0.04049$, 12139 km s^{-1}).
26503 – large early-type companion 3 arcmin SE, SDSS J102323.75+125006.1 ($z = 0.032486$, 9739 km s^{-1}); other galaxies within 3 arcmin are in the background or have no redshift.
28030 – perhaps hint of galaxy signal, but present in polarization B only.
28327 – next to bright star; two companion spirals $\sim$3.5 arcmin E (SDSS J154145.55+275917.8, $z = 0.032026$) and 4 arcmin N (SDSS J154135.57+280258.6, $z = 0.031891$, AA2).
28348 – companion $\sim$2 arcmin SE, SDSS J154100.75+281922.9 ($z = 0.032234$, 9664 km s^{-1}); the small blue galaxy $\sim$2 arcmin E has $z = 0.066$.
30746 – galaxy $\sim$1 arcmin NW has $z = 0.079$.
31478 – hint of galaxy signal; two galaxies $\sim$2 arcmin W and $\sim$2 arcmin NW have $z = 0.063$.
33469 – small blue galaxy $\sim$2.5 arcmin E is in the foreground ($z = 0.005$).
33777 – detected blue companion $\sim$2 arcmin W, SDSS J100240.68+323749.4 ($z = 0.045315$, 13585 km s^{-1}); several other galaxies within 3 arcmin with redshifts between 0.048 and 0.052.
35475 – face-on spiral galaxy $\sim$3 arcmin SE, SDSS J125941.30+283025.9 ($z = 0.027566$, 8264 km s^{-1}), also not detected.
35497 – hint of galaxy signal. Four galaxies within 3.5 arcmin are in the background ($z > 0.06$).
39407 – blue companion $\sim$2 arcmin SE, SDSS J152248.12+083148.0 ($z = 0.036607$, 10975 km s^{-1}), and three galaxies $\sim$2.5 arcmin away with $z = 0.034 - 0.035$ (SDSS J152236.57+083447.5, SDSS J152249.21+083337.9, SDSS J152244.22+083013.3).
41723 – blue companion $\sim$3.5 arcmin NE, SDSS J144610.59+085807.7 ($z = 0.029595$, 8872 km s^{-1}); also notice two blue disks $\sim$2.5 arcmin N without optical redshifts.
44021 – small blue galaxy $\sim$70 arcsec NE, SDSS J134235.17+301547.2, has $z = 0.124$; very blue galaxy $\sim$2 arcmin SW, SDSS J134226.53+301311.0, has no optical redshift.
45940 – small bluish cloud to the N of the galaxy. Large red companion $\sim$2.5 arcmin NE, SDSS J142758.18+263016.2 ($z = 0.032298$) and two galaxies $\sim$3 arcmin SE, SDSS J142759.07+262754.1 ($z = 0.031056$) and SDSS J142759.98+262805.9 (no optical redshift).
48160 – feature at $\sim$13250 km s^{-1}is present in both polarizations; detected perhaps the small blue galaxy $\sim$1 arcmin S (SDSS J111203.29+274951.2) without optical redshift?
48205 – disk galaxy 2 arcmin N is in the foreground ($z = 0.037$); small galaxies within 1.5 arcmin without optical redshifts.
48544 – RFI spike at 1350 MHz ($\sim$15600 km s^{-1}) visible in final spectrum. Small blue companion $\sim$3 arcmin E, SDSS J112053.20+271816.7 ($z = 0.047646$, 14284 km s^{-1}).
50866 – small disk galaxy $\sim$2 arcmin SE, SDSS J125614.26+274856.0 ($z = 0.022243$, 6668 km s^{-1}); a few other small galaxies within 3 arcmin in the background ($z > 0.08$).
51462 – small, blue companion $\sim$2 arcmin NW, SDSS J075555.63+141317.0 ($z = 0.03625$, 10867 km s^{-1}) also not detected.
53269 – smaller galaxy almost superimposed is in the background (SDSS J093115.52+263255.8, $z = 0.058$).
54240 – two edge-on galaxies nearby, SDSS J102254.55+243639.4 ($\sim$20 arcsec NE, $z = 0.046341$, 13893 km s^{-1}) and SDSS J102248.59+243622.3 ($\sim$1 arcmin W, no optical redshift).
54577 – companion $\sim$2.5 arcmin W, SDSS J103007.19+273436.7 ($z = 0.047206$).
56320 – detected companion, large spiral $\sim$1 arcmin N, SDSS J080343.91+100306.2 ($z = 0.034116$, 10228 km s^{-1}); also notice small blue galaxy $\sim$2.5 arcmin W, SDSS J080332.99+100259.1 ($z = 0.034658$).
56612 – three large, disky companions: SDSS J090320.38+134142.0, $\sim$3 arcmin E ($z = 0.029988$), SDSS J090313.10+134444.1, $\sim$3 arcmin NE ($z = 0.028401$) and SDSS J090254.93+133938.4, $\sim$4 arcmin SW ($z = 0.029838$); the small galaxy $\sim$40 arcsec W is in the background ($z = 0.102$).
56650 – perhaps hint of galaxy signal (not well centered on SDSS redshift).

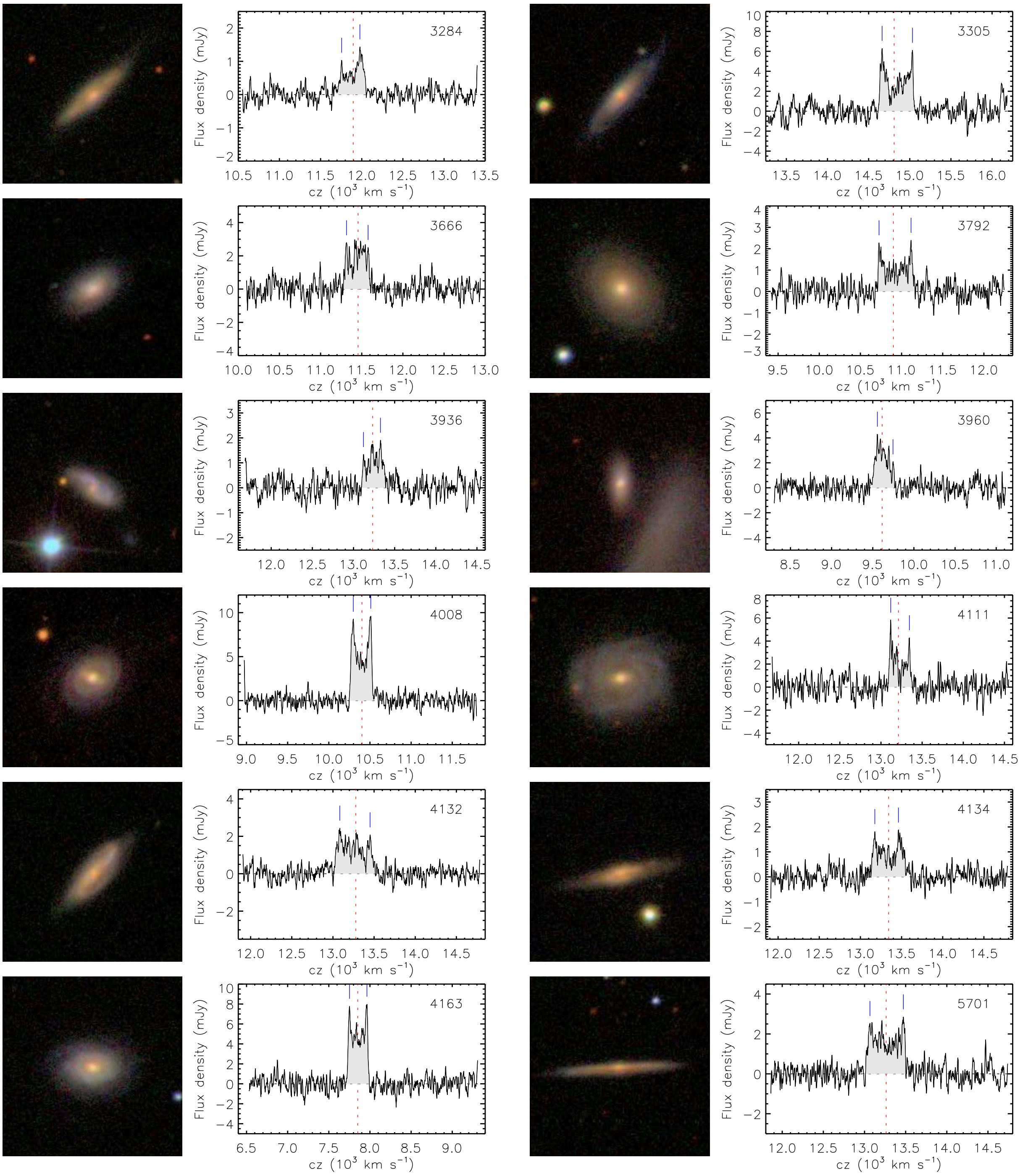

Figure 14. SDSS postage stamp images (1 arcmin square) and HI-line profiles of the detections included in this final data release, ordered by increasing GASS number (indicated in each spectrum). The HI spectra are calibrated, smoothed and baseline-subtracted. A dotted line and two dashes indicate the heliocentric velocity corresponding to the SDSS redshift and the two peaks used for width measurement, respectively. This is a sample of the complete figure, which is available in the online version of the article.

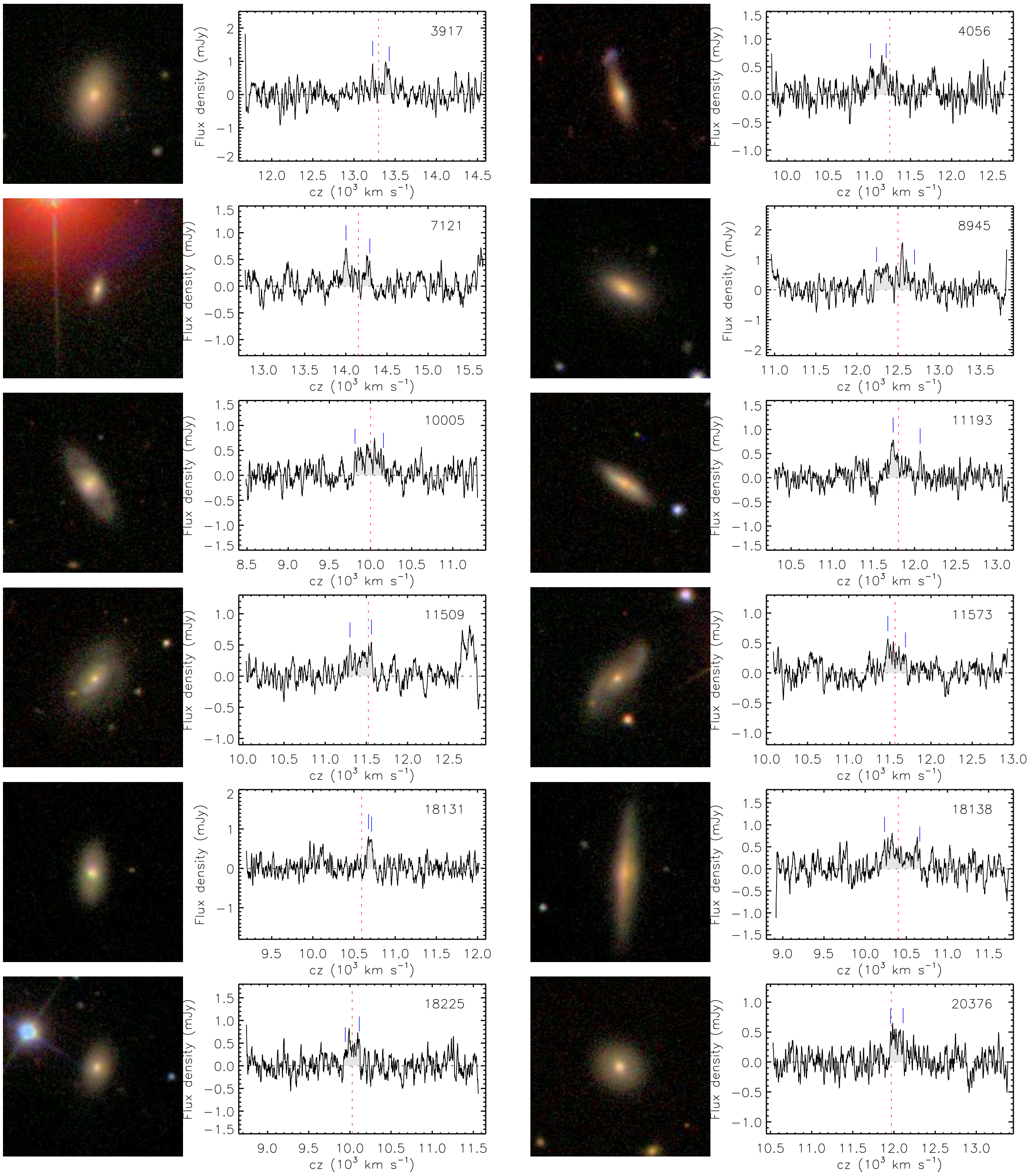

Figure 15. Same as Figure 14 for marginal and/or confused detections. Here galaxies are sorted by quality flag first (starting with code 2 and increasing) and, within each category, by GASS number. This is a sample of the complete figure, which is available in the online version of the article.

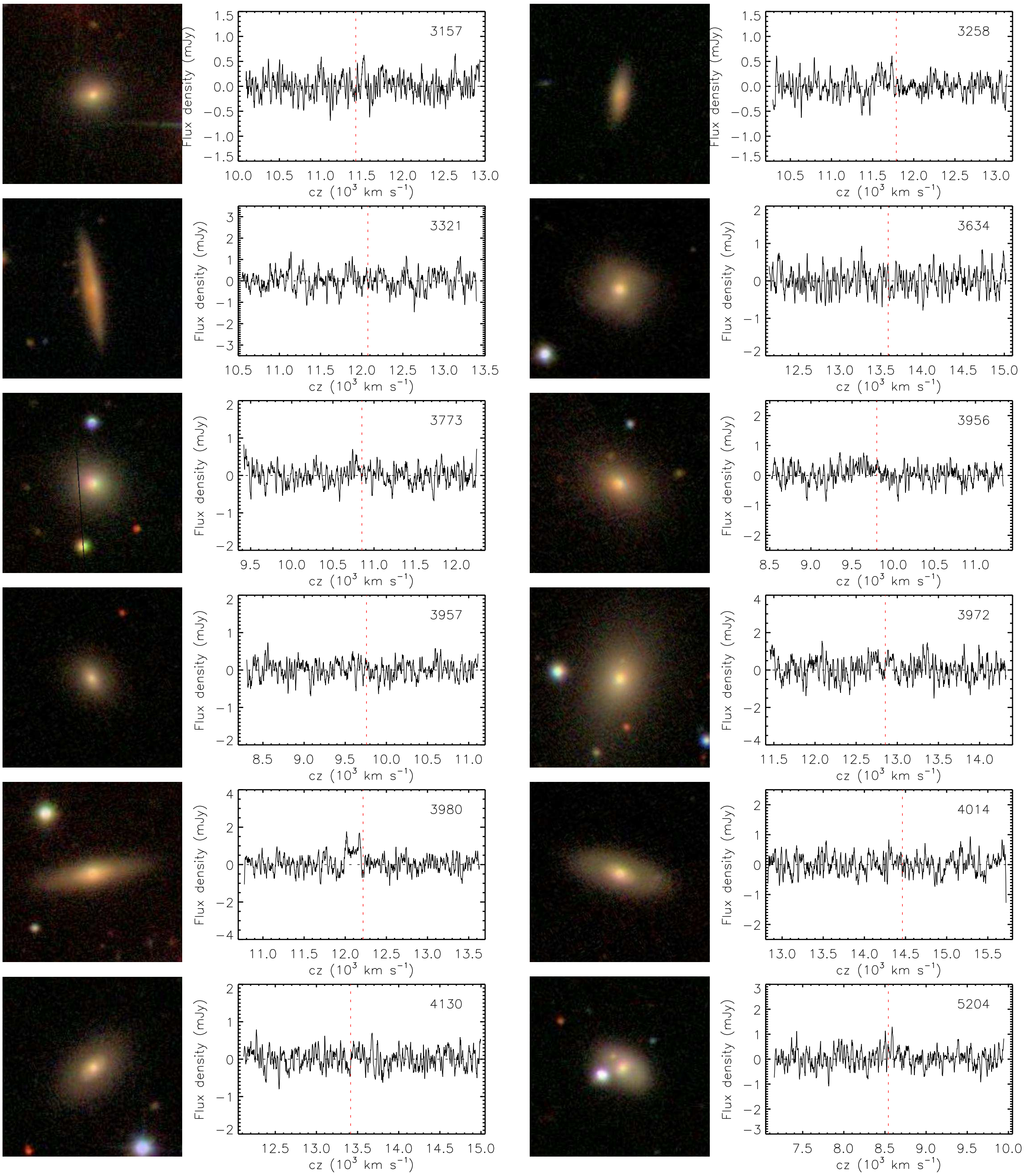

Figure 16. Same as Figure 14 for non-detections. This is a sample of the complete figure, which is available in the online version of the article.

Table 2. SDSS and UV Parameters.

GASS (1)	SDSS ID (2)	Other name (3)	$z_{\rm SDSS}$ (4)	Log $M_\star$ (M$_\odot$) (5)	$R_{50,z}$ ($''$) (6)	R_{50} ($''$) (7)	R_{90} ($''$) (8)	Log $\mu_\star$ (M$_\odot$ kpc^{-2}) (9)	ext$_r$ (mag) (10)	r (mag) (11)	(b/a)$_r$ (12)	incl (deg) (13)	NUV$-r$ (mag) (14)	T$_{NUV}$ (sec) (15)	$T_{\rm max}$ (min) (16)
11892	J000200.82+150132.1	...	0.0357	10.54	3.12	3.37	9.96	8.99	0.13	15.03	0.820	36	5.60	1705	49
11903	J000458.72+154018.2	...	0.0373	10.17	2.16	2.11	5.99	8.90	0.19	15.93	0.411	69	5.49	260	71
11910	J000632.57+154004.7	...	0.0370	10.28	2.97	3.10	8.53	8.74	0.18	15.67	0.555	58	3.69	260	68
12030	J001842.68+151142.6	...	0.0372	10.65	2.41	2.44	7.63	9.29	0.13	14.85	0.724	45	5.68	1588	34
12062	J002556.06+153815.0	...	0.0365	10.09	2.63	2.83	6.16	8.67	0.15	15.41	0.708	46	2.36	222	65
3157	J003032.94+145635.4	...	0.0381	10.57	2.73	2.87	8.41	9.08	0.17	15.33	0.744	43	5.09	3133	56
3258	J005316.95+160556.1	...	0.0393	10.27	2.82	3.11	7.98	8.72	0.21	16.23	0.363	72	6.23	1918	88
3305	J005709.66+143906.6	...	0.0494	10.71	3.22	3.83	11.49	8.84	0.14	15.39	0.360	72	3.02	1996	85
3321	J010228.41+154457.0	...	0.0403	10.85	5.22	5.52	13.71	8.75	0.31	15.42	0.218	85	5.76	110	19
3284	J010253.84+141140.3	...	0.0397	10.60	4.16	4.82	12.14	8.71	0.14	15.57	0.335	74	5.05	110	57
3634	J011347.63+153029.8	...	0.0453	10.89	3.58	3.72	10.82	9.01	0.18	14.87	0.908	25	6.15	1440	26
3666	J011803.07+153224.4	...	0.0382	10.25	3.30	3.49	9.00	8.59	0.16	15.47	0.614	54	2.96	1647	78
3773	J012153.31+145344.6	...	0.0362	10.56	2.68	2.79	8.81	9.13	0.13	14.82	0.887	28	5.31	1658	47
3792	J012842.03+143633.2	...	0.0364	10.81	4.44	5.34	15.14	8.93	0.10	14.62	0.805	37	4.79	112	15
27250	J013006.16+131702.1	...	0.0380	10.24	4.22	4.67	10.19	8.37	0.15	15.25	0.928	22	2.59	198	76
27284	J013204.58+153001.2	...	0.0440	10.95	4.31	4.89	13.12	8.93	0.15	14.47	0.772	40	3.61	107	18
3851	J013851.94+150258.8	CGCG437-007	0.0278	10.59	4.14	4.49	13.67	9.02	0.16	14.45	1.000	2	5.88	2954	14
4111	J014601.79+141421.0	...	0.0441	10.89	6.64	8.49	16.61	8.49	0.14	14.63	0.733	44	3.39	1625	24
4165	J015046.48+134127.5	...	0.0441	10.83	2.42	2.65	8.85	9.31	0.21	15.10	0.708	46	5.83	1661	30
4163	J015244.40+131133.3	...	0.0262	10.22	3.89	4.47	10.87	8.75	0.19	14.85	0.699	47	2.94	1661	17
4134	J015606.45+123403.2	...	0.0445	10.64	3.23	3.60	10.14	8.86	0.19	15.77	0.335	74	5.16	1659	76
4136	J015703.78+131001.4	...	0.0323	10.85	4.42	4.85	14.49	9.09	0.15	14.43	0.558	58	5.70	1651	8
4130	J015720.03+131013.4	...	0.0448	10.81	3.37	3.54	11.49	8.99	0.15	15.03	0.621	53	5.09	1651	36
4132	J015742.52+132318.8	...	0.0443	10.82	4.15	4.52	10.15	8.83	0.16	15.25	0.330	74	3.79	1651	32
3917	J015755.84+132129.3	...	0.0444	10.95	3.95	4.07	10.82	9.00	0.15	14.61	0.664	50	4.48	1651	18
3936	J015945.90+134652.6	...	0.0441	10.12	3.82	3.83	7.14	8.20	0.17	15.94	0.426	67	2.72	1663	141
3957	J020325.71+133910.7	...	0.0325	10.14	2.70	3.01	9.15	8.80	0.24	15.75	0.683	48	5.57	1664	40
3960	J020351.38+144534.3	...	0.0321	10.03	2.21	2.68	6.87	8.87	0.17	15.68	0.449	66	3.30	1664	38
3956	J020353.23+134011.9	...	0.0327	10.59	3.29	3.63	11.75	9.07	0.26	14.92	0.778	40	5.64	1662	27
3966	J020455.76+140055.4	...	0.0310	10.53	4.07	4.50	14.63	8.87	0.21	14.85	0.779	40	5.69	1664	29
3972	J020539.16+143907.7	...	0.0429	11.15	4.49	4.67	14.67	9.12	0.13	14.19	0.709	46	5.83	564	6
4014	J020720.31+130154.4	...	0.0482	10.98	3.54	3.60	11.85	9.05	0.26	14.67	0.509	61	5.57	1661	22
4008	J020829.86+124359.9	...	0.0347	10.49	3.70	4.28	10.55	8.81	0.31	14.96	0.783	39	3.28	1661	53
3987	J021337.66+132741.5	...	0.0420	10.80	2.47	2.62	8.43	9.31	0.28	14.78	0.718	45	5.93	1692	28
4056	J021349.29+135035.7	...	0.0375	10.42	1.75	1.81	5.29	9.33	0.35	15.41	0.434	67	4.17	1692	72
3980	J021423.65+122015.6	...	0.0408	10.95	2.82	2.97	8.91	9.37	0.42	14.44	0.463	65	...	201	13
12069	J073906.01+290936.2	CGCG147-050	0.0388	11.13	6.76	7.73	17.60	8.83	0.13	13.70	0.924	23	2.93	1531	5
14260	J074158.62+231035.0	CGCG117-066	0.0431	11.06	2.47	2.56	8.67	9.54	0.14	14.17	0.733	44	5.71	194	10
14017	J074426.50+291609.7	CGCG147-063	0.0396	10.92	2.97	3.09	10.11	9.32	0.09	14.47	0.568	57	5.41	1535	13
21842	J074533.96+184812.0	...	0.0450	11.06	4.36	5.72	17.49	9.01	0.10	14.57	0.729	44	5.41	156	12
51334	J075329.53+140122.8	...	0.0294	10.10	3.59	4.28	9.68	8.61	0.10	16.04	0.202	88	3.57	1656	27
51351	J075457.85+142718.8	CGCG058-069	0.0293	11.01	5.21	6.28	18.89	9.19	0.09	13.60	0.615	54	3.95	209	3

Table 2. – *continued*

GASS (1)	SDSS ID (2)	Other name (3)	$z_{\rm SDSS}$ (4)	Log $M_\star$ ($M_\odot$) (5)	$R_{50,z}$ ($''$) (6)	R_{50} ($''$) (7)	R_{90} ($''$) (8)	Log $\mu_\star$ ($M_\odot$ kpc^{-2}) (9)	ext$_r$ (mag) (10)	r (mag) (11)	(b/a)$_r$ (12)	incl (deg) (13)	NUV$-r$ (mag) (14)	T_{NUV} (sec) (15)	$T_{\rm max}$ (min) (16)
51462	J075600.62+141144.6	CGCG058-072	0.0357	11.10	2.97	3.04	9.69	9.59	0.09	13.63	0.483	63	6.11	196	4
51336	J075617.10+143609.6	...	0.0474	11.00	5.38	6.18	13.64	8.72	0.09	14.66	0.732	44	4.20	209	19
19132	J080020.05+222634.8	...	0.0350	10.35	2.04	2.10	6.46	9.18	0.18	15.50	0.832	35	5.74	1696	54
56320	J080342.27+100159.7	...	0.0337	10.22	2.69	2.87	8.25	8.85	0.07	15.64	0.776	40	6.37	218	47
51580	J080403.84+150518.4	...	0.0390	10.24	2.24	2.49	7.46	8.90	0.10	16.52	0.264	80	4.27	2650	85
14247	J080528.11+355648.1	IC2225	0.0330	11.14	6.73	7.72	22.90	8.99	0.13	13.53	0.567	57	4.90	218	2
19274	J081625.36+255928.8	UGC4303	0.0453	11.32	6.38	8.06	20.00	8.94	0.10	14.01	0.753	42	4.54	78	4
51899	J083131.52+192228.3	...	0.0387	10.01	2.72	3.01	6.85	8.51	0.09	16.26	0.510	61	3.27	3072	82
52045	J083836.42+173809.2	CGCG089-060	0.0415	10.17	3.45	3.97	9.44	8.40	0.08	15.47	0.962	16	2.25	1830	109
32308	J083934.43+252837.6	...	0.0292	10.02	7.09	8.07	14.75	7.93	0.10	15.33	0.943	20	3.52	4026	26
56486	J084528.61+143425.6	...	0.0360	10.26	2.79	2.82	7.35	8.79	0.05	15.46	0.787	39	4.98	1685	61
56509	J085045.27+114839.0	...	0.0297	10.48	2.10	2.18	6.52	9.44	0.09	14.79	0.491	63	5.60	5569	28
8096	J085254.99+030908.4	...	0.0345	10.28	3.64	3.89	9.42	8.62	0.14	15.33	0.614	54	2.81	112	51
19989	J085425.62+081241.0	...	0.0294	10.46	2.97	3.14	10.01	9.13	0.14	14.78	0.658	50	5.73	1545	27
52297	J085724.03+204237.9	...	0.0328	10.49	3.18	3.44	10.42	9.00	0.07	15.03	0.572	57	4.19	1637	42
56662	J090254.93+133938.5	...	0.0299	10.24	5.22	6.66	15.78	8.41	0.09	15.90	0.227	84	4.71	1612	29
56612	J090307.74+134149.4	...	0.0290	10.27	2.15	2.36	6.97	9.23	0.08	15.29	0.477	64	5.07	1612	25
56650	J090308.20+133103.9	...	0.0289	10.24	1.78	1.85	5.43	9.37	0.09	15.50	0.463	65	5.81	1612	25
20026	J090610.15+082343.3	...	0.0457	10.46	2.10	2.22	7.41	9.04	0.14	15.66	0.912	25	5.40	1696	163
20041	J091427.70+080445.9	...	0.0309	10.03	2.97	3.19	9.10	8.65	0.13	15.78	0.350	73	4.77	2441	32
20042	J091444.06+083605.3	...	0.0468	10.01	2.69	2.61	6.02	8.35	0.14	16.30	0.617	53	2.64	2187	180
16756	J091717.67+064151.5	...	0.0333	10.43	2.79	3.07	9.89	9.04	0.10	15.22	0.654	51	5.85	1693	44
16815	J091831.34+065223.3	...	0.0393	10.63	1.62	1.82	6.02	9.56	0.11	15.60	0.605	54	5.96	1693	49
19672	J091929.51+341810.2	...	0.0458	10.73	3.11	3.33	7.19	8.96	0.05	15.00	0.690	48	2.55	168	58
33019	J092533.76+272050.9	CGCG151-078	0.0484	11.15	4.73	4.92	13.76	8.97	0.06	14.34	0.298	77	5.72	345	10
32937	J092708.07+292408.2	CGCG151-081	0.0258	10.45	5.57	6.63	18.38	8.68	0.06	14.60	0.441	66	4.02	8435	16
32907	J093009.18+285351.3	...	0.0349	10.47	4.36	4.64	10.94	8.65	0.06	15.79	0.261	80	4.58	112	54
53269	J093116.00+263259.6	...	0.0458	10.98	2.52	2.64	7.93	9.39	0.06	15.10	0.375	71	6.98	202	18
20165	J093231.96+094957.3	...	0.0498	10.82	2.23	2.25	6.96	9.26	0.11	15.34	0.823	35	...	...	53
33214	J093624.28+320445.5	...	0.0269	10.34	5.02	5.45	16.21	8.63	0.05	14.78	0.842	33	5.23	213	19
20149	J093647.77+100551.1	...	0.0494	10.91	4.15	4.51	10.97	8.82	0.08	15.03	0.351	73	4.20	106	35
55745	J093710.07+165837.9	NGC2928	0.0278	10.92	10.04	12.44	28.70	8.57	0.10	13.71	0.432	67	4.28	106	3
8349	J093953.62+034850.2	...	0.0285	10.36	3.46	4.18	12.26	8.92	0.14	15.61	0.328	75	4.73	1735	24
33469	J095009.35+333409.5	NGC3013	0.0270	10.61	4.82	5.56	15.62	8.93	0.04	14.24	0.718	45	...	...	11
22822	J095144.91+353719.6	...	0.0270	10.56	3.73	4.22	10.92	9.10	0.03	14.81	0.393	70	3.79	208	14
20376	J095416.82+103457.5	...	0.0399	10.54	2.83	3.11	8.57	8.97	0.08	15.44	0.776	40	5.40	208	78
20445	J095429.64+103530.1	...	0.0397	10.71	2.13	2.19	6.67	9.40	0.08	14.84	0.434	67	5.93	208	34
26017	J095641.82+111144.6	...	0.0416	10.71	5.24	5.46	11.51	8.57	0.09	14.97	0.562	58	4.46	109	42
33737	J095851.33+320423.0	CGCG153-007	0.0270	10.69	5.85	7.27	17.66	8.84	0.04	14.28	0.661	50	...	...	8
33777	J100250.75+323840.2	...	0.0477	10.10	1.70	1.77	4.49	8.82	0.04	16.86	0.718	45	5.47	109	195
8634	J101324.41+050131.7	...	0.0464	10.13	1.32	1.37	3.54	9.09	0.08	16.74	0.862	31	5.59	320	174
26407	J102138.86+131845.6	...	0.0461	11.03	5.41	5.96	12.97	8.77	0.13	14.34	0.576	57	3.71	111	15

Table 2. – *continued*

GASS (1)	SDSS ID (2)	Other name (3)	$z_{\rm SDSS}$ (4)	Log $M_\star$ ($M_\odot$) (5)	$R_{50,z}$ ($''$) (6)	R_{50} ($''$) (7)	R_{90} ($''$) (8)	Log $\mu_\star$ ($M_\odot$ kpc^{-2}) (9)	ext$_r$ (mag) (10)	r (mag) (11)	(b/a)$_r$ (12)	incl (deg) (13)	NUV$-r$ (mag) (14)	T$_{NUV}$ (sec) (15)	$T_{\rm max}$ (min) (16)
26406	J102149.72+132649.6	CGCG065-008	0.0322	10.76	4.83	5.98	15.67	8.92	0.12	14.23	0.714	46	4.47	111	12
54240	J102253.59+243623.0	IC2569	0.0463	11.13	4.61	4.98	15.67	9.01	0.06	14.32	0.867	31	5.97	199	9
26503	J102314.32+125224.0	...	0.0329	10.45	1.92	2.00	6.46	9.39	0.11	15.15	0.528	60	5.36	322	42
26436	J102413.51+131444.8	...	0.0326	10.01	2.36	2.36	6.00	8.78	0.11	16.09	0.883	29	5.57	322	41
23029	J102705.85+110317.5	IC612	0.0323	10.90	3.65	3.76	11.45	9.30	0.08	14.12	0.524	60	5.72	335	6
26535	J102727.40+132526.2	...	0.0315	10.06	3.68	3.82	9.73	8.47	0.12	15.41	0.431	67	3.26	331	35
5204	J102750.83+023634.0	...	0.0285	10.40	3.00	3.14	7.85	9.09	0.10	14.82	0.785	39	4.70	3027	23
23070	J102802.88+104630.4	...	0.0448	11.02	4.77	5.25	13.43	8.89	0.09	15.37	0.200	90	4.33	335	14
23102	J102949.21+115144.4	...	0.0386	10.18	4.20	4.38	9.99	8.30	0.09	16.04	0.459	65	4.64	332	81
54577	J103018.65+273422.9	...	0.0480	11.00	2.83	2.95	9.83	9.27	0.07	14.73	0.675	49	5.71	1661	20
55541	J103246.99+211256.3	...	0.0429	10.62	4.41	5.04	12.50	8.61	0.07	15.31	0.233	83	3.08	190	72
23203	J103549.90+121212.7	CGCG065-061	0.0371	10.92	4.34	4.55	13.98	9.05	0.08	14.26	0.732	44	6.03	211	10
26586	J103611.29+131025.3	...	0.0334	10.06	1.47	1.55	4.23	9.22	0.08	15.87	0.651	51	4.16	106	45
23213	J103621.90+115317.0	...	0.0293	10.14	3.49	3.74	9.00	8.67	0.07	15.53	0.331	74	3.67	206	26
26569	J103808.15+131737.0	...	0.0319	10.25	3.52	3.71	9.89	8.70	0.10	15.36	0.568	57	4.38	106	37
23302	J104248.63+110000.8	...	0.0295	10.43	3.56	3.83	11.02	8.94	0.08	14.79	0.708	46	4.51	439	27
15257	J104805.79+060114.4	...	0.0288	10.09	2.46	2.43	6.68	8.94	0.08	15.75	0.731	44	5.45	209	24
8971	J104837.87+044756.4	...	0.0333	10.15	4.44	4.60	9.93	8.35	0.08	15.75	0.600	55	4.42	42538	45
34723	J105134.08+301221.8	...	0.0356	10.57	3.55	3.86	12.37	8.91	0.07	15.03	0.726	45	5.60	2610	43
8953	J105241.71+040913.9	...	0.0425	10.95	3.76	4.09	11.57	9.08	0.12	14.81	0.525	60	5.56	217	15
8945	J105315.29+042003.1	...	0.0417	10.82	2.39	2.69	7.90	9.37	0.11	15.27	0.461	65	4.60	1515	25
23496	J105721.59+120611.0	...	0.0477	10.16	4.62	4.99	9.72	8.01	0.05	15.55	0.564	57	2.08	203	196
17635	J105935.53+085536.5	CGCG066-078	0.0309	10.48	4.75	5.08	11.56	8.69	0.08	14.72	0.442	66	3.61	106	33
17673	J105958.54+102312.4	...	0.0363	10.32	3.32	3.31	8.26	8.71	0.09	15.46	0.815	36	5.63	107	63
15485	J110004.55+080622.2	...	0.0349	10.13	2.08	2.07	4.81	8.95	0.10	15.82	0.790	39	5.48	442	54
23457	J110011.41+121015.1	...	0.0354	10.12	3.90	4.55	10.31	8.39	0.05	16.59	0.213	86	4.49	106	57
17622	J110043.97+090243.0	...	0.0354	10.05	3.50	4.04	11.28	8.41	0.07	16.58	0.260	80	4.49	106	57
34989	J110339.49+315129.4	UGC6124	0.0466	11.04	3.51	4.03	13.19	9.15	0.08	14.87	0.361	72	4.35	6247	15
48356	J111113.19+284147.0	NGC3561	0.0287	11.25	6.43	8.53	24.67	9.26	0.08	13.40	0.819	36	4.33	959	1
47825	J111147.22+281602.2	CGCG156-017	0.0359	11.05	3.54	3.74	12.53	9.39	0.06	14.04	0.823	35	5.66	959	5
48205	J111151.56+271156.0	...	0.0471	11.12	3.56	4.14	14.72	9.21	0.06	14.31	0.775	40	3.44	184	10
48160	J111201.78+275053.8	...	0.0474	11.03	3.40	3.89	11.51	9.15	0.06	14.94	0.665	50	5.46	199	16
17824	J111404.85+090924.0	...	0.0342	10.11	3.05	3.37	7.82	8.62	0.09	16.02	0.302	77	3.77	1605	49
23531	J111429.02+110847.8	...	0.0406	10.74	2.20	2.30	7.02	9.38	0.04	14.88	0.212	86	5.78	1612	34
5701	J111509.40+024156.4	...	0.0442	10.72	4.23	5.43	13.81	8.72	0.19	15.75	0.111	90	4.03	220	51
48521	J111738.91+263506.0	...	0.0475	10.29	1.22	1.25	3.99	9.30	0.05	15.90	0.836	34	3.06	183	192
48518	J111750.72+263927.0	...	0.0285	10.42	5.03	5.15	13.21	8.65	0.04	14.78	0.734	44	4.33	183	23
24496	J111809.91+074653.9	...	0.0421	10.60	3.13	3.61	9.04	8.90	0.11	15.45	0.437	67	3.41	1524	73
12452	J112006.21+041035.6	...	0.0492	10.82	3.28	3.54	10.16	8.94	0.12	15.42	0.407	69	5.53	1536	51
48544	J112039.09+271737.4	...	0.0486	11.05	4.05	4.59	14.73	9.00	0.06	14.49	0.665	50	5.11	186	17
5848	J112142.43+033424.5	CGCG039-145	0.0391	10.44	4.83	5.58	13.83	8.43	0.13	15.30	0.313	76	2.96	2045	85
23703	J112731.58+120834.3	IC2835	0.0459	10.74	2.88	3.21	8.98	9.04	0.10	15.25	0.572	57	5.48	127	55

Table 2. – *continued*

GASS (1)	SDSS ID (2)	Other name (3)	$z_{\rm SDSS}$ (4)	Log $M_\star$ ($M_\odot$) (5)	$R_{50,z}$ ($''$) (6)	R_{50} ($''$) (7)	R_{90} ($''$) (8)	Log $\mu_\star$ ($M_\odot$ kpc^{-2}) (9)	ext$_r$ (mag) (10)	r (mag) (11)	(b/a)$_r$ (12)	incl (deg) (13)	NUV$-r$ (mag) (14)	T$_{NUV}$ (sec) (15)	$T_{\rm max}$ (min) (16)
48604	J112746.27+265734.5	CGCG156-077	0.0334	10.60	3.76	4.34	10.11	8.95	0.05	14.64	0.657	50	3.20	51	29
6015	J113524.48+021627.3	...	0.0289	10.23	2.33	2.92	7.75	9.13	0.08	16.40	0.371	71	4.46	1714	25
23761	J113704.29+125535.7	IC2945	0.0345	11.07	5.96	6.71	21.97	8.99	0.08	13.80	0.727	44	5.06	341	4
23739	J113706.07+115237.7	...	0.0358	10.90	2.72	2.93	9.64	9.47	0.08	14.58	0.432	67	6.13	252	9
23789	J114144.66+122937.1	...	0.0342	10.41	3.23	3.37	9.03	8.87	0.11	15.11	0.913	25	5.69	112	50
23781	J114212.30+113041.1	...	0.0432	10.62	2.36	2.51	7.87	9.14	0.10	15.49	0.610	54	4.29	258	75
48994	J114218.00+301349.0	UGC6664	0.0322	10.73	6.70	9.16	25.94	8.61	0.06	14.35	0.275	79	2.67	103	14
23815	J115036.65+112151.9	...	0.0306	10.23	2.66	3.03	9.31	8.95	0.11	15.47	0.613	54	3.24	107	32
18084	J115112.59+085311.6	...	0.0351	10.34	5.30	5.61	10.74	8.35	0.06	15.27	0.706	46	3.85	112	55
18004	J115135.06+084507.6	...	0.0352	11.12	5.39	5.42	17.74	9.11	0.07	13.89	0.809	37	5.75	112	3
49433	J115536.63+292104.4	...	0.0458	10.45	3.12	3.27	8.43	8.68	0.06	15.57	0.627	53	3.67	109	164
49386	J115913.81+305325.8	...	0.0294	10.53	3.13	3.81	12.26	9.15	0.04	15.19	0.416	68	5.30	1680	23
18138	J120239.51+085624.2	...	0.0347	10.64	4.46	4.98	14.66	8.81	0.06	15.40	0.247	81	5.13	86	27
18185	J120308.04+110920.4	...	0.0438	10.83	3.72	3.83	12.91	8.95	0.07	14.81	0.828	35	5.68	1201	30
49727	J120445.20+311132.9	CGCG158-011	0.0250	10.27	2.31	2.40	7.85	9.30	0.05	15.11	0.455	65	4.76	1695	14
18131	J120445.85+092521.1	...	0.0353	10.34	2.29	2.61	7.65	9.07	0.07	15.49	0.568	57	7.05	86	57
18225	J120511.42+103341.0	...	0.0334	10.14	2.49	2.55	7.06	8.84	0.06	15.94	0.745	43	4.68	1201	45
18220	J120536.25+104113.3	...	0.0344	10.50	3.72	3.70	10.17	8.83	0.07	15.17	0.320	75	4.71	1201	50
28062	J122800.84+081108.1	...	0.0377	10.70	4.06	4.52	12.83	8.87	0.06	14.91	0.514	61	4.43	3272	30
28030	J122902.67+083133.3	...	0.0385	10.02	4.16	4.43	8.60	8.15	0.06	16.27	0.522	60	3.75	1597	81
50404	J123409.10+280750.5	...	0.0400	10.55	2.24	2.30	6.65	9.18	0.04	15.05	0.635	52	5.26	1626	76
12967	J123553.51+054723.4	...	0.0419	10.57	3.64	4.06	14.50	8.74	0.06	15.06	0.630	52	5.05	3047	82
50406	J123653.92+274456.8	NGC4559B	0.0258	10.41	6.09	6.12	13.65	8.57	0.06	14.34	0.817	36	3.11	1626	16
50550	J124128.01+284728.3	...	0.0350	10.29	3.66	3.73	8.26	8.62	0.05	15.14	0.622	53	3.27	123	55
50856	J125547.82+281521.9	...	0.0270	10.40	4.23	5.16	14.97	8.83	0.03	15.40	0.241	82	5.13	2547	19
50866	J125609.90+275039.3	...	0.0253	10.49	4.93	5.39	15.59	8.85	0.03	14.51	0.527	60	5.69	2780	14
40495	J125626.93+093604.5	...	0.0459	10.92	3.09	3.20	9.48	9.15	0.06	14.71	0.645	51	5.08	247	24
35497	J125650.61+285547.4	...	0.0270	10.44	4.66	4.96	14.57	8.79	0.03	14.25	0.384	70	4.92	2593	19
40502	J125752.83+101754.6	...	0.0363	10.19	3.44	3.89	9.89	8.54	0.06	15.87	0.219	85	3.15	233	63
35475	J125935.67+283304.9	...	0.0253	10.29	2.59	2.71	9.10	9.21	0.03	14.94	0.576	57	5.79	3503	14
35437	J130125.07+284038.0	...	0.0291	10.23	7.60	7.89	15.76	8.09	0.04	14.45	0.923	23	2.70	3503	26
6679	J130210.77+030623.6	CGCG043-105	0.0472	11.03	3.57	3.78	11.84	9.11	0.09	14.07	0.937	21	3.32	306	16
13159	J130525.44+035929.7	...	0.0437	10.37	2.40	2.66	6.96	8.86	0.07	16.62	0.290	78	5.27	3371	135
40647	J130624.82+095635.8	...	0.0487	10.73	4.16	4.32	9.22	8.65	0.07	14.88	0.653	51	3.09	354	74
25215	J131032.19+110121.0	CGCG072-010	0.0427	10.59	4.29	4.54	10.41	8.60	0.08	14.84	0.635	52	2.98	293	81
25213	J131222.82+114339.5	...	0.0320	10.12	4.09	4.38	9.21	8.43	0.08	15.60	0.628	53	3.42	128	38
26936	J131525.21+152522.2	CGCG101-014	0.0266	10.74	3.48	3.80	12.19	9.36	0.07	14.36	0.458	65	5.99	332	6
44354	J132050.70+313700.6	...	0.0448	10.68	4.17	6.36	15.28	8.67	0.03	15.33	0.660	50	3.06	3417	66
51150	J132259.87+270659.1	IC4234	0.0345	10.80	6.54	6.91	16.82	8.64	0.06	13.74	0.815	36	3.60	161224	13
51161	J132522.77+271456.7	...	0.0345	10.15	5.07	5.65	14.19	8.21	0.04	15.38	0.616	54	2.84	161224	51
43963	J134142.40+300731.5	NGC5271	0.0370	11.05	5.46	7.83	22.14	8.98	0.04	13.98	0.640	52	4.03	148	5
35659	J134159.72+294653.5	...	0.0449	11.14	4.73	5.35	16.17	9.02	0.05	14.41	0.515	61	4.83	148	8

Table 2. – *continued*

GASS (1)	SDSS ID (2)	Other name (3)	z_{SDSS} (4)	Log $M_\star$ ($M_\odot$) (5)	$R_{50,z}$ ($''$) (6)	R_{50} ($''$) (7)	R_{90} ($''$) (8)	Log $\mu_\star$ ($M_\odot$ kpc^{-2}) (9)	ext$_r$ (mag) (10)	r (mag) (11)	(b/a)$_r$ (12)	incl (deg) (13)	NUV$-r$ (mag) (14)	T$_{NUV}$ (sec) (15)	T_{max} (min) (16)
44021	J134231.07+301500.1	CGCG161-128	0.0363	11.06	4.03	4.23	14.07	9.27	0.04	14.18	0.460	65	5.23	148	5
38018	J134834.19+245329.2	...	0.0297	10.08	4.18	5.09	13.46	8.44	0.04	16.24	0.230	83	3.35	178	28
35981	J135308.35+354250.5	UGC8802	0.0411	10.30	4.78	8.79	19.46	8.25	0.04	15.31	0.458	65	2.50	3864	106
44856	J135411.14+243322.5	...	0.0286	10.05	1.60	1.64	4.92	9.28	0.04	15.85	0.669	49	5.29	268	24
44892	J135609.30+251143.6	CGCG132-055	0.0290	10.66	4.42	4.78	15.64	9.00	0.05	14.40	0.769	41	5.59	268	12
13618	J135622.01+043710.6	...	0.0339	10.20	2.96	3.22	8.06	8.74	0.08	16.01	0.339	74	4.62	18451	47
13674	J135815.23+035953.8	CGCG046-020	0.0300	10.10	5.25	5.64	11.64	8.25	0.10	15.00	0.522	61	2.58	18849	29
9317	J140430.25+050629.4	...	0.0295	10.04	4.71	5.05	10.95	8.30	0.07	15.13	0.912	25	2.64	15250	27
38458	J140603.77+123016.2	...	0.0387	10.41	2.82	3.17	10.94	8.88	0.08	15.50	0.887	28	5.51	220	82
7121	J140642.63+015452.2	...	0.0472	10.24	1.34	1.45	4.05	9.18	0.10	16.48	0.415	68	4.46	129	187
30746	J140908.49+061048.8	...	0.0363	10.32	1.92	2.00	5.84	9.18	0.06	15.55	0.508	62	5.91	1680	63
7310	J141657.47+021039.5	CGCG018-102	0.0261	10.44	2.48	2.66	9.00	9.37	0.12	14.67	0.614	54	5.20	1636	16
45254	J141830.77+291012.3	CGCG163-026	0.0349	11.03	3.46	3.88	12.27	9.41	0.05	14.02	0.677	49	4.98	161	5
7405	J141837.70+020245.4	...	0.0256	10.53	4.55	5.01	10.96	8.95	0.10	14.98	0.269	79	3.74	1636	13
45940	J142748.88+262900.7	...	0.0325	10.43	2.55	2.89	9.90	9.13	0.05	15.16	0.822	36	5.86	61	40
28703	J142802.34+120134.9	...	0.0267	10.16	5.84	5.87	14.22	8.32	0.07	15.41	0.250	81	3.77	108	18
9615	J143001.87+032352.1	...	0.0333	10.15	1.62	1.69	4.97	9.23	0.08	16.67	0.808	37	5.35	1691	44
9607	J143043.65+031149.3	...	0.0268	10.26	2.16	2.19	6.65	9.28	0.08	15.06	0.396	70	5.79	1691	18
38198	J143134.60+244053.6	...	0.0378	10.65	4.01	4.49	13.32	8.83	0.09	14.81	0.471	64	...	...	37
31095	J143749.60+064454.3	CGCG047-122	0.0290	10.08	6.14	6.39	13.46	8.13	0.09	14.91	0.600	55	2.52	1995	25
41621	J144011.86+081512.2	...	0.0296	10.35	1.69	1.71	5.16	9.50	0.08	15.03	0.399	69	5.27	93	28
9702	J144043.35+032226.4	IC1043	0.0319	10.79	2.25	2.32	7.37	9.63	0.09	14.41	0.510	61	5.50	2701	10
9938	J144140.50+040347.1	...	0.0275	10.08	5.75	6.31	12.53	8.24	0.09	15.16	0.936	21	3.12	1696	20
41699	J144213.77+084036.0	CGCG075-117	0.0341	10.92	5.38	6.31	16.05	8.94	0.08	14.24	0.621	53	4.90	218	7
9695	J144216.88+034844.7	...	0.0257	10.13	3.19	3.42	10.96	8.85	0.09	15.18	0.387	70	5.26	1687	15
31131	J144248.49+063924.3	CGCG048-003	0.0279	10.48	3.03	3.26	9.98	9.17	0.09	14.49	0.766	41	5.38	1743	21
9942	J144325.65+042244.6	CGCG048-008	0.0264	10.82	4.34	4.51	15.20	9.25	0.09	13.74	0.787	39	5.22	1911	4
41718	J144338.96+083350.7	...	0.0346	10.46	2.62	2.74	8.77	9.09	0.08	15.20	0.822	36	5.73	218	52
31478	J144350.25+313128.7	...	0.0335	10.37	1.77	1.85	5.79	9.37	0.04	15.39	0.412	68	5.49	84	46
41723	J144605.27+085456.2	CGCG076-020	0.0295	10.71	3.28	3.47	11.06	9.29	0.08	14.11	0.618	53	5.29	221	10
29371	J144907.58+105847.6	CGCG076-065	0.0292	10.70	4.18	4.35	14.12	9.07	0.06	14.16	0.677	49	5.31	141	10
10032	J145024.11+043655.2	...	0.0468	10.82	1.66	1.80	5.21	9.57	0.14	15.35	0.407	69	5.43	1682	42
42233	J145304.36+310406.0	...	0.0323	10.49	2.50	3.04	7.68	9.22	0.05	15.48	0.424	68	3.73	317	39
10005	J145307.29+033217.4	...	0.0334	10.47	2.51	2.64	7.48	9.17	0.11	15.05	0.734	44	4.95	5768	45
42191	J145403.73+305046.4	...	0.0320	10.12	1.71	1.74	4.86	9.19	0.06	15.31	0.641	52	2.62	317	38
38935	J145458.46+114156.2	CGCG076-094	0.0305	10.90	3.61	4.02	14.43	9.36	0.09	13.88	0.576	57	5.09	79	5
41743	J150204.10+064922.9	...	0.0462	10.45	3.39	3.57	8.99	8.60	0.09	15.79	0.415	68	3.59	1677	171
39014	J150513.62+084747.6	CGCG076-145	0.0449	11.05	4.86	5.23	15.92	8.91	0.09	14.21	0.767	41	5.00	79	12
39082	J150721.51+095541.0	CGCG077-013	0.0352	11.02	5.41	5.68	18.80	9.01	0.10	13.99	0.586	56	5.14	148	5
41869	J150921.50+070439.8	...	0.0414	10.15	3.22	3.16	6.85	8.44	0.11	16.05	0.366	72	3.40	1613	109
41863	J151028.90+072455.4	...	0.0322	10.11	4.20	3.43	8.99	8.40	0.10	16.46	0.356	72	1.76	1613	39
10211	J151219.92+031826.6	...	0.0469	10.97	5.70	5.81	13.20	8.65	0.12	14.88	0.386	70	4.01	1666	21

Table 2. – *continued*

GASS (1)	SDSS ID (2)	Other name (3)	$z_{\rm SDSS}$ (4)	Log $M_\star$ ($M_\odot$) (5)	$R_{50,z}$ ($''$) (6)	R_{50} ($''$) (7)	R_{90} ($''$) (8)	Log $\mu_\star$ ($M_\odot$ kpc^{-2}) (9)	ext$_r$ (mag) (10)	r (mag) (11)	(b/a)$_r$ (12)	incl (deg) (13)	NUV$-r$ (mag) (14)	T$_{NUV}$ (sec) (15)	$T_{\rm max}$ (min) (16)
7813	J151243.59+012752.2	CGCG021-049	0.0293	10.79	4.15	4.74	15.08	9.17	0.13	14.04	0.581	56	5.60	1811	7
25057	J152106.26+304036.9	...	0.0308	10.01	3.12	2.90	8.04	8.59	0.06	15.81	0.719	45	5.35	2185	32
25115	J152112.78+303928.5	CGCG165-039	0.0308	10.50	2.93	2.79	8.96	9.14	0.06	14.60	0.537	59	5.40	2185	32
39407	J152239.21+083226.7	...	0.0366	10.26	2.57	2.64	7.44	8.86	0.10	15.89	0.484	63	5.26	1513	65
39532	J152346.52+083853.1	...	0.0301	10.24	4.03	4.09	11.06	8.62	0.09	15.55	0.731	44	6.09	1513	29
28348	J154051.59+282027.7	...	0.0329	10.22	3.32	3.96	10.44	8.69	0.08	16.22	0.415	68	4.62	4531	42
28327	J154129.97+275911.4	...	0.0320	11.02	3.40	3.93	13.28	9.49	0.10	13.79	0.865	31	5.84	4531	3
28317	J154408.13+274024.3	...	0.0316	10.07	1.99	2.03	5.71	9.02	0.09	15.76	0.457	65	5.75	943	36
25682	J154811.74+090424.5	...	0.0393	10.59	2.55	2.75	8.97	9.13	0.11	15.11	0.639	52	5.85	1703	57
25721	J155506.74+093023.0	...	0.0341	10.09	2.62	2.99	8.40	8.73	0.11	16.38	0.346	73	4.16	1688	49
10918	J221421.77+135711.1	CGCG428-054	0.0261	10.78	4.78	5.18	15.28	9.14	0.17	13.89	0.860	31	4.85	7104	4
11086	J225524.42+131453.8	NGC7414	0.0329	10.43	2.68	2.77	7.96	9.08	0.14	15.21	0.390	70	4.26	1690	42
11080	J225608.33+130337.9	...	0.0290	10.10	2.26	2.47	6.76	9.01	0.12	15.91	0.366	72	4.74	2905	25
11249	J230757.92+152455.2	...	0.0362	10.11	2.93	2.78	6.69	8.60	0.64	15.96	0.791	39	7.87	298	63
11257	J230806.95+152520.1	...	0.0368	10.18	2.47	2.65	6.79	8.80	0.69	16.34	0.331	74	4.10	298	67
11312	J231225.98+135450.1	...	0.0339	10.44	2.40	2.54	7.54	9.17	0.19	15.16	0.526	60	5.60	3264	48
11193	J231321.76+141648.8	...	0.0394	10.50	2.46	2.75	6.76	9.07	0.19	15.57	0.296	77	5.41	4965	88
11192	J231340.27+140127.7	...	0.0399	10.56	1.16	1.00	1.83	9.77	0.18	17.19	0.804	37	3.67	3264	70
11284	J231545.95+133035.6	...	0.0394	10.34	3.03	3.25	7.93	8.72	0.17	16.23	0.234	83	5.13	3335	88
11292	J231608.02+134918.4	...	0.0389	10.54	2.89	3.02	8.12	8.98	0.17	15.31	0.488	63	4.56	3335	69
11291	J231616.05+135042.9	...	0.0386	10.39	2.38	2.69	8.05	9.00	0.17	15.62	0.372	71	3.01	3335	82
11347	J231647.75+153459.7	...	0.0388	10.87	3.11	3.12	9.36	9.25	0.13	14.56	0.541	59	5.81	4851	15
11444	J232114.19+131851.2	...	0.0420	10.69	6.15	7.56	17.62	8.40	0.25	15.18	0.514	61	3.63	1682	48
11410	J232222.95+135938.2	...	0.0415	10.55	2.53	2.66	8.53	9.05	0.13	15.23	0.787	39	5.72	1676	86
11435	J232321.31+141704.4	...	0.0434	10.97	4.80	5.30	14.70	8.87	0.11	14.71	0.387	70	4.66	1676	15
11434	J232326.70+140753.9	...	0.0417	10.96	5.25	5.84	14.81	8.81	0.13	14.24	0.728	44	3.49	1676	14
11636	J232331.69+151401.6	...	0.0394	10.10	2.87	3.04	7.71	8.54	0.20	16.08	0.886	28	4.30	3180	89
11395	J232337.45+133908.1	...	0.0425	10.77	2.34	2.47	8.15	9.32	0.19	15.30	0.921	23	5.40	1676	34
11509	J232407.17+145006.6	...	0.0384	10.50	4.06	4.49	11.62	8.65	0.15	15.15	0.519	61	4.36	1681	80
11524	J232423.53+152636.3	...	0.0256	10.41	3.20	3.44	10.30	9.14	0.14	14.65	0.419	68	5.52	3180	15
11585	J232516.78+142135.6	...	0.0445	11.08	3.09	3.36	11.34	9.34	0.11	14.51	0.686	48	6.09	1681	10
11544	J232538.54+152115.9	IC1488	0.0412	11.22	5.48	5.86	17.42	9.06	0.19	14.48	0.213	86	5.95	208	4
11676	J232711.15+144546.3	...	0.0418	10.58	3.51	4.07	11.27	8.79	0.15	15.95	0.371	71	4.37	1681	77
11669	J232713.50+152831.1	...	0.0466	10.74	5.17	5.80	12.32	8.51	0.17	15.01	0.835	34	3.20	208	60
11685	J232749.71+150709.1	...	0.0419	11.16	7.54	8.74	20.31	8.71	0.20	14.02	0.586	56	4.39	208	5
11571	J232934.08+132718.3	...	0.0337	10.28	5.13	5.48	11.94	8.36	0.15	15.04	0.668	49	2.80	109	46
11573	J233011.60+132656.3	...	0.0386	10.47	3.75	4.95	11.81	8.69	0.17	15.49	0.494	63	3.69	109	81
11568	J233013.51+132801.7	...	0.0417	11.19	3.58	3.91	12.59	9.39	0.17	14.11	0.628	53	5.56	109	5
11567	J233019.67+132657.4	...	0.0399	11.22	4.40	4.69	15.29	9.27	0.17	13.87	0.722	45	5.69	109	3
11791	J235159.08+144504.1	...	0.0466	10.95	3.74	4.26	13.09	9.00	0.09	14.96	0.918	24	4.67	1699	23

Table 3. HI Properties of GASS Detections.

GASS (1)	SDSS ID (2)	z_{SDSS} (3)	T_{on} (min) (4)	Δv (km s^{-1}) (5)	z (6)	W_{50} (km s^{-1}) (7)	$W_{50}{}^{c}$ (km s^{-1}) (8)	F (Jy km s^{-1}) (9)	rms (mJy) (10)	S/N (11)	Log M_{HI} (M$_{\odot}$) (12)	Log $M_{HI}/M_{\star}$ (13)	Q (14)
11910	J000632.57+154004.7	0.0370	14	13	0.037052	317± 1	300	0.45± 0.06	0.41	12.1	9.43	−0.85	1
12062	J002556.06+153815.0	0.0365	5	13	0.036445	255± 12	240	1.18± 0.09	0.64	22.9	9.84	−0.25	1*
3305	J005709.66+143906.6	0.0494	5	13	0.049501	403± 6	378	1.30± 0.13	0.75	16.9	10.15	−0.56	1
3284	J010253.84+141140.3	0.0397	53	16	0.039637	289± 7	271	0.23± 0.03	0.20	12.3	9.20	−1.40	1
3666	J011803.07+153224.4	0.0382	10	13	0.038173	295± 8	278	0.60± 0.07	0.49	14.1	9.59	−0.66	1*
3792	J012842.03+143633.2	0.0364	15	13	0.036442	416± 2	396	0.49± 0.07	0.39	11.9	9.45	−1.36	1
27250	J013006.16+131702.1	0.0380	10	13	0.037986	76± 6	67	0.58± 0.04	0.53	24.9	9.57	−0.67	1
27284	J013204.58+153001.2	0.0440	10	13	0.043984	358± 12	336	0.74± 0.08	0.47	16.2	9.80	−1.15	1
3851	J013851.94+150258.8	0.0278	15	15	0.028420	380± 11	362	0.40± 0.07	0.37	9.9	9.15	−1.44	5*
4111	J014601.79+141421.0	0.0441	4	13	0.044131	251± 4	235	0.61± 0.10	0.75	10.0	9.72	−1.17	1*
4165	J015046.48+134127.5	0.0441	29	16	0.044554	307± 1	287	0.25± 0.04	0.26	9.8	9.34	−1.49	5*
4163	J015244.40+131133.3	0.0262	5	13	0.026201	241± 1	229	1.29± 0.09	0.69	24.0	9.59	−0.63	1
4134	J015606.45+123403.2	0.0445	30	13	0.044484	376± 19	354	0.41± 0.05	0.29	14.5	9.55	−1.09	1
4136	J015703.78+131001.4	0.0323	16	15	0.032649	185± 38	172	0.20± 0.04	0.31	8.5	8.97	−1.88	5*
4132	J015742.52+132318.8	0.0443	15	16	0.044231	429± 18	404	0.65± 0.06	0.33	16.5	9.75	−1.07	1
3917	J015755.84+132129.3	0.0444	20	21	0.044457	227± 3	207	0.09± 0.04	0.25	3.7	8.90	−2.05	2*
3936	J015945.90+134652.6	0.0441	18	16	0.044144	248± 12	230	0.30± 0.05	0.35	9.6	9.41	−0.71	1*
3960	J020351.38+144534.3	0.0321	8	13	0.032172	231± 7	218	0.61± 0.07	0.53	15.1	9.45	−0.58	1*
3966	J020455.76+140055.4	0.0310	34	13	0.031305	271± 7	257	0.18± 0.04	0.26	8.1	8.88	−1.65	5*
4008	J020829.86+124359.9	0.0347	5	13	0.034677	255± 3	240	1.55± 0.08	0.61	31.5	9.91	−0.58	1
3987	J021337.66+132741.5	0.0420	28	13	0.041602	303± 3	285	0.26± 0.04	0.30	9.9	9.30	−1.50	5*
4056	J021349.29+135035.7	0.0375	72	16	0.037049	217± 17	202	0.08± 0.02	0.17	5.3	8.66	−1.76	2*
12069	J073906.01+290936.2	0.0388	5	13	0.038927	212± 5	198	1.50± 0.09	0.74	27.6	10.00	−1.13	1
21842	J074533.96+184812.0	0.0450	12	16	0.045075	450± 7	423	0.55± 0.09	0.44	9.9	9.70	−1.36	1
51334	J075329.53+140122.8	0.0294	4	13	0.029414	320± 8	304	0.98± 0.11	0.76	14.4	9.57	−0.53	1*
51351	J075457.85+142718.8	0.0293	8	15	0.029280	523± 2	501	1.31± 0.12	0.58	15.8	9.69	−1.32	1
51336	J075617.10+143609.6	0.0474	19	21	0.047309	467± 2	436	0.25± 0.07	0.29	5.5	9.39	−1.61	2
51580	J080403.84+150518.4	0.0390	20	16	0.038927	331± 2	311	0.21± 0.05	0.31	6.7	9.15	−1.09	1*
14247	J080528.11+355648.1	0.0330	8	13	0.033040	480± 6	458	0.93± 0.13	0.71	10.8	9.65	−1.49	1*
51899	J083131.52+192228.3	0.0387	10	13	0.039004	439± 4	416	1.08± 0.09	0.49	19.7	9.86	−0.15	5*
52045	J083836.42+173809.2	0.0415	4	13	0.041499	120± 2	109	0.81± 0.08	0.83	17.5	9.79	−0.38	1*
32308	J083934.43+252837.6	0.0292	8	13	0.029284	89± 4	81	0.26± 0.05	0.66	8.2	8.99	−1.03	1*
56509	J085045.27+114839.0	0.0297	15	13	0.029791	411± 5	393	1.00± 0.08	0.50	19.5	9.59	−0.89	1*
8096	J085254.99+030908.4	0.0345	5	15	0.034417	320± 29	301	0.92± 0.13	0.79	11.7	9.68	−0.60	1*
19989	J085425.62+081241.0	0.0294	30	15	0.029674	135± 9	124	0.12± 0.03	0.29	6.4	8.66	−1.80	1*
52297	J085724.03+204237.9	0.0328	8	13	0.032899	374± 8	356	0.63± 0.10	0.63	10.4	9.48	−1.01	1*
56662	J090254.93+133938.5	0.0299	20	15	0.029924	329± 26	312	0.28± 0.05	0.31	9.1	9.04	−1.20	1*
20041	J091427.70+080445.9	0.0309	35	15	0.030998	400± 6	381	0.33± 0.05	0.24	12.1	9.14	−0.89	5*
20042	J091444.06+083605.3	0.0468	60	16	0.046879	165± 6	150	0.11± 0.02	0.19	8.2	9.04	−0.97	1
16815	J091831.34+065223.3	0.0393	20	13	0.039284	368± 10	348	0.42± 0.05	0.34	12.9	9.45	−1.18	1
19672	J091929.51+341810.2	0.0458	5	13	0.045872	461± 3	434	1.34± 0.16	0.86	13.3	10.10	−0.63	1*
32937	J092708.07+292408.2	0.0258	5	13	0.025831	286± 6	272	0.82± 0.11	0.81	12.0	9.38	−1.07	1
32907	J093009.18+285351.3	0.0349	20	15	0.034934	355± 13	336	0.42± 0.07	0.42	9.6	9.35	−1.12	1
33214	J093624.28+320445.5	0.0269	20	15	0.027319	256± 22	241	0.16± 0.05	0.36	5.2	8.72	−1.62	2*
55745	J093710.07+165837.9	0.0278	8	21	0.027813	298± 6	280	0.25± 0.08	0.45	5.1	8.94	−1.98	2*
8349	J093953.62+034850.2	0.0285	29	15	0.028783	341± 4	324	0.18± 0.05	0.27	6.6	8.82	−1.55	1
22822	J095144.91+353719.6	0.0270	5	13	0.027185	346± 6	331	2.70± 0.16	0.99	29.2	9.94	−0.62	1
20376	J095416.82+103457.5	0.0399	73	16	0.040141	164± 1	150	0.06± 0.02	0.16	5.4	8.65	−1.89	2*
33737	J095851.33+320423.0	0.0270	4	10	0.026078	232± 3	222	2.97± 0.10	0.87	50.6	9.95	−0.74	1*
8634	J101324.41+050131.7	0.0464	45	13	0.046469	387± 3	363	0.30± 0.04	0.24	12.6	9.46	−0.67	1*
26407	J102138.86+131845.6	0.0461	15	13	0.046205	405± 3	381	0.40± 0.07	0.38	10.1	9.58	−1.45	1*
26406	J102149.72+132649.6	0.0322	4	15	0.032289	361± 8	342	0.79± 0.15	0.83	9.0	9.56	−1.20	1*
26535	J102727.40+132526.2	0.0315	15	15	0.031589	197± 13	184	0.37± 0.05	0.40	12.0	9.22	−0.84	1
23070	J102802.88+104630.4	0.0448	15	21	0.044654	297± 19	274	0.18± 0.06	0.34	4.8	9.21	−1.81	2*
55541	J103246.99+211256.3	0.0429	10	13	0.042826	414± 12	391	0.89± 0.11	0.62	13.8	9.86	−0.76	1*
26586	J103611.29+131025.3	0.0334	15	13	0.033420	235± 9	221	0.38± 0.05	0.41	11.9	9.27	−0.79	1*
23213	J103621.90+115317.0	0.0293	20	13	0.029327	330± 9	314	0.38± 0.05	0.35	11.8	9.15	−0.99	1
26569	J103808.15+131737.0	0.0319	25	15	0.032112	298± 3	281	0.25± 0.04	0.28	9.3	9.05	−1.20	1
15257	J104805.79+060114.4	0.0288	24	15	0.028847	237± 5	223	0.19± 0.04	0.26	8.6	8.84	−1.25	5*
8945	J105315.29+042003.1	0.0417	25	21	0.041555	492± 2	462	0.25± 0.06	0.26	6.1	9.28	−1.55	2*
23496	J105721.59+120611.0	0.0477	4	13	0.047793	295± 12	276	0.99± 0.11	0.72	15.7	10.00	−0.16	1*
17635	J105935.53+085536.5	0.0309	29	13	0.030908	407± 3	389	0.31± 0.05	0.30	10.1	9.11	−1.37	1
17673	J105958.54+102312.4	0.0363	65	15	0.036722	292± 0	274	0.10± 0.03	0.17	5.9	8.77	−1.55	3*
17622	J110043.97+090243.0	0.0354	18	15	0.035435	323± 9	305	0.33± 0.06	0.37	9.0	9.26	−0.79	1*
34989	J110339.49+315129.4	0.0466	10	13	0.046642	570± 2	539	2.01± 0.10	0.50	27.6	10.29	−0.75	1
48356	J111113.19+284147.0	0.0287	4	15	0.029177	361± 65	343	0.70± 0.12	0.67	10.1	9.42	−1.83	5*
17824	J111404.85+090924.0	0.0342	29	13	0.034214	332± 4	315	0.28± 0.05	0.31	10.1	9.17	−0.94	1
5701	J111509.40+024156.4	0.0442	20	13	0.044244	459± 8	434	0.80± 0.07	0.40	17.0	9.84	−0.88	1*
48521	J111738.91+263506.0	0.0475	19	13	0.047483	185± 2	171	0.25± 0.04	0.34	10.5	9.39	−0.90	1*
48518	J111750.72+263927.0	0.0285	25	15	0.027409	657± 39	632	0.91± 0.07	0.29	17.1	9.48	−0.94	5*
24496	J111809.91+074653.9	0.0421	10	21	0.042109	395± 14	369	0.76± 0.08	0.38	15.6	9.77	−0.83	1*
5848	J112142.43+033424.5	0.0391	10	13	0.039110	374± 1	354	0.89± 0.10	0.62	14.6	9.78	−0.66	1
23703	J112731.58+120834.3	0.0459	35	13	0.046082	461± 7	434	0.42± 0.05	0.27	12.9	9.59	−1.15	1*
48604	J112746.27+265734.5	0.0334	5	13	0.033400	377± 4	359	1.22± 0.11	0.70	17.8	9.78	−0.82	1*
6015	J113524.48+021627.3	0.0289	20	13	0.028967	267± 1	253	0.41± 0.07	0.53	9.4	9.18	−1.05	1*
23739	J113706.07+115237.7	0.0358	12	15	0.035465	321± 1	302	0.32± 0.06	0.38	8.5	9.25	−1.65	1*
23789	J114144.66+122937.1	0.0342	55	15	0.034194	420± 5	399	0.16± 0.04	0.20	6.9	8.92	−1.49	5*
23781	J114212.30+113041.1	0.0432	15	16	0.042980	438± 8	413	0.58± 0.07	0.36	13.2	9.67	−0.95	5*
48994	J114218.00+301349.0	0.0322	5	10	0.032286	392± 4	375	4.41± 0.17	1.15	43.2	10.31	−0.42	1*
23815	J115036.65+112151.9	0.0306	20	13	0.030651	323± 1	307	0.49± 0.05	0.36	14.9	9.30	−0.93	1*
18084	J115112.59+085311.6	0.0351	60	15	0.035164	282± 9	265	0.12± 0.03	0.18	7.3	8.82	−1.52	1*
49433	J115536.63+292104.4	0.0458	49	21	0.045765	290± 15	267	0.20± 0.03	0.16	11.0	9.27	−1.18	1
49386	J115913.81+305325.8	0.0294	27	15	0.029527	281± 9	266	0.29± 0.04	0.27	11.6	9.04	−1.49	1*
18138	J120239.51+085624.2	0.0347	30	21	0.034827	454± 4	429	0.16± 0.05	0.21	5.2	8.94	−1.70	2*
49727	J120445.20+311132.9	0.0250	10	15	0.025875	610± 36	587	1.56± 0.11	0.47	19.7	9.66	−0.61	5*
18131	J120445.85+092521.1	0.0353	55	15	0.035668	68± 2	58	0.05± 0.01	0.18	6.0	8.44	−1.90	2*
18225	J120511.42+103341.0	0.0334	54	15	0.033446	191± 8	178	0.08± 0.03	0.19	5.3	8.59	−1.55	2*
28062	J122800.84+081108.1	0.0377	30	16	0.037733	336± 17	316	0.29± 0.05	0.27	10.5	9.26	−1.44	5*
50404	J123409.10+280750.5	0.0400	45	13	0.039994	139± 7	128	0.14± 0.02	0.24	9.6	8.99	−1.56	1*
50406	J123653.92+274456.8	0.0258	15	13	0.025781	232± 12	220	0.37± 0.05	0.42	11.6	9.04	−1.37	1*
50550	J124128.01+284728.3	0.0350	9	15	0.035114	302± 2	285	0.48± 0.08	0.47	10.6	9.42	−0.87	1
40495	J125626.93+093604.5	0.0459	24	21	0.046039	297± 33	274	0.14± 0.05	0.26	4.7	9.11	−1.81	2*
40502	J125752.83+101754.6	0.0363	10	13	0.036272	344± 5	325	0.90± 0.10	0.64	15.0	9.72	−0.47	1*
35437	J130125.07+284038.0	0.0291	10	13	0.029200	136± 6	126	0.42± 0.05	0.52	13.7	9.19	−1.04	1
6679	J130210.77+030623.6	0.0472	20	13	0.047236	275± 10	256	0.47± 0.05	0.38	14.6	9.67	−1.36	1*
13159	J130525.44+035929.7	0.0437	80	16	0.043717	286± 12	266	0.28± 0.03	0.20	15.1	9.38	−0.99	1*
40647	J130624.82+095635.8	0.0487	60	13	0.048734	363± 8	340	0.26± 0.03	0.20	13.4	9.44	−1.29	1
25215	J131032.19+110121.0	0.0427	5	13	0.042796	395± 4	372	0.59± 0.12	0.69	8.5	9.68	−0.91	1*
44354	J132050.70+313700.6	0.0448	5	13	0.044821	298± 6	279	1.76± 0.10	0.67	30.0	10.19	−0.49	1
51150	J132259.87+270659.1	0.0345	10	15	0.034400	259± 20	243	0.42± 0.07	0.44	10.7	9.34	−1.46	1*
51161	J132522.77+271456.7	0.0345	5	15	0.034577	260± 6	244	0.61± 0.11	0.76	8.9	9.50	−0.65	1*

Table 3. – *continued*

GASS (1)	SDSS ID (2)	$z_{\rm SDSS}$ (3)	$T_{\rm on}$ (min) (4)	Δv (km s^{-1}) (5)	z (6)	W_{50} (km s^{-1}) (7)	$W_{50}{}^c$ (km s^{-1}) (8)	F (Jy km s^{-1}) (9)	rms (mJy) (10)	S/N (11)	Log $M_{\rm HI}$ (M$_\odot$) (12)	Log $M_{\rm HI}/M_\star$ (13)	Q (14)
43963	J134142.40+300731.5	0.0370	5	13	0.037112	309± 9	292	1.14± 0.11	0.71	18.1	9.84	−1.21	1
38018	J134834.19+245329.2	0.0297	4	13	0.029694	344± 3	328	0.72± 0.11	0.73	10.7	9.45	−0.63	1
35981	J135308.35+354250.5	0.0411	5	5	0.041152	376± 3	359	3.45± 0.14	1.33	42.2	10.41	0.11	1
44856	J135411.14+243322.5	0.0286	25	15	0.028646	301± 18	285	0.49± 0.05	0.29	17.8	9.25	−0.80	1*
13618	J135622.01+043710.6	0.0339	49	15	0.033857	226± 12	211	0.10± 0.03	0.21	6.0	8.72	−1.48	3*
13674	J135815.23+035953.8	0.0300	4	21	0.030004	289± 11	270	0.78± 0.12	0.67	10.6	9.49	−0.61	1*
9317	J140430.25+050629.4	0.0295	5	13	0.029490	170± 9	159	0.65± 0.07	0.66	15.0	9.39	−0.65	1
38458	J140603.77+123016.2	0.0387	80	21	0.038176	693± 15	658	0.29± 0.03	0.12	10.6	9.27	−1.14	5*
7121	J140642.63+015452.2	0.0472	85	21	0.047163	323± 4	298	0.08± 0.03	0.17	4.2	8.91	−1.33	2*
45254	J141830.77+291012.3	0.0349	9	15	0.034914	401± 20	380	0.85± 0.09	0.46	16.4	9.66	−1.37	1
7405	J141837.70+020245.4	0.0256	10	12	0.025494	381± 12	366	1.34± 0.09	0.58	23.6	9.58	−0.95	1*
28703	J142802.34+120134.9	0.0267	15	13	0.026712	290± 7	277	0.37± 0.06	0.41	10.5	9.06	−1.10	1*
9615	J143001.87+032352.1	0.0333	20	13	0.033333	274± 2	259	0.52± 0.06	0.41	15.1	9.41	−0.74	1*
38198	J143134.60+244053.6	0.0378	10	13	0.037903	444± 3	421	0.79± 0.08	0.47	14.8	9.70	−0.95	1*
31095	J143749.60+064454.3	0.0290	4	13	0.028963	258± 5	245	1.10± 0.11	0.85	16.0	9.61	−0.47	1*
9938	J144140.50+040347.1	0.0275	20	13	0.027482	123± 0	114	0.16± 0.04	0.41	6.9	8.71	−1.37	1
41699	J144213.77+084036.0	0.0341	12	15	0.034344	65± 1	56	0.08± 0.03	0.35	5.1	8.62	−2.30	2
9942	J144325.65+042244.6	0.0264	9	21	0.026518	544± 2	520	0.29± 0.10	0.40	4.2	8.95	−1.87	3*
41718	J144338.96+083350.7	0.0346	50	15	0.035164	112± 5	101	0.12± 0.02	0.20	9.9	8.81	−1.65	1*
10032	J145024.11+043655.2	0.0468	51	16	0.046652	369± 14	345	0.26± 0.04	0.20	12.2	9.40	−1.42	1*
42233	J145304.36+310406.0	0.0323	15	13	0.032279	360± 9	343	0.57± 0.07	0.41	14.7	9.42	−1.07	1*
10005	J145307.29+033217.4	0.0334	50	21	0.033306	362± 2	340	0.12± 0.04	0.17	5.9	8.78	−1.69	2*
42191	J145403.73+305046.4	0.0320	40	15	0.031869	206± 44	192	0.15± 0.04	0.25	7.4	8.82	−1.30	1*
41743	J150204.10+064922.9	0.0462	20	13	0.046269	345± 3	324	0.42± 0.06	0.37	12.1	9.60	−0.85	1
39082	J150721.51+095541.0	0.0352	9	15	0.035525	273± 7	256	0.29± 0.08	0.50	6.4	9.21	−1.81	2*
41869	J150921.50+070439.8	0.0414	29	13	0.041479	314± 2	296	0.25± 0.04	0.29	9.9	9.29	−0.86	1*
41863	J151028.90+072455.4	0.0322	5	13	0.032382	365± 7	347	1.40± 0.10	0.65	22.3	9.81	−0.30	5*
7813	J151243.59+012752.2	0.0293	12	13	0.029083	245± 12	232	0.51± 0.08	0.58	11.1	9.27	−1.52	1*
28317	J154408.13+274024.3	0.0316	20	13	0.031915	218± 2	205	0.28± 0.05	0.38	9.9	9.09	−0.98	1*
25721	J155506.74+093023.0	0.0341	44	21	0.034207	341± 3	319	0.15± 0.04	0.20	6.1	8.88	−1.21	2*
11086	J225524.42+131453.8	0.0329	15	13	0.032889	354± 2	336	0.44± 0.07	0.45	10.2	9.32	−1.11	1*
11312	J231225.98+135450.1	0.0339	16	13	0.034147	487± 4	465	0.74± 0.07	0.39	15.4	9.58	−0.86	5*
11193	J231321.76+141648.8	0.0394	85	16	0.039671	376± 3	354	0.10± 0.03	0.17	5.2	8.82	−1.68	2*
11192	J231340.27+140127.7	0.0399	9	13	0.039981	339± 16	320	1.01± 0.07	0.47	22.9	9.85	−0.71	5
11292	J231608.02+134918.4	0.0389	64	16	0.038807	458± 2	434	0.31± 0.04	0.18	13.4	9.32	−1.22	5*
11291	J231616.05+135042.9	0.0386	5	16	0.038580	362± 11	341	0.86± 0.11	0.60	13.6	9.75	−0.64	1*
11347	J231647.75+153459.7	0.0388	10	13	0.038947	474± 6	450	0.95± 0.09	0.47	17.0	9.80	−1.07	5*
11444	J232114.19+131851.2	0.0420	5	10	0.042059	173± 2	161	1.17± 0.07	0.68	28.9	9.96	−0.73	1
11435	J232321.31+141704.4	0.0434	16	16	0.043500	521± 1	491	0.32± 0.07	0.33	6.7	9.42	−1.55	1*
11434	J232326.70+140753.9	0.0417	15	13	0.041839	392± 9	370	0.73± 0.06	0.38	18.8	9.75	−1.21	1*
11509	J232407.17+145006.6	0.0384	80	21	0.038126	283± 28	263	0.08± 0.02	0.14	5.5	8.72	−1.78	2*
11676	J232711.15+144546.3	0.0418	15	13	0.041816	377± 2	356	0.47± 0.07	0.42	11.4	9.56	−1.02	1
11669	J232713.50+152831.1	0.0466	5	13	0.046592	149± 3	137	0.45± 0.07	0.66	11.0	9.64	−1.10	1*
11685	J232749.71+150709.1	0.0419	10	16	0.041926	388± 22	365	0.76± 0.09	0.47	14.8	9.77	−1.39	1
11571	J232934.08+132718.3	0.0337	5	13	0.033577	252± 5	238	1.46± 0.09	0.70	26.2	9.86	−0.43	1
11573	J233011.60+132656.3	0.0386	80	21	0.038617	250± 4	230	0.08± 0.02	0.14	5.2	8.70	−1.77	2*

Table 4. GASS Non-detections.

GASS (1)	SDSS ID (2)	$z_{\rm SDSS}$ (3)	$T_{\rm on}$ (min) (4)	rms (mJy) (5)	Log $M_{{\rm HI},lim}$ (M$_\odot$) (6)	Log $M_{{\rm HI},lim}/M_\star$ (7)	Note (8)
11892	J000200.82+150132.1	0.0357	46	0.21	8.76	−1.78	*
11903	J000458.72+154018.2	0.0373	65	0.18	8.73	−1.44	*
12030	J001842.68+151142.6	0.0372	34	0.26	8.88	−1.77	...
3157	J003032.94+145635.4	0.0381	55	0.20	8.80	−1.77	*
3258	J005316.95+160556.1	0.0393	68	0.17	8.74	−1.53	*
3321	J010228.41+154457.0	0.0403	14	0.42	9.16	−1.69	...
3634	J011347.63+153029.8	0.0453	25	0.29	9.11	−1.78	...
3773	J012153.31+145344.6	0.0362	43	0.23	8.80	−1.76	...
4130	J015720.03+131013.4	0.0448	35	0.25	9.03	−1.78	*
3957	J020325.71+133910.7	0.0325	45	0.21	8.68	−1.46	...
3956	J020353.23+134011.9	0.0327	28	0.27	8.78	−1.81	...
3972	J020539.16+143907.7	0.0429	8	0.51	9.30	−1.85	*
4014	J020720.31+130154.4	0.0482	23	0.29	9.17	−1.81	*
3980	J021423.65+122015.6	0.0408	14	0.37	9.12	−1.83	*
14260	J074158.62+231035.0	0.0431	10	0.51	9.31	−1.75	*
14017	J074426.50+291609.7	0.0396	15	0.42	9.15	−1.77	*
51462	J075600.62+141144.6	0.0357	4	0.73	9.30	−1.80	*
19132	J080020.05+222634.8	0.0350	50	0.24	8.79	−1.56	...
56320	J080342.27+100159.7	0.0337	55	0.20	8.68	−1.53	*
19274	J081625.36+255928.8	0.0453	4	0.69	9.49	−1.83	*
56486	J084528.61+143425.6	0.0360	60	0.17	8.68	−1.57	...
56612	J090307.74+134149.4	0.0290	25	0.29	8.71	−1.56	*
56650	J090308.20+133103.9	0.0289	25	0.29	8.71	−1.53	*
20026	J090610.15+082343.3	0.0457	80	0.21	8.97	−1.49	...
16756	J091717.67+064151.5	0.0333	45	0.22	8.72	−1.71	*
33019	J092533.76+272050.9	0.0484	10	0.45	9.36	−1.79	...
53269	J093116.00+263259.6	0.0458	18	0.32	9.17	−1.81	*
20165	J093231.96+094957.3	0.0498	50	0.21	9.06	−1.76	*
20149	J093647.77+100551.1	0.0494	30	0.27	9.16	−1.75	*
33469	J095009.35+333409.5	0.0270	10	0.50	8.88	−1.73	*
20445	J095429.64+103530.1	0.0397	34	0.26	8.95	−1.76	*
26017	J095641.82+111144.6	0.0416	44	0.23	8.93	−1.78	*
33777	J100250.75+323840.2	0.0477	80	0.17	8.94	−1.16	*
54240	J102253.59+243623.0	0.0463	10	0.45	9.32	−1.81	*
26503	J102314.32+125224.0	0.0329	35	0.26	8.79	−1.66	*
26436	J102413.51+131444.8	0.0326	40	0.23	8.72	−1.28	...
23029	J102705.85+110317.5	0.0323	5	0.61	9.13	−1.77	*
5204	J102750.83+023634.0	0.0285	25	0.33	8.75	−1.65	*
23102	J102949.21+115144.4	0.0386	80	0.15	8.67	−1.51	*
54577	J103018.65+273422.9	0.0480	20	0.31	9.20	−1.80	*
23203	J103549.90+121212.7	0.0371	10	0.43	9.10	−1.82	*
23302	J104248.63+110000.8	0.0295	28	0.26	8.69	−1.74	...
8971	J104837.87+044756.4	0.0333	45	0.23	8.73	−1.42	*
34723	J105134.08+301221.8	0.0356	44	0.22	8.77	−1.80	...
8953	J105241.71+040913.9	0.0425	15	0.38	9.16	−1.79	*
15485	J110004.55+080622.2	0.0349	55	0.19	8.70	−1.43	...
23457	J110011.41+121015.1	0.0354	58	0.18	8.69	−1.43	*
47825	J111147.22+281602.2	0.0359	5	0.69	9.28	−1.77	...
48205	J111151.56+271156.0	0.0471	10	0.44	9.32	−1.80	*
48160	J111201.78+275053.8	0.0474	16	0.35	9.24	−1.79	*
23531	J111429.02+110847.8	0.0406	35	0.25	8.94	−1.80	*
12452	J112006.21+041035.6	0.0492	50	0.22	9.07	−1.75	*
48544	J112039.09+271737.4	0.0486	18	0.34	9.24	−1.81	*
23761	J113704.29+125535.7	0.0345	4	0.78	9.30	−1.77	...
18004	J115135.06+084507.6	0.0352	4	0.64	9.23	−1.89	*
18185	J120308.04+110920.4	0.0438	30	0.27	9.04	−1.79	...
18220	J120536.25+104113.3	0.0344	50	0.22	8.74	−1.76	*
28030	J122902.67+083133.3	0.0385	80	0.16	8.71	−1.31	*
12967	J123553.51+054723.4	0.0419	50	0.20	8.88	−1.69	*
50856	J125547.82+281521.9	0.0270	15	0.37	8.76	−1.64	...
50866	J125609.90+275039.3	0.0253	15	0.37	8.70	−1.79	*

Table 4. – *continued*

GASS (1)	SDSS ID (2)	$z_{\rm SDSS}$ (3)	$T_{\rm on}$ (min) (4)	rms (mJy) (5)	Log $M_{{\rm HI},lim}$ ($M_\odot$) (6)	Log $M_{{\rm HI},lim}/M_\star$ (7)	Note (8)
35497	J125650.61+285547.4	0.0270	20	0.30	8.66	−1.78	*
35475	J125935.67+283304.9	0.0253	15	0.38	8.71	−1.58	*
25213	J131222.82+114339.5	0.0320	40	0.22	8.67	−1.45	*
26936	J131525.21+152522.2	0.0266	5	0.59	8.94	−1.81	...
35659	J134159.72+294653.5	0.0449	8	0.56	9.38	−1.76	...
44021	J134231.07+301500.1	0.0363	5	0.66	9.27	−1.79	*
44892	J135609.30+251143.6	0.0290	12	0.44	8.89	−1.77	...
30746	J140908.49+061048.8	0.0363	60	0.22	8.79	−1.53	*
7310	J141657.47+021039.5	0.0261	15	0.42	8.78	−1.66	*
45940	J142748.88+262900.7	0.0325	40	0.22	8.70	−1.73	*
9607	J143043.65+031149.3	0.0268	23	0.32	8.68	−1.58	...
41621	J144011.86+081512.2	0.0296	30	0.25	8.66	−1.69	...
9702	J144043.35+032226.4	0.0319	10	0.48	9.02	−1.77	*
9695	J144216.88+034844.7	0.0257	16	0.38	8.72	−1.41	...
31131	J144248.49+063924.3	0.0279	20	0.28	8.67	−1.81	...
31478	J144350.25+313128.7	0.0335	45	0.23	8.75	−1.62	*
41723	J144605.27+085456.2	0.0295	10	0.47	8.94	−1.77	*
29371	J144907.58+105847.6	0.0292	10	0.45	8.91	−1.79	...
38935	J145458.46+114156.2	0.0305	9	0.42	8.92	−1.98	...
39014	J150513.62+084747.6	0.0449	12	0.42	9.26	−1.79	...
10211	J151219.92+031826.6	0.0469	20	0.35	9.22	−1.75	*
25057	J152106.26+304036.9	0.0308	33	0.24	8.68	−1.33	*
25115	J152112.78+303928.5	0.0308	30	0.24	8.68	−1.82	*
39407	J152239.21+083226.7	0.0366	60	0.23	8.83	−1.43	*
39532	J152346.52+083853.1	0.0301	30	0.27	8.71	−1.53	...
28348	J154051.59+282027.7	0.0329	38	0.24	8.74	−1.48	*
28327	J154129.97+275911.4	0.0320	4	0.72	9.19	−1.83	*
25682	J154811.74+090424.5	0.0393	57	0.21	8.84	−1.75	*
10918	J221421.77+135711.1	0.0261	4	0.68	8.99	−1.79	...
11080	J225608.33+130337.9	0.0290	25	0.29	8.71	−1.39	*
11249	J230757.92+152455.2	0.0362	63	0.19	8.72	−1.39	*
11257	J230806.95+152520.1	0.0368	63	0.17	8.69	−1.49	*
11284	J231545.95+133035.6	0.0394	84	0.15	8.70	−1.64	*
11410	J232222.95+135938.2	0.0415	80	0.16	8.79	−1.76	*
11636	J232331.69+151401.6	0.0394	84	0.17	8.76	−1.34	*
11395	J232337.45+133908.1	0.0425	35	0.23	8.95	−1.82	*
11524	J232423.53+152636.3	0.0256	15	0.37	8.71	−1.70	...
11585	J232516.78+142135.6	0.0445	10	0.43	9.27	−1.81	*
11544	J232538.54+152115.9	0.0412	4	0.74	9.43	−1.79	*
11568	J233013.51+132801.7	0.0417	5	0.61	9.36	−1.84	*
11567	J233019.67+132657.4	0.0399	4	0.71	9.38	−1.84	*
11791	J235159.08+144504.1	0.0466	19	0.34	9.20	−1.75	*